

# Structural Evaluation of LIC-310-0396 and FAY-35-17-6.82 Box Beams with Advanced Strand Deterioration



Eric Steinberg, Ph.D., P.E.  
Richard Miller, Ph.D., P.E.  
Douglas Nims, Ph.D., P.E.  
Shad Sargand, Ph.D.

for the  
Ohio Department of Transportation  
Office of Research and Development

Federal Highway Administration

State Job Number 134381

September, 2011



Ohio Research Institute for  
Transportation and the Environment  
Civil Engineering

OHIO  
UNIVERSITY



University of Cincinnati  
Department of Civil and  
Environmental Engineering



THE UNIVERSITY OF  
TOLEDO  
1872

University of Toledo  
Department of Civil  
Engineering





# **Structural Evaluation of LIC-310-0396 and FAY-35-17-6.82 Box Beams with Advanced Strand Deterioration**

## **Draft Final Report – Phase II**

Prepared in Cooperation with the  
Ohio Department of Transportation and the  
U.S. Department of Transportation,  
Federal Highway Administration

Principal Investigators:  
Eric Steinberg, Ph.D., P.E.  
and Shad Sargand, Ph.D.  
Ohio University  
Ohio Research Institute for Transportation and the Environment  
Department of Civil Engineering  
Athens, Ohio

Richard Miller, Ph.D., P.E.  
University of Cincinnati  
Department of Civil and Environmental Engineering  
Cincinnati, Ohio

Douglas Nims, Ph.D., P.E.  
University of Toledo  
Department of Civil Engineering  
Toledo, Ohio

The contents of this report reflect the views of the authors, who are responsible for the facts and accuracy of the data presented herein. The contents do not necessarily reflect the official views or policies of the Ohio Department of Transportation or the Federal Highway Administration. This report does not constitute a standard, specification or regulation.

September, 2011

## **ACKNOWLEDGEMENTS**

The authors especially thank Mike Loeffler, ODOT technical liaisons, for his input, scheduling of snooper trucks, coring equipment, and transportation vehicles for hydraulics, finding steel for the frame, and overall encouragement. The assistance provided by Fayette County Engineer, Steve Luebbe, with scheduling of cranes, providing county personnel and equipment to assist on site and to transport steel, and overall general input was greatly appreciated. The assistance of Curtis Zigan from ODOT in locating steel and providing transportation of the steel is also noted. The continual on-site assistance of Fayette County personnel, especially Larry Dean, was deeply appreciated. The work by Issam Khoury of Ohio University related to instrumentation and data acquisition far exceeded expectations. Input, comments, and encouragement from Tim Keller at ODOT are also appreciated by all the authors.

The authors also note the assistance and efforts from graduate students Jon Huffman, Clinton Setty, Kyle Grupenhoff, Brendan Kelly, Drew Hatton, Brad Hoffman, and Santiago Camino from Ohio University, Tyler Stillings from the University of Cincinnati, and Michael Titus from the University of Toledo. Without the hard work and efforts of those involved, the project would not have been completed successfully.

# TABLE OF CONTENTS

<b>DISCLAIMER</b> .....	3
<b>ACKNOWLEDGEMENTS</b> .....	4
<b>TABLE OF CONTENTS</b> .....	5
<b>LIST OF FIGURES</b> .....	7
<b>LIST OF TABLES</b> .....	10
<b>1. INTRODUCTION</b> .....	11
1.1 Purpose .....	11
1.2 Objectives .....	11
1.3 Tasks .....	12
<b>2. BACKGROUND</b> .....	13
2.1 Bridge Details .....	13
2.2 Nondestructive Evaluation .....	15
2.2.1 Visual Inspection .....	15
2.2.2 Ground Penetrating Radar .....	20
2.2.3 Magnetic .....	22
2.2.4 Truck Testing .....	23
2.3 Destructive Testing.....	33
2.3.1 Test Setup .....	33
2.3.2 Testing Procedure .....	36
2.3.2.1 East Span .....	36
2.3.2.2 Center Span .....	39
2.3.2.3 West Span .....	39
2.4 Load Rating .....	41
2.4.1 LFR Rating Method .....	41
2.4.2 LRFR Rating Method .....	44
<b>3. RESULTS</b> .....	48
3.1 Nondestructive Testing .....	48
3.1.1 Ground Penetrating Radar Results.....	48
3.1.2 Magnetic Results .....	50
3.1.3 Truck Testing Results .....	59
3.2 Concrete Coring .....	68
3.3 Chloride Testing .....	69
3.4 Destructive Testing.....	70
3.4.1 East Span .....	70
3.4.2 Center Span .....	77
3.4.3 West Span .....	91
3.4.4 Span Comparison .....	109

<b>4. ANALYSIS</b>	<b>111</b>
4.1 AASHTO Standard Capacities	111
4.2 AASHTO LRFD Capacities	112
4.3 Load Factor Rating (LFR)	113
4.4 Load and Resistance Factor Rating (LRFR)	114
4.5 Distribution Factors	116
4.6 Beam Modeling	117
4.7 Finite Element Modeling	118
<b>5. CONCLUSIONS</b>	<b>127</b>
5.1 Forensic	127
5.2 Full Scale Destructive Testing	127
5.3 Load Rating	128
5.4 Finite Element Modeling	128
<b>6. RECOMMENDATIONS</b>	<b>129</b>
<b>7. REFERENCES</b>	<b>130</b>

## LIST OF FIGURES

Figure 1: FAY 35-17-6.82.....	13
Figure 2: FAY 35-17-6.82 Bridge Span.....	14
Figure 3: FAY 35-17-6.82 Beam Section.....	14
Figure 4: FAY 35-17-6.82 Pier Detail .....	15
Figure 5: Exterior North Beam (Beam 9) - West Span .....	16
Figure 6: Exterior South Beam (Beam 1) – West Span.....	17
Figure 7: Exterior South Beam (Beam 1) – Center Span.....	17
Figure 8: Exterior North Beam (Beam 9) – Center Span.....	18
Figure 9: Exterior South Beam (Beam 1) – East Span .....	18
Figure 10: Exterior North Beam (Beam 9) – East Span.....	19
Figure 11: Exterior North Beam (Beam 9) – East Span.....	19
Figure 12: Interior Beam 3 - East Span .....	20
Figure 13: GPR – Bottom.....	21
Figure 14: GPR – Top.....	21
Figure 15: MFL Sensing Equipment.....	22
Figure 16: University of Toledo IMF Sensor.....	23
Figure 17: Asphalt Removed.....	24
Figure 18: Installed Strain Gage .....	25
Figure 19: Instrumentation Locations .....	25
Figure 20: Cold Patch Placement .....	26
Figure 21: Instrumentation and Supporting Frame.....	26
Figure 22: Data Acquisition System.....	27
Figure 23: Truck Load Case 1 .....	28
Figure 24: Truck Load Case 4.....	29
Figure 25: Truck Loading (Max +M) .....	29
Figure 26: Truck Load Case 5 .....	30
Figure 27: Truck Loading (Max -M) .....	30
Figure 28: Truck Load Case 6.....	32
Figure 29: Truck Load Case 7 .....	32
Figure 30: Truck Load Case 8.....	33
Figure 31: Test Frames on Span 1.....	34
Figure 32: Hydraulic Cylinder .....	34
Figure 33: Abutment Test Frame Anchorage .....	35
Figure 34: Pier Test Frame Anchorage .....	35
Figure 35: Exposed and Cut Strands – East Span.....	36
Figure 36: Damage of East Span .....	37
Figure 37: Steel Tubes with String Potentiometers .....	38
Figure 38: Instrumentation Locations for Center Span.....	38
Figure 39: Damage Created in Beams 4-6 .....	40
Figure 40: Verification Strands Cut.....	40
Figure 41: Truck Configurations .....	42
Figure 42: HL-93 Design Live Load.....	45
Figure 43: GPR of Top Surface .....	49
Figure 44: GPR of Bottom Surface (West Span) .....	50

<b>Figure 45: MFL Test Tracks.....</b>	<b>51</b>
<b>Figure 46: Track Layout / MFL Corrosion Map.....</b>	<b>52</b>
<b>Figure 47: MFL Scan Data Tracks 1I, 3I, 7I and 10I.....</b>	<b>53</b>
<b>Figure 48: MFL Scan Data Tracks 1E, 3E, and 4E .....</b>	<b>55</b>
<b>Figure 49: IMF Field Results for Interior Beam .....</b>	<b>56</b>
<b>Figure 50: Laboratory Results for Tracks 3I and 7I w/ 2.2”between Pole Face/Strand .....</b>	<b>57</b>
<b>Figure 51: Area 2 of Beam 3 Exposed.....</b>	<b>59</b>
<b>Figure 52: Instrument Line A - Truck Tests.....</b>	<b>60</b>
<b>Figure 53: Instrument Line B - Truck Tests .....</b>	<b>61</b>
<b>Figure 54: 10 MPH Moving Truck Deflection (Beam 8 – Instrument Line A).....</b>	<b>62</b>
<b>Figure 55: 35 MPH Moving Truck Deflection (Beam 8 – Instrument Line A).....</b>	<b>63</b>
<b>Figure 56: Maximum Dynamic and Static Deflection (Truck # 8).....</b>	<b>64</b>
<b>Figure 57: 10 MPH Moving Truck Deflection w/o Continuity Reinforcement (Beam 8 – Instrument Line A) .....</b>	<b>65</b>
<b>Figure 58: 35 MPH Moving Truck Deflection w/o Continuity Reinforcement (Beam 8 – Instrument Line A) .....</b>	<b>65</b>
<b>Figure 59: Max. Dynamic vs. Static (Truck #26) .....</b>	<b>66</b>
<b>Figure 60: Joint Effect (10 MPH).....</b>	<b>67</b>
<b>Figure 61: Joint Effect (35 MPH).....</b>	<b>67</b>
<b>Figure 62: Bottom Strain Profile Instrument Line H (Cylinder 1 – 100 K).....</b>	<b>70</b>
<b>Figure 63: Bottom Strain Profile Instrument Line H (Cylinder 2 – 100 K).....</b>	<b>71</b>
<b>Figure 64: Bottom Strain Profile Instrument Line H (Cylinder 3 – 100 K).....</b>	<b>72</b>
<b>Figure 65: Top Strain Profile Instrument Line H (All Cylinders) .....</b>	<b>73</b>
<b>Figure 66: Average Top Strain vs Load - Instrument Line H (All Cylinders).....</b>	<b>74</b>
<b>Figure 67: Flexural Cracking and Void Water Leakage .....</b>	<b>75</b>
<b>Figure 68: Concrete Crushing in Beam 1 .....</b>	<b>75</b>
<b>Figure 69: Flexural Cracking and Concrete Crushing in Beam 1 .....</b>	<b>76</b>
<b>Figure 70: Concrete Crushing and Buckling of Compression Reinforcement in Beam 9 ....</b>	<b>76</b>
<b>Figure 71: Flexural Cracking and Spalling of Concrete in Beam 9 .....</b>	<b>77</b>
<b>Figure 72: Deflection Profile Instrument Line E (Cylinder 1 – 100 K) .....</b>	<b>78</b>
<b>Figure 73: Deflection Profile Instrument Line D (Cylinder 1 – 100 K) .....</b>	<b>78</b>
<b>Figure 74: Deflection Profile Instrument Line E (Cylinder 2 – 100 K) .....</b>	<b>79</b>
<b>Figure 75: Deflection Profile Instrument Line D (Cylinder 2 – 100 K) .....</b>	<b>79</b>
<b>Figure 76: Deflection Profile Instrument Line E (Cylinder 3 – 100 K) .....</b>	<b>80</b>
<b>Figure 77: Deflection Profile Instrument Line D (Cylinder 3 – 100 K).....</b>	<b>80</b>
<b>Figure 78: Deflection Profiles Instrument Line E.....</b>	<b>81</b>
<b>Figure 79: Deflection Profiles Instrument Line D .....</b>	<b>82</b>
<b>Figure 80: Bottom Strain Profile Instrument Line E (Cylinder 1 – 100 K) .....</b>	<b>83</b>
<b>Figure 81: Bottom Strain Profile Instrument Line E (Cylinder 2 – 100 K) .....</b>	<b>84</b>
<b>Figure 82: Bottom Strain Profile Instrument Line E (Cylinder 3 – 100 K) .....</b>	<b>84</b>
<b>Figure 83: Total Load and Instrument Line E Deflection (Center Span) .....</b>	<b>85</b>
<b>Figure 84: Total Load and Instrument Line D Deflection (Center Span).....</b>	<b>86</b>
<b>Figure 85: Total Load and Instrument Line E Average Deflection (Center Span).....</b>	<b>87</b>
<b>Figure 86: Total Load and Instrument Line D Average Deflection (Center Span).....</b>	<b>87</b>
<b>Figure 87: Beam 1 Failure.....</b>	<b>88</b>
<b>Figure 88: Buckling of Asphalt Overlay on Beams 1-3 .....</b>	<b>89</b>

<b>Figure 89: Failure of Shear Key .....</b>	<b>89</b>
<b>Figure 90: Spalling and Crushing of Beam 9 .....</b>	<b>90</b>
<b>Figure 91: Spalling and Cracking of Beams 8 and 9 .....</b>	<b>90</b>
<b>Figure 92: Crushing of Beam 8 Top Flange .....</b>	<b>91</b>
<b>Figure 93: Deflection Profile Instrument Line A (Cylinder 1 – 100 K) .....</b>	<b>92</b>
<b>Figure 94: Deflection Profile Instrument Line B (Cylinder 1 – 100 K) .....</b>	<b>92</b>
<b>Figure 95: Deflection Profile Instrument Line A (Cylinder 2 – 100 K) .....</b>	<b>93</b>
<b>Figure 96: Deflection Profile Instrument Line B (Cylinder 2 – 100 K) .....</b>	<b>94</b>
<b>Figure 97: Deflection Profile Instrument Line A (Cylinder 3 – 100 K) .....</b>	<b>94</b>
<b>Figure 98: Deflection Profile Instrument Line B (Cylinder 3 – 100 K) .....</b>	<b>95</b>
<b>Figure 99: Deflection Profiles Instrument Line A .....</b>	<b>96</b>
<b>Figure 100: Deflection Profiles Instrument Line B.....</b>	<b>96</b>
<b>Figure 101: Bottom Strain Profile Instrument Line A (Cylinder 1 – 100 K) .....</b>	<b>97</b>
<b>Figure 102: Bottom Strain Profile Instrument Line A (Cylinder 2 – 100 K) .....</b>	<b>98</b>
<b>Figure 103: Bottom Strain Profile Instrument Line A (Cylinder 3 – 100 K).....</b>	<b>98</b>
<b>Figure 104: Total Load and Instrument Line A Deflection (West Span) .....</b>	<b>99</b>
<b>Figure 105: Total Load and Instrument Line B Deflection (West Span) .....</b>	<b>100</b>
<b>Figure 106: Total Load and Instrument Line A Average Deflection (West Span).....</b>	<b>101</b>
<b>Figure 107: Total Load and Instrument Line A Deflection after Shimming (West Span) .</b>	<b>102</b>
<b>Figure 108: Total Load and Instrument Line B Deflection after Shimming (West Span) .</b>	<b>103</b>
<b>Figure 109: Total Load and Instrument Line A Average Deflection after Shimming (West Span).....</b>	<b>104</b>
<b>Figure 110: Average Top Strain vs. Load - Instrument Line A (All Cylinders).....</b>	<b>104</b>
<b>Figure 111: Shear Key Failures Between Beams 8-9 and 6-7 Prior to Collapse (West Span).....</b>	<b>105</b>
<b>Figure 112: Shear Key Failures Between Beams 8-9 and 6-7 Prior to Collapse (West Span).....</b>	<b>105</b>
<b>Figure 113: Shear Key Failure between Beams 3 and 4 Prior to Collapse (West Span).....</b>	<b>106</b>
<b>Figure 114: Collapsed Bridge (West Span w/ Frame) .....</b>	<b>107</b>
<b>Figure 115: Collapsed Bridge (West Span w/o Frame) .....</b>	<b>107</b>
<b>Figure 116: Collapsed Bridge (West Span w/o Frame) .....</b>	<b>108</b>
<b>Figure 117: Fractured Transverse Bar (West Span) .....</b>	<b>108</b>
<b>Figure 118: Average Mid-span Deflections vs. Load (Center &amp; West Spans) .....</b>	<b>109</b>
<b>Figure 119: Average Mid-span Top Strain vs. Load (East &amp; West Spans).....</b>	<b>110</b>
<b>Figure 120: Center Span Beam 7 (100 kip Cylinder 3) .....</b>	<b>117</b>
<b>Figure 121: Center Span Beam 8 (100 kip Cylinder 3) .....</b>	<b>118</b>
<b>Figure 122: Meshed Beam.....</b>	<b>119</b>
<b>Figure 123: User Defined Node Sets for Load Locations .....</b>	<b>121</b>
<b>Figure 124: FEM and Experimental Deflections Cylinder 1 (West Span) .....</b>	<b>122</b>
<b>Figure 125: FEM and Experimental Deflections Cylinder 2 (West Span) .....</b>	<b>123</b>
<b>Figure 126: FEM and Experimental Deflections Cylinder 3 (West Span) .....</b>	<b>123</b>
<b>Figure 127: FEM and Experimental Strains Cylinder 1 (West Span).....</b>	<b>124</b>
<b>Figure 128: FEM and Experimental Strains Cylinder 2 (West Span).....</b>	<b>125</b>
<b>Figure 129: FEM and Experimental Strains Cylinder 3 (West Span).....</b>	<b>125</b>
<b>Figure 130: FEM Damaged, Undamaged and Experimental Strains Cylinder 2 (West Span) .....</b>	<b>126</b>

## LIST OF TABLES

<b>Table 1: Truck Loads (7/15/10 Test) .....</b>	<b>28</b>
<b>Table 2: Truck Loads (7/28/10 Test) .....</b>	<b>31</b>
<b>Table 3: Live Load Factors for Legal Load .....</b>	<b>44</b>
<b>Table 4: Strength I Load Factors .....</b>	<b>47</b>
<b>Table 5: IMF Corrosion Estimates for Tracks 3I and 7I.....</b>	<b>58</b>
<b>Table 6: Comparison of Strand Loss to MFL and IMF Methods .....</b>	<b>58</b>
<b>Table 7: Concrete Core Test Results.....</b>	<b>68</b>
<b>Table 8: Chloride Test Results.....</b>	<b>69</b>
<b>Table 9: Cylinder Load Distribution (East Span).....</b>	<b>73</b>
<b>Table 10: Cylinder Load Distribution (Center Span) .....</b>	<b>85</b>
<b>Table 11: Cylinder Load Distribution (West Span).....</b>	<b>99</b>
<b>Table 12: Cylinder Load Distribution after Shimming (West Span).....</b>	<b>102</b>
<b>Table 13: AASHTO Standard Specifications Beam Capacity .....</b>	<b>111</b>
<b>Table 14: AASHTO Standard and Experimental Bridge Capacity .....</b>	<b>111</b>
<b>Table 15: AASHTO LRFD Beam Capacity.....</b>	<b>112</b>
<b>Table 16: AASHTO LRFD and Experimental Bridge Capacity .....</b>	<b>113</b>
<b>Table 17: LFR Rating Factors (Simply Supported) .....</b>	<b>113</b>
<b>Table 18: LFR Rating Factors (Continuous for Live Load).....</b>	<b>114</b>
<b>Table 19: LRFR Results (Simply Supported) .....</b>	<b>115</b>
<b>Table 20: LRFR Rating Factors (Continuous for Live Load) .....</b>	<b>115</b>
<b>Table 21: Experimental Distribution Factors .....</b>	<b>116</b>

# 1. INTRODUCTION

## 1.1 Purpose

This report describes the results from the testing of a full scale three span 43 year old adjacent prestressed concrete box beam bridge. This research is the second phase of the overall project entitled “Structural Evaluation of LIC-310-0396 Box Beams with Advanced Strand Deterioration” (State Job #134381). The first phase involved the forensic study and destructive testing of damaged individual beams removed from a similar type of bridge and described in the Interim - Phase I report. The results of Phase I showed the differences in behavior of the damaged beams on an individual basis.

However, these beams do not exist in bridges as single members. Unfortunately, the research does not currently provide experimental results for the complete adjacent box beam bridge system behavior. The evaluation of the behavior of the complete bridge system is critical for several reasons. The first reason is related to the robustness of the structural system for adjacent box beam bridges. For typical deck and girder bridges, the girders are spaced at distances of 6-9 feet (1.8-2.7m) with the bridge deck spanning in between the girders. For adjacent box beam bridges, the beams are placed adjacent to each other and tied together through shear keys as well as transverse tie rods. This adjacent placement causes a significant difference in the behavior of the beams in the bridge system compared to an individual beam. Though design standards provide analytical procedures to determine how loading transfers between the various beams, experimental evidence of these procedures is limited. In addition, determining how loads transfer in the beams of this structural system when members are damaged from deterioration does not exist analytically or experimentally. Typically, evaluation of damaged members are done assuming loads distribute to them as if they are not damaged.

This lack of analytical and experimental verification on the behavior of damaged prestressed box beam bridge systems is related to economics. An overly conservative approach to evaluating a bridge based on individual member capacity and undamaged load distribution behavior may lead to premature load restriction of the bridge, closing of the bridge, or replacement of the bridge. In addition, replacement of a bridge may be considered necessary when in fact a more economical solution may be repair of the bridge to extend its service life. Finally, not completely understanding the behavior of the bridge system compared to individual member behavior could lead to unexpected premature failure leading to damage of public property, personal injury, or worse. It has been noted that during removal of some damaged beams, collapse of the beams under their own weight have occurred once shear keys and transverse ties have been cut. If such a condition occurred in an operational bridge and went unnoticed, the consequences could be disastrous.

## 1.2 Objectives

The primary objective of the study was to test and analyze an existing full scale damaged prestressed concrete adjacent box beam bridge. This included:

1. Nondestructive evaluation of the bridge.
2. Destructive field testing of the full scale damaged bridge.
3. Data analysis of the experimental testing.
4. Analytical assessment of the field tested bridge.

5. Summarize the results of the study in a final report to ODOT.  
Each task is explained in more detail below.

### **1.3 Tasks**

In order to meet the objectives of the study, the project involved a variety of tasks. The nondestructive testing involved the use of ground penetrating radar to assess the concrete of the bridge, a magnetic method to evaluate the procedure of the method on a small portion of the bridge for prestressing strand corrosion, and truck testing to determine initial behavior of the bridge prior to destructive testing. The destructive field testing of the 3 span bridge involved instrumenting and testing each span individually. One span was left in its existing condition to serve as a control while the two other spans were damaged to varying magnitudes prior to testing. The data from the nondestructive and destructive testing was analyzed and comparisons were made to evaluate the behavior of the bridges and damage. The bridge was assessed analytically using standard design procedures, as well as with simple and complex computer software. Load rating of the bridge was also performed.

## 2. BACKGROUND

### 2.1 Bridge Details

A bridge was identified with the assistance of the ODOT technical liaison, Mike Loeffler and County Engineer, Steve Lubbe. The bridge was located in Fayette County and was slated for replacement in 2010. The bridge was located on County Road 35 (FAY 35- 17-6.80) northeast of the city of Washington Court House. The bridge was put into service in 1967, making it 43 years old at the time of testing. The bridge had three spans and crossed the North fork of Paint Creek (see Figure 1). According to the plans each span was 47' 10" (14.6 m) in length with a left forward 15° skew (see Figure 2). Transverse ties, 1" (25 mm) in diameter, were located approximately at the third points of the spans. Each span consisted of nine prestressed concrete box beams. For this research project, the spans were referred to as the east, center and west span and the beams in each span were number 1-9 from south to north.

The beams were 21" (533 mm) deep and 36" (914 mm) wide with flanges and webs 5" (127 mm) thick. The voids were created with cardboard forms and drawings for the bridge showed a total of 27 - 3/8" (9.5 mm) diameter 250 ksi (1,723 MPa) prestressing strands though a note called for 29 strands. A total of 3 rows of strands existed, with 14 strands in the bottom row, 9 strands in the middle row and 4 strands in the top row. Mild reinforcement also existed at the top of the beam in the form of 4 - #5 (16M) bars (see Figure 3). Shear reinforcement on the bottom of the beam consisted of 6 - #4 (13M) bars spaced at 7 1/2" (191 mm) at each end of the beam and then 15" (381 mm) throughout the remaining length of the beam. The shear reinforcement on the top of the beam consisted of #4 (13M) bars at 7 1/2" (191 mm) spacing. The bottom row of strands existed below the bottom shear reinforcement. The connection of the beams over the pier involved the lap splice of a #4 (13M) bar with a length of 2 feet (0.61 m) (see Figure 4).



**Figure 1: FAY 35-17-6.82**

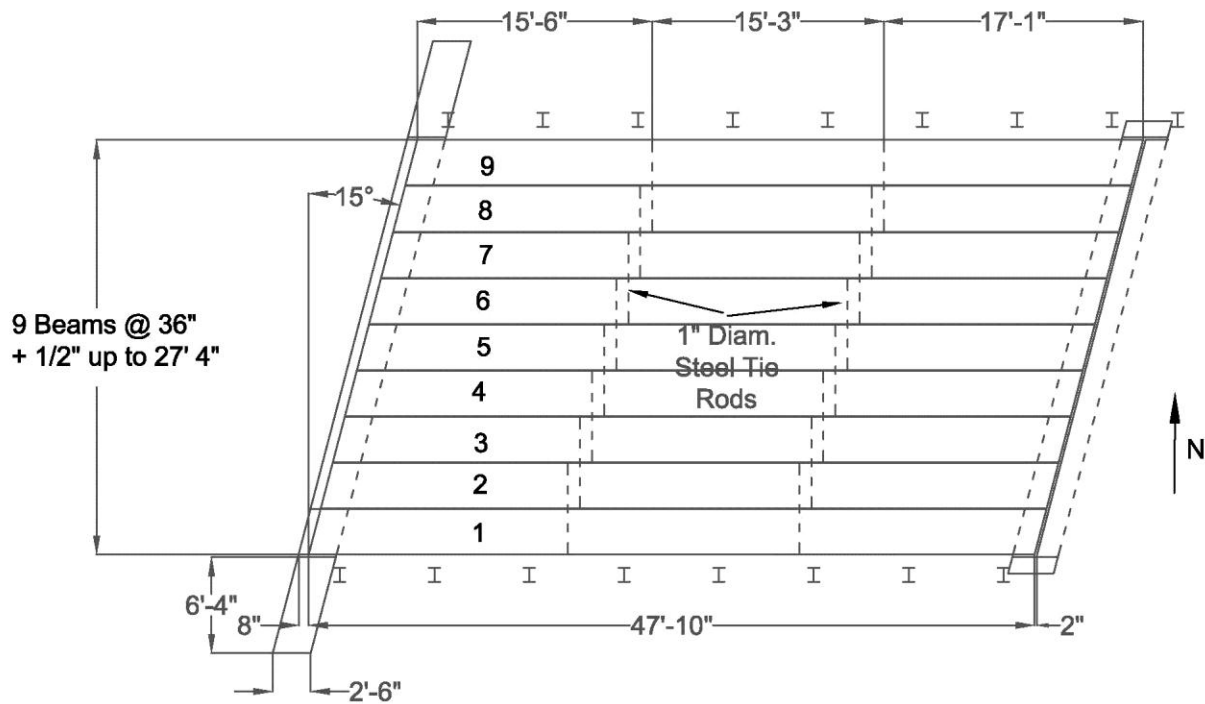


**Figure 2: FAY 35-17-6.82 Bridge Span**

(Note: 1' = 0.305 m)

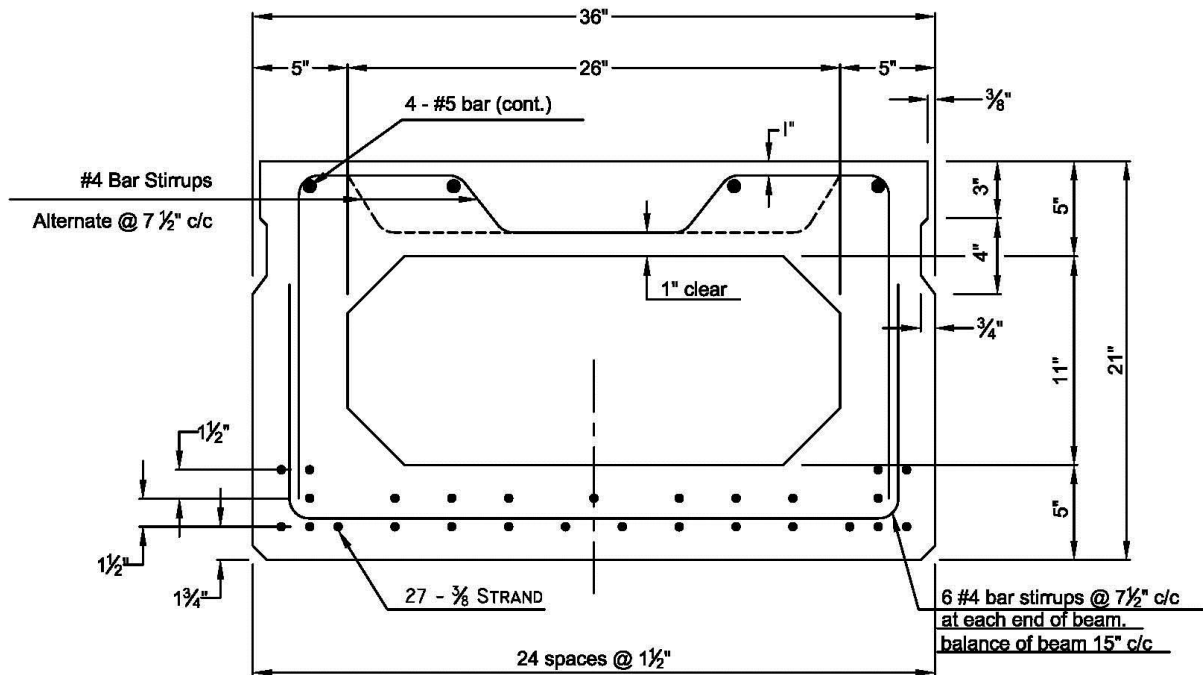


**Figure 3: FAY 35-17-6.82 Beam Section**

(Note: 1" = 25.4 mm)

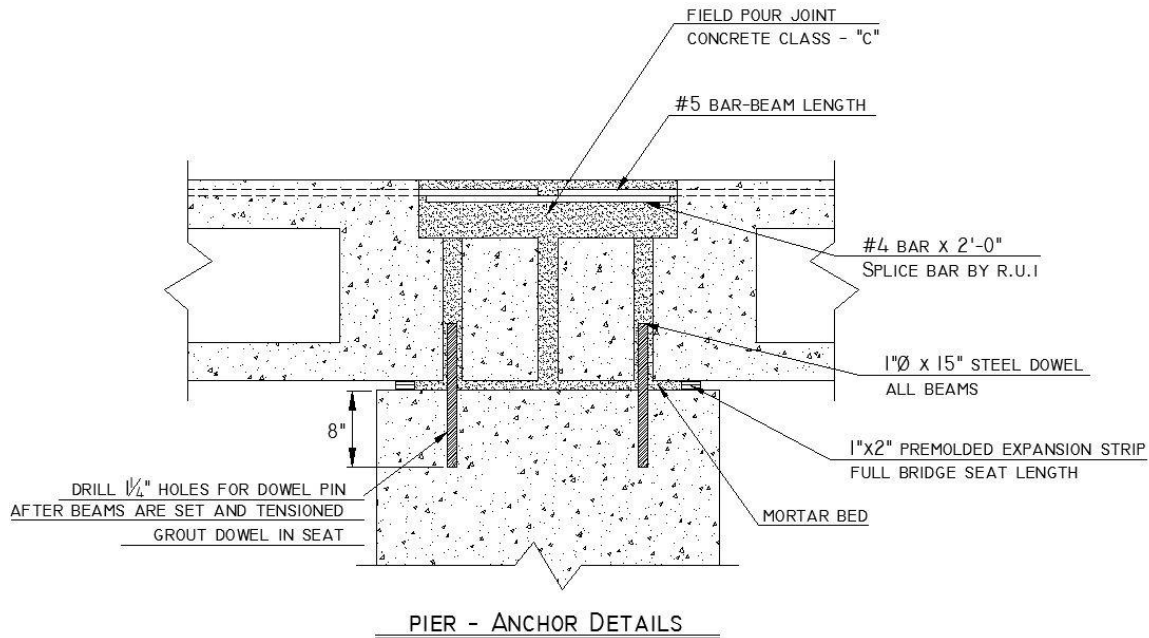


**Figure 4: FAY 35-17-6.82 Pier Detail**  
 (Note: 1" = 25.4 mm)

## 2.2 Nondestructive Evaluation

Nondestructive evaluation provides means of evaluation without damaging or causing minimal damage to the structure. Various nondestructive testing methods exist to investigate a variety of aspects of a structure. The evaluations could be visual or involve nondestructive testing techniques. The level of sophistication of the techniques can vary widely as well. The nondestructive testing techniques can include acoustic methods, electromagnetic methods, magnetic methods, and optical methods. Acoustical methods utilize sound waves of various frequency and include methods such as ultrasonic, impact-echo, and acoustic emission. The primary electromagnetic method is radar and utilizes the transmission and reflection of electromagnetic waves. Various frequency waves can be used depending on the type of evaluation being sought. Other electromagnetic methods include covermeter, capacitometry, electrical resistivity, potential field methods, and microwave methods (Maierhofer, et. al., 2010). Magnetic methods are primarily used to inspect prestressing strands. Concrete does not affect the methods unless ferromagnetic aggregates exist within the concrete. The methods include magnetic flux leakage and induced magnetic field methods. Optical methods include mapping and direct images of the surface such as photogrammetry, laser scanning, digital photography, and thermography.

### 2.2.1 Visual Inspection

Visual inspections on bridges are done on a yearly basis in the State of Ohio. The inspections ensure public safety, compliance with Federal and State regulations, and proper management of the bridges (Manual of Bridge Inspection, 2010). Visual inspections can vary in the degree of information being sought. Initial inspections are done new bridges before they are put into service to provide a baseline for future inspections. Routine inspections are primarily

used to determine changes in the bridges condition from previous inspections and to note items to evaluate in future inspections. The level of detail during the inspection is dependent on the type of bridge being evaluated and its existing condition. More in-depth inspections can be performed if necessary due to concerns or uniqueness of the entire bridge.

The results from a bridge inspection are recorded on the Bridge Inspection Report, form BR-86, and stored in ODOT Bridge Management System. The BR-86 form contains 66 items that are either given either a 1-4 rating number or a 0-9 condition rating. If the General Appraisal, item 66 on BR-86, is  $\leq 4$  (0-9 scale), then the bridge must be load rated based on the in-service condition of the bridge (Manual of Bridge Inspection, 2010).

For the FAY 35- 17-6.80 bridge used in this research, the outside beams were in very poor condition. The top flange separated from the lower portion of the beam for the north outside beam (Beam 9) of the west span (see Figure 5). The south outside beam (Beam 1) of the west span was in similar condition (see Figure 6). The stirrups were exposed for these outside beams of the west span. The top flange had been patched by the County some years prior to testing, but this was not completely successful. Beam 1 of the center span had some degradation of the top flange concrete (see figure 7) but was in relatively good condition. The north beam (Beam 9) of the center span was comparable to Beam 1 of the center span (see Figure 8). The south beam (Beam 1) of the east span had some separation of the top flange near the abutment (see Figure 9). The exterior beam on the north side of the east span also had separation of the top flange and strands exposed (see Figures 10 and 11).

The interior beams were in very good condition with the exception of Beam 3 on the east span (see Figure 12). The beam showed longitudinal cracking and some spalling of concrete near east pier. The spalling did not expose any strands, but staining was visible.



**Figure 5: Exterior North Beam (Beam 9) - West Span**



**Figure 6: Exterior South Beam (Beam 1) – West Span**



**Figure 7: Exterior South Beam (Beam 1) – Center Span**



**Figure 8: Exterior North Beam (Beam 9) – Center Span**



**Figure 9: Exterior South Beam (Beam 1) – East Span**



**Figure 10: Exterior North Beam (Beam 9) – East Span**



**Figure 11: Exterior North Beam (Beam 9) – East Span**



**Figure 12: Interior Beam 3 - East Span**

### **2.2.2 Ground Penetrating Radar**

Ground Penetrating Radar (GPR) is an electromagnetic technique and is also commonly referred to as surface penetrating radar, electromagnetic reflection or simply radar. The advantages to GPR are the speed of which the technique can be performed to obtain frequent data, its complete nondestructive effect on the structure, and the system does not have to be in direct contact with surface of the structure (Maierhofer, et. al., 2010). The basic principal of GPR involves the emission of an electromagnetic pulse into the structure from a transmitter. The pulse is reflected at the surface and the internal boundary layers within the structure and recorded by a receiver. GPR can be used to determine layer thicknesses, such concrete cover over rebar, locations of voids or reinforcement, and material properties. GPR has been used to evaluate the condition of pavements and bridge decks.

Nondestructive testing using a GPR system was performed on June 29. The top of all spans were evaluated and the bottoms of the end spans were also evaluated with GPR. The technique requires the scanning of the structural system be done in a direction transverse to the reinforcing steel nearest the surface. Therefore, the bottom of the spans required the beams to be scanned in a transverse direction since the prestressing strands were closest to the concrete surface. Access at some locations made use of the system difficult (see Figure 13). In addition, the longitudinal joints between the beams also resulted in difficulties.

Performing the radar on the top of the bridge was simpler and quicker because of the easier access and allowed for a better sampling system to be used. However, there were still some issues with using the GPR on the top of the bridge. The scanning had to be performed

longitudinally (see Figure 14) due to the shear steel reinforcement being closest to the surface. Unfortunately, the shear steel drops in the middle of the beam (see Figure 3), which affects the data.



**Figure 13: GPR – Bottom**



**Figure 14: GPR – Top**

### 2.2.3 Magnetic

Magnetic methods have been successfully used in determining hidden corrosion in embedded strand in prestressed concrete and to identify fractures in prestressing strands. In this research project, a comparison of two magnetic methods, the Magnetic Flux Leakage (MFL) and the Induced Magnetic Field (IMF), was evaluated by the University of Toledo personnel on a small portion of the test bridge.

For the MFL method, an external magnetic field is applied to reinforced or prestressed concrete members. The flux within the reinforcing or prestressing steel remains unchanged until it must leave the steel to travel back to the south pole of the second magnet. If the flux encounters a flaw such as a corroded area, broken strand, or complete fracture, some or all of the flux leaks out of the steel. This magnetic flux leakage is detected by one or more sensors and is analyzed to determine the extent or severity of the discontinuity. The distance between the sensor and the steel has a damping effect on the magnitude of the flux leakage due to the presence of discontinuities in the steel. The induced magnetic field strength needs to be adequately large to cause considerable magnetic flux leakage to occur when there are small defects in the steel. As a result, small flaws in the steel cannot be detected using the MFL concept. The MFL method was recently examined by researchers at Lehigh University to determine hidden corrosion in sections of damaged box beams (Naito, 2010).

The primary component of the MFL system is a modular unit called the sensing head that is comprised of two permanent magnets and a series of Hall effect sensors that are housed in a protective box between the magnets, as shown in Figure 15. The sensing head is installed on a beam rider unit under the bridge to be inspected. The inspection is done by moving the magnet head to scan under the bridge while the Hall sensors simultaneously measure magnetic field. This data is acquired by the data acquisition software and recorded in a computer where it can be analyzed for magnetic leakage field. The process of acquiring and recording the data is simultaneous and the live run can be observed in a computer. Dr. Ghorbanpoor of the University of Wisconsin performed the MFL under the direction of the University of Toledo.



**Figure 15: MFL Sensing Equipment**

The IMF detection technique involves magnetization of the strand, such that the magnetic flux induced in it is near a level of magnetic saturation. This induced magnetic flux would depend on the amount of sound cross-sectional area of steel and thus give a measure of the sound cross-

sectional area of the strand. Corrosion can be inferred as a change in cross-sectional area. The change in magnetic induction with the change in cross-sectional area of steel due to corrosion can be correlated to estimate corrosion in terms of mass loss of steel. A non-corroded specimen has a higher effective sound cross-sectional area compared to a corroded specimen with the same original diameter. In other words, a non-corroded rod would be induced with a magnetic field higher in magnitude than a corroded one. The magnetized tendons will have a magnetic field proportional to the sound cross-sectional area of the tendon itself. The University of Toledo has been working on developing a new electromagnetic based sensor to determine the sound condition of steel in prestressing strand using induced IMF magnetic field technique. The setup contains a yoke-shaped electromagnet with hall sensors on its pole face to sense induced magnetic field. This electromagnet is used to magnetize the prestressing strands located majorly in the bottom of the bridge, by scanning under the bridge. The setup can be seen in Figure 16.

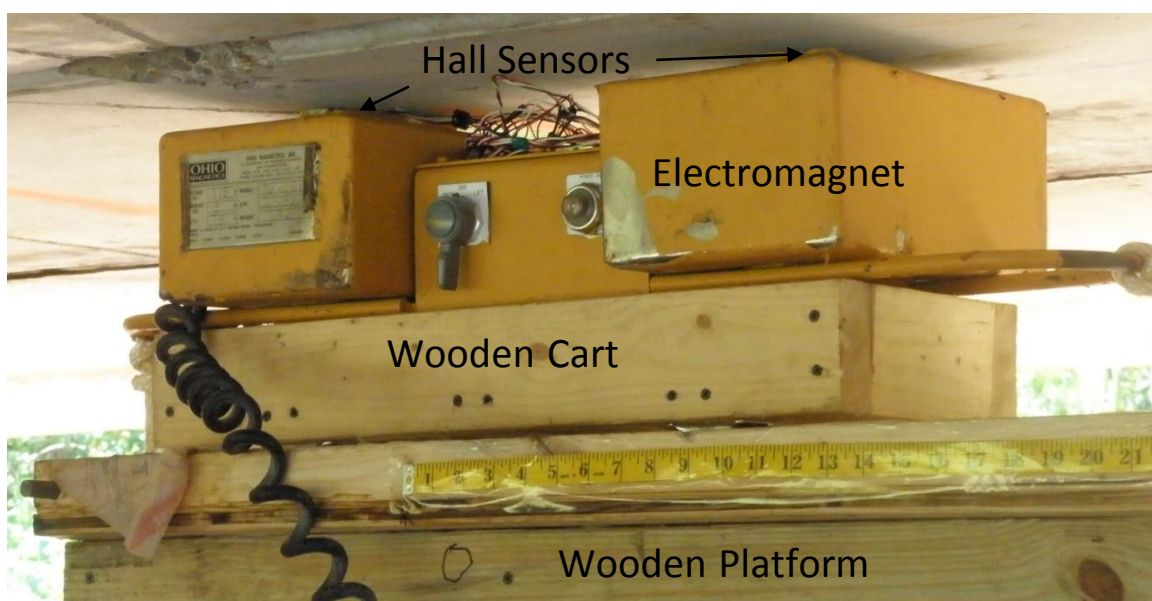


**Figure 16: University of Toledo IMF Sensor**

## 2.2.4 Truck Testing

Truck testing, also referred to as load testing, is a means of determining the behavior of a bridge based on a known truck weight (loading). Deflections and/or strains are measured with sensors to determine the behavior of the bridge statically and/or dynamically. This type of testing has been performed by numerous researchers on a variety of bridges. However, the difficulty of this testing is the loading is often minimal relative the bridge capacity in order to assure no damaged is incurred during testing.

One of the more relevant truck loading research projects to this research was performed by Case Western Reserve University for ODOT (Hucklebridge, et. al., 1993). This project involved placing a truck of known weight on six adjacent box beam bridges and measuring the relative movement between beams as well as the bending strains in the beams. The bridges ranged in age of less than 1 year old to 16 years old. A total of 4 of the bridges were non-composite and 2 were composite. The research concluded from field observations and analytical study that the relative displacement between adjacent beams should not exceed 0.001" (0.0254

mm) if the shear key is fully intact. The bridges monitored in the study all showed relative displacements of adjacent beams in excess of 0.001" (0.0254 mm) and were in the range of 0.003" (0.0762 mm) to 0.024" (0.610 mm). This led the authors to conclude that at least a portion of the shear keys had fracture.

On July 14, instrumentation was installed on the west span of the FAY 35-17-6.80 bridge used in this research. The installation of the instrumentation involved grinding the asphalt off the top surface of the full width of the bridge at two locations down to the top of the beams. The trenches from the asphalt removal was approximately 2 feet (0.61 m) wide to allow the grinding machine to penetrate deep enough for the complete removal of the asphalt. Figure 17 shows one the trenches ready for installation of instrumentation.



**Figure 17: Asphalt Removed**

The top surfaces of the beams were then prepared by minor grinding, sanding and cleaning. Encased electrical resistant strain gages were then installed using an adhesive and allowed to cure (see Figure 18). One strain gage was mounted on each beam for each of the two instrument trench lines. The locations of the two instrumentation lines are shown in Figure 19. Instrument line A was slightly off of midspan in order to assure room for load placement during

destructive testing. Instrument line B was near the inflection point if full continuity existed over the pier. Wiring from the gages was run to the edge of the bridge to allow for connection to a data acquisition system. Cold patch was then placed on top of the gages, tamped, and compacted to return the bridge to a drivable surface (see Figure 20).



**Figure 18: Installed Strain Gage**

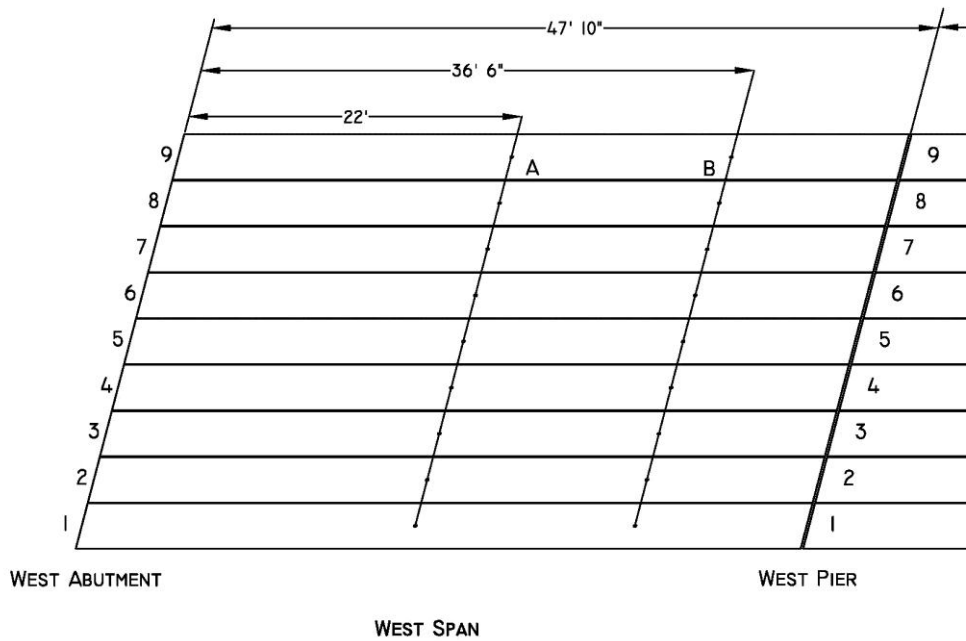


**Figure 19: Instrumentation Locations**

(Note: 1 ft. = 0.305 m)



**Figure 20: Cold Patch Placement**

The bottom surfaces of the beams were also sanded and cleaned to allow for the installation of strain gages. Two small frames were also erecting beneath the west span to support string potentiometers in order to measure deflections (see Figure 21). Small anchors were drilled into the beams so the wires of the string potentiometers could be attached to the beams. Wiring from the strain gages, as well as the string potentiometers, was run along the frames to the edge of the bridge near the wiring from the top gages. A single strain gage and one string potentiometer was mounted to each beam along two instrumentation lines A and B matching the instrumentation lines for the top surface.



**Figure 21: Instrumentation and Supporting Frame**

Truck testing on west span was performed on July 15. Instrumentation was connected to a high speed data acquisition system capable of reading each sensor 100,000 times per second (see Figure 22). All sensors were tested, verified, and zeroed before trucks were placed on the bridge. The Fayette County Engineer's office provided 4 loaded trucks. Wheel loads were measured with scales before the placement of the trucks on the bridge. A summary of the truck loads is provided in Table 1.

The trucks were placed in static positions at several locations on the west span of the bridge. Figure 23 shows the positioning of Truck #8 on the west span for Truck Load Case 1. This was to produce large positive moments as well as investigate transverse distribution of the loads for a single truck (see Figure 23). It was also used to compare static and dynamic loading on the bridge as will be discussed shortly. Truck Load Case 4 was the positioning of all trucks to produce the largest positive moment as well as investigate transverse distribution of the loads for multiple trucks (see Figures 24 and 25). The trucks were also positioned on the west and center spans simultaneously to produce significant negative moments to check for continuity over the pier for Truck Load Case 5 (see Figures 26 and 27). Truck Load Cases 2 and 3 were similar to Truck Load Cases 4 and 5, respectively, but the trucks were placed in the lanes and not to the furthest southern positions as possible.



**Figure 22: Data Acquisition System**

**Table 1: Truck Loads (7/15/10 Test)**

Truck #		Weight (kips)		
		Left	Right	Axle
8	Front	7.35	7.25	14.60
	Rear (Front)	9.80	11.15	20.95
	Rear (Back)	10.05	11.20	21.25
	Total			56.80
31	Front	5.40	6.65	12.05
	Rear (Front)	9.80	11.50	21.30
	Rear (Back)	10.00	11.30	21.30
	Total			54.65
41	Front	7.50	6.90	14.40
	Rear (Front)	9.45	10.70	20.15
	Rear (Back)	8.85	10.75	19.60
	Total			54.15
47	Front	7.25	7.25	14.50
	Rear (Front)	9.15	9.60	18.75
	Rear (Back)	8.95	9.55	18.50
	Total			51.75
All			217.35	

(Note: 1 kip = 4.45 kN)

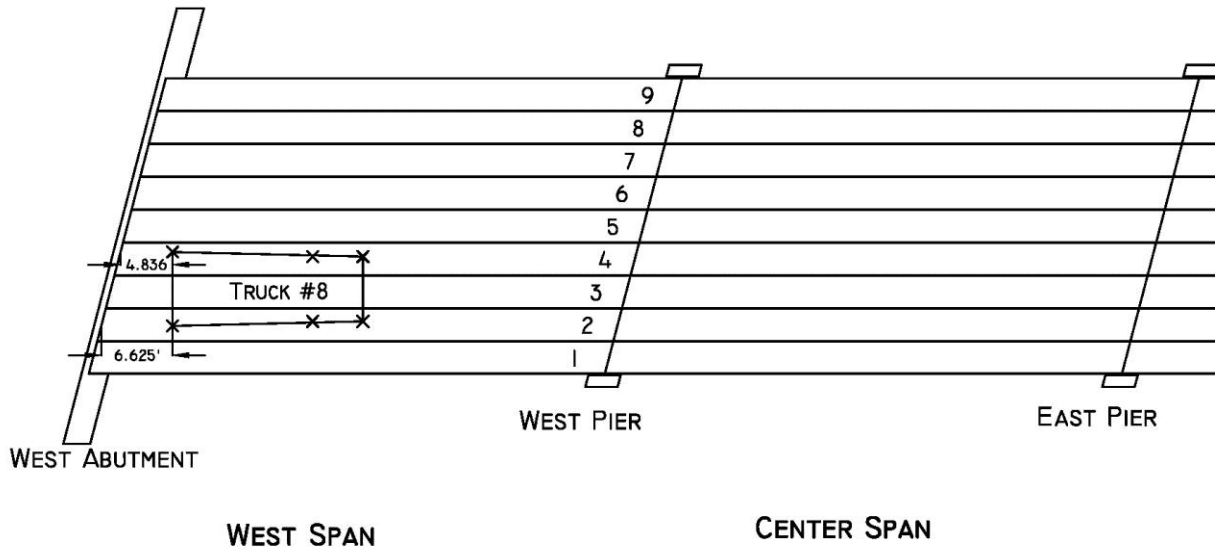


**Figure 23: Truck Load Case 1**

(Note: and 1' = 0.305m)

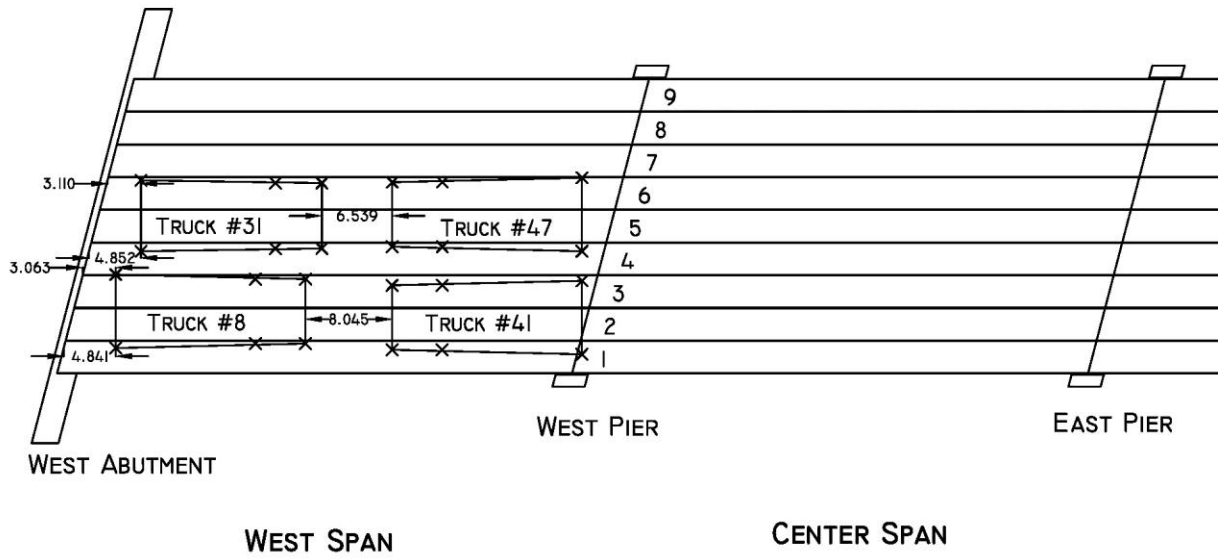


**Figure 24: Truck Load Case 4**  
 (Note: and 1' = 0.305m)



**Figure 25: Truck Loading (Max +M)**

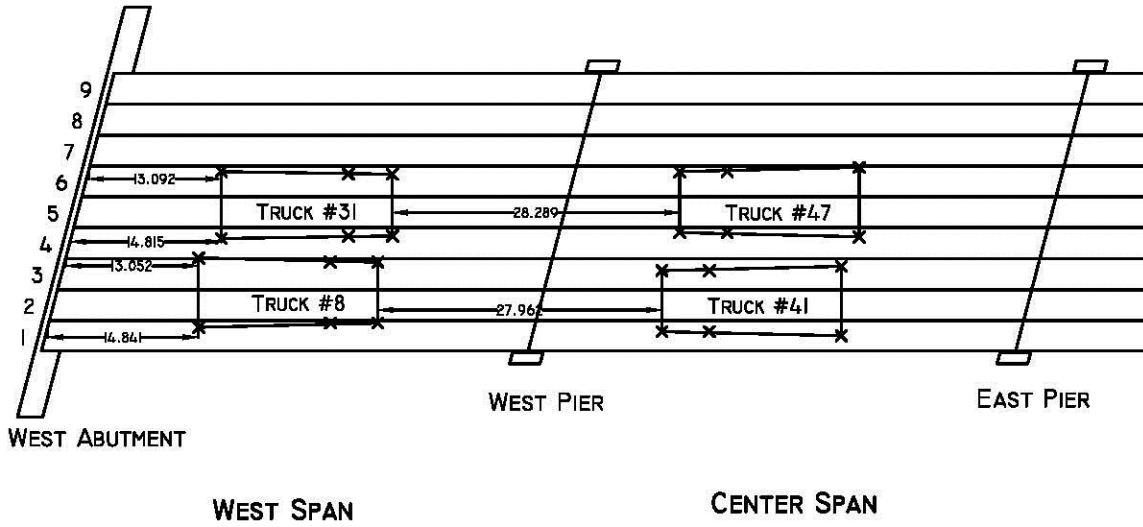


**Figure 26: Truck Load Case 5**  
 (Note: and 1' = 0.305m)



**Figure 27: Truck Loading (Max -M)**

Truck testing was performed again on July 28 after cutting the continuity reinforcement over the pier between the west and center spans. The truck loads for this test are summarized in Table 2. Truck Load Case 6 placed all the trucks in the center span (see Figure 28). This was

done to see if any deflection or strain would be measured in the west span to determine the degree of continuity that still existed, if any. Truck Load Cases 7 and 8 (see Figures 29 and 30) were similar to Truck Load Cases 4 and 5, respectively, to investigate the level of continuity after cutting the reinforcement over the west pier. Upon completion of the static truck loading, a single truck was driven across the bridge at two speeds of approximately 10 and 35 MPH while monitoring instrumentation. This was to investigate dynamic loading effect and the associated load distribution on the bridge.

**Table 2: Truck Loads (7/28/10 Test)**

Truck #		Weight (kips)		
		Left	Right	Axle
7	Front	7.00	6.85	13.85
	Rear (Front)	10.55	9.95	20.50
	Rear (Back)	10.35	9.40	19.75
	Total			54.10
26	Front	8.90	9.00	17.90
	Rear (Front)	12.25	9.35	21.60
	Rear (Back)	10.75	8.35	19.10
	Total			58.60
57	Front	5.70	5.00	10.70
	Rear (Front)	11.45	9.45	20.90
	Rear (Back)	10.95	8.35	19.30
	Total			50.90
86	Front	5.90	5.80	11.70
	Rear (Front)	10.90	9.45	20.35
	Rear (Back)	10.95	9.35	20.30
	Total			52.35
All				215.95

(Note: 1 kip = 4.45 kN)

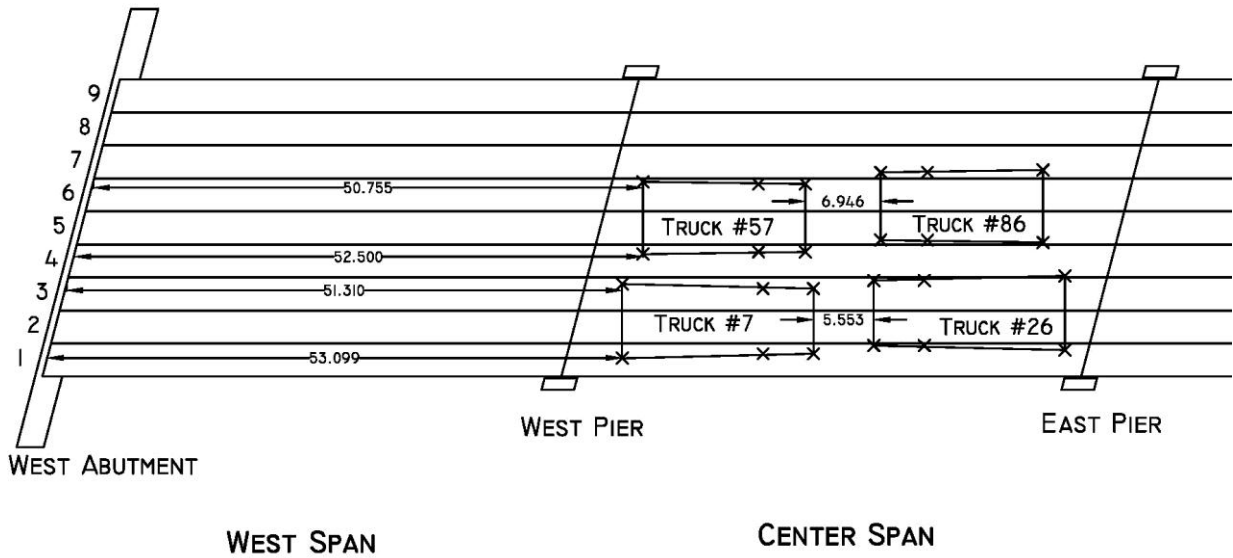


**Figure 28: Truck Load Case 6**  
 (Note: and 1' = 0.305m)

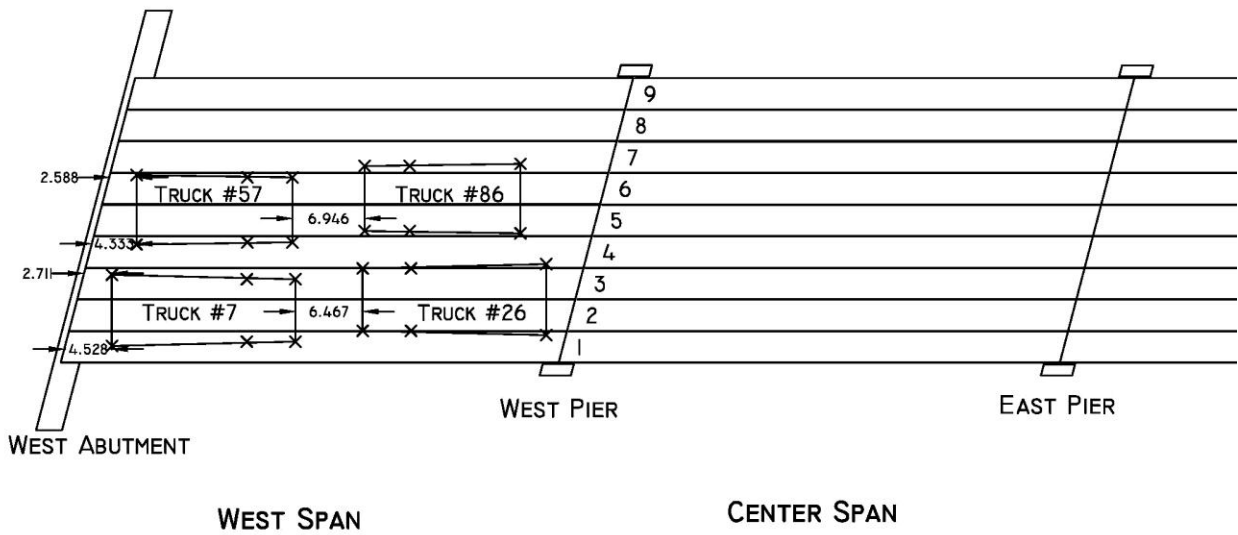


**Figure 29: Truck Load Case 7**  
 (Note: and 1' = 0.305m)

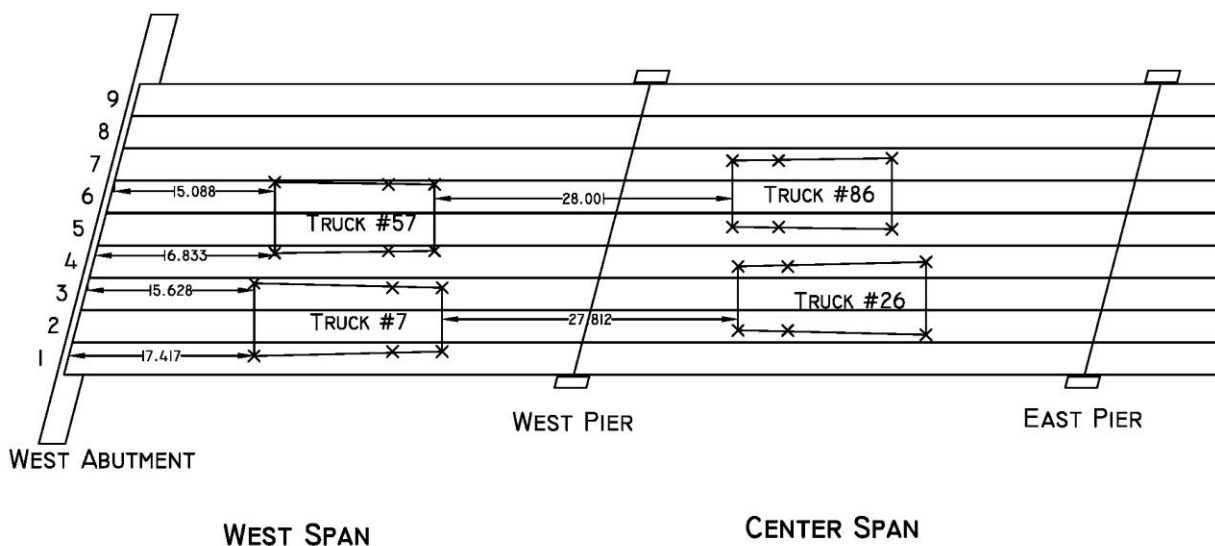


**Figure 30: Truck Load Case 8**  
(Note: and 1' = 0.305m)

## 2.3 Destructive Testing

There is little information in the literature in regards to field testing full scale bridges to failure. Scalon and Mikhailovsky (1987) tested a 34 year old slab and tee-beam bridge in Alberta, Canada to failure. Researchers performed destructive field tests on a three span, skewed, reinforced concrete slab bridge with the intent to develop quantitative evaluations for damaged bridges (Miller, et. al., 1994). In South Korea, researchers used a specially designed loading system to destructively test one 98.4 foot (30 m) span from a 12 span post-tensioned prestressed concrete girder bridge (Oh, et., al., 2002). In China, researchers overloaded a 43 year old concrete single span bridge with hydraulic jacks (Zhang, et. al., 2011). Unfortunately, none of these full scale destructive tests involved adjacent prestressed concrete box beam bridges.

Research has been carried out on the destructive testing of single deteriorated members removed from bridges that have been in service, as was done in Phase I of this project (Steinberg and Miller, 2011) and also by others (Harries, 2009; Harries, et., al., 2006; Labia, et., al., 1997; Miller and Parekh, 1994). A four beam full scale assembly intended to model a portion of a bridge was also tested to evaluate different shear key assemblies (Miller, et. al., 1999). Though these test programs provide some insight, they do not provide data for the behavior of a complete bridge.

### 2.3.1 Test Setup

In order to perform the destructive testing in this research, three steel test frames were designed and fabricated. Each steel test frame consisted of two W36 x 260 longitudinal beams approximately 50 feet (15.3 m) in length and spaced 18" (457 mm) apart. Each end of each frame was supported on two W33 x 118 approximately 4'6" (1.37 m) in length and spaced

approximately 4" (102 mm) apart. Figure 31 shows the frames in place on the first span. These test frames required a variety of fabrication such as drilling holes for bolts, welding in stiffeners, and splicing in pieces to meet the required length. A hydraulic cylinder with a capacity of 350 kips (1,558 kN) was mounted between each test frame. Therefore, the total load that could be placed on the bridge was 1,050 kips (4,673 kN). Figure 32 shows one of the cylinders mounted in a test frame.



**Figure 31: Test Frames on Span 1**



**Figure 32: Hydraulic Cylinder**

To assure the frames were not going to lift off the bridge during the application of load, the test frames were anchored through the abutment or pier. This was achieved by coring through the pier/abutment and anchoring a 1 3/4" (44.5 mm) Dywidag post tensioning Threadbar with an ultimate capacity of 400 kips (1,780 kN) at each end of the frame. The Threadbars were anchored to the top of the W33 x 118 and the bottom of the abutment/pier with plates and nuts as shown in Figures 33 and 34.



**Figure 33: Abutment Test Frame Anchorage**



**Figure 34: Pier Test Frame Anchorage**

The load from the cylinders was transferred into two small W6x25 spreader beams. The length of the spreader beams was approximately 6 feet (1.83 m) for the east span. The lengths were reduced for the center and west span testing to 4 feet (1.22 m) to concentrate the load more.

## 2.3.2 Testing Procedure

### 2.3.2.1 East Span

The setup for the destructive testing began on August 23, 2010 with the placement and erection of the test frames and the initiation of damage to the lower part of the east span. Erection of the test frames and damaging of the east span was completed on August 24. The following day the hydraulic system was tested and instrumentation was installed. The damaging of the bridge was performed by removal of concrete with jack hammers to expose the strands. The strands were then flame cut with a torch. Figure 35 shows some of the exposed and cut strands. The beams were numbered 1-9 from south to north. Damaging occurred near midspan for a length of approximately 50 in. (1.27 m) to 60 in. (1.53 m) and a width of approximately 9" (229 mm). Three bottom row strands on Beam 2 were cut near the interface with Beam 3. The first three strands on each edge of Beam 3 were cut. Damage to Beam 5 was similar to Beam 3 and Beam 6 had three strands cut near the interface with Beam 5. Therefore, a total of 18 strands were cut. Figure 36 shows the damage pattern for the east span. It should also be noted that Beam 3 had longitudinal cracking near the pier and Beam 9 had the exterior strand exposed and broken. Instrumentation was monitored during the cutting to see if any effect could be noticed.



**Figure 35: Exposed and Cut Strands – East Span**

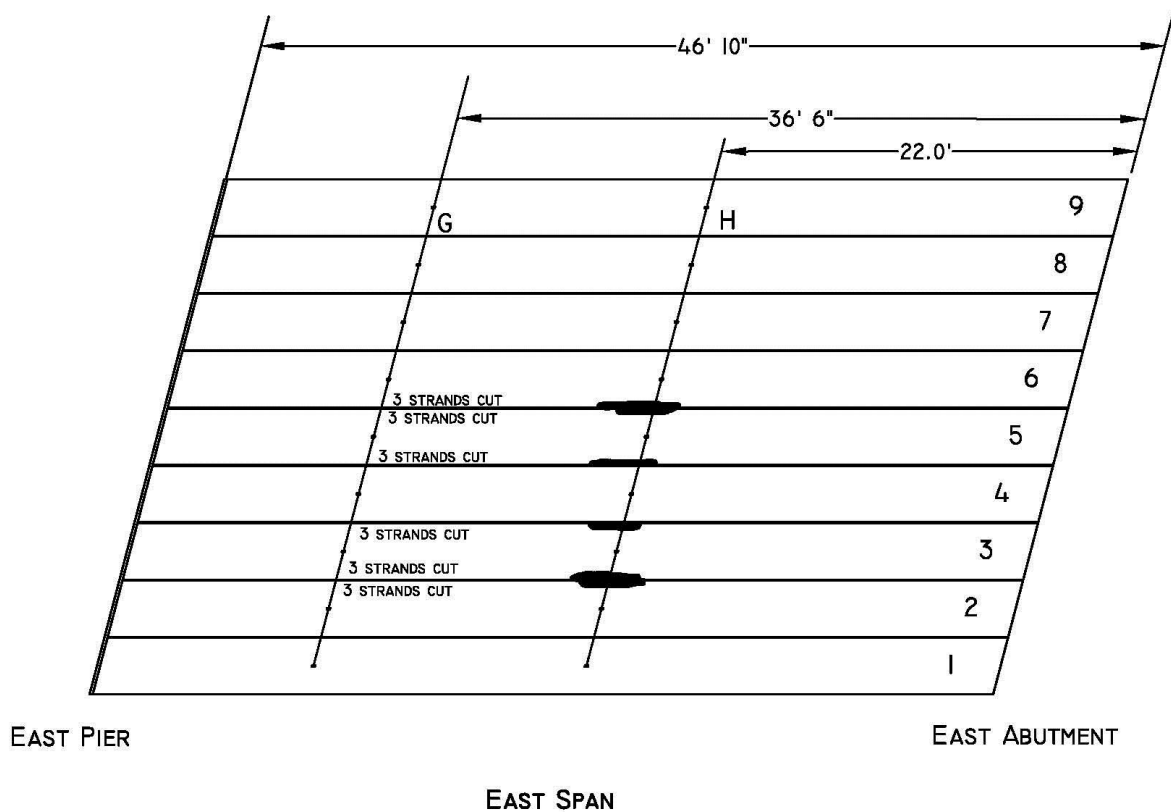


**Figure 36: Damage of East Span**  
 (Note: 1' = 0.305 m)

The instrumentation was installed along lines G and H. One strain gage was installed on the top and one on the bottom of each beam at each gage line. Asphalt was removed from the top surface down to the top of the beams as was done in the truck testing. However, cold patch was not placed over the gages because the bridge no longer needed to be reopened to traffic until the bridge was replaced. A small frame was erected on each side of the bridge and supported on the edge of the pier and the abutment as well as with a post at midspan. Steel tubes attached to the frames ran across the bridge along the instrument lines. String potentiometers were mounted to the steel tubes and the strings were attached to the bridge with anchors, one per beam per instrument line (see Figure 37). In addition, one string potentiometer was mounted between the steel tube and the test frame to monitor the deflection of the test frame. The instrumentation frame allowed deflections to be measured independent of bridge and test frame deformations. Mounting the string potentiometers on top of the bridge protected them from damage from spalling concrete or possible member / bridge failure during testing.



**Figure 37: Steel Tubes with String Potentiometers**

All instrumentation from the east span was connected to a high speed data acquisition system to monitor and record data during the testing. In addition, gages from the center span were also connected to the data acquisition system and monitored. These gages were on the bottom of beams 1, 4, 5 and 8 for instrument line E (see Figure 38).

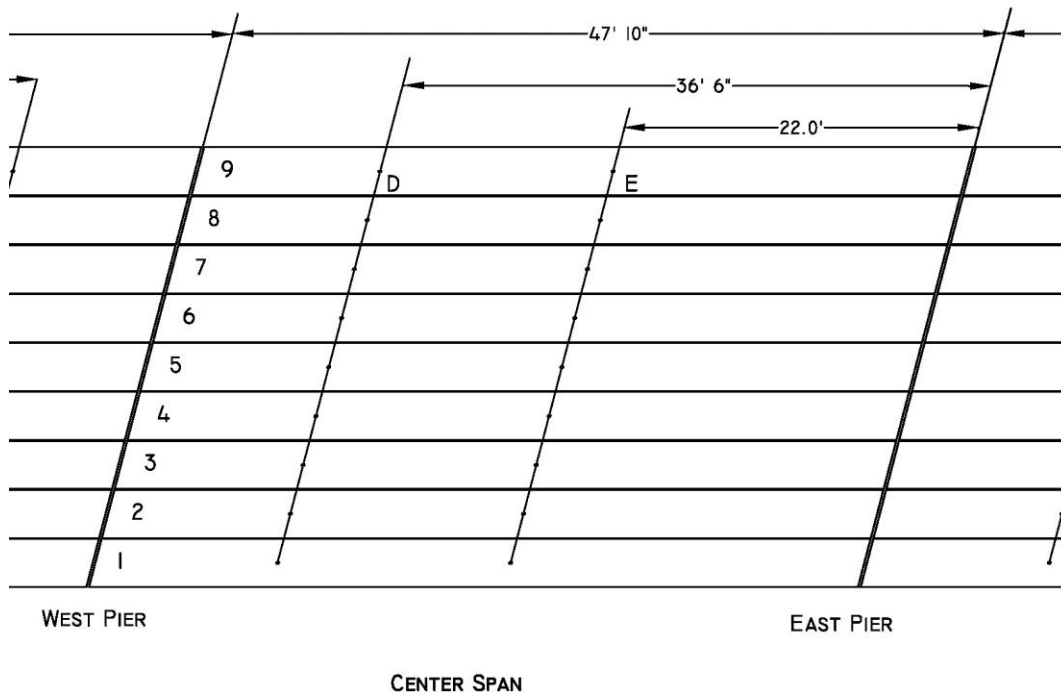


**Figure 38: Instrumentation Locations for Center Span**

(Note: 1' = 0.305 m)

Destructive testing of the east span occurred on August 26. Loading consisted of applying 50 kips (222.5 kN) of load to a cylinder, removing the load, applying 50 kips (222.5

kN) of load to another cylinder, and so on until each cylinder was loaded and unloaded. The process was repeated to a load of 100 kips (445 kN) per cylinder. A load of 50 kips (222.5 kN) was then applied to each cylinder consecutively without unloading, followed by an increment to 100 kips (445 kN) and so on until the bridge was no longer able to maintain additional load.

### **2.3.2.2 Center Span**

Movement of the testing frames to the center span occurred on August 27. Final installation of the instrumentation for the center span was completed on August 30. No damage of the center span was performed in order to obtain data for an undamaged span to serve as a control. In addition, only strain gages along instrument line E were mounted to the bottom of the bridge since this span was over water and had limited access. On the top surface, part of the asphalt was not removed and hence did not allow the installation of strain gages to Beams 1-3. The asphalt was not removed at the request of the County Engineer to see the effect of the asphalt overlay. A larger instrumentation frame was also used to support the steel tubes that ran across the bridge to support the string potentiometers. This was done since the frame had to be supported at the pier edges without any additional post in the middle. Fewer gages on the bottom of the beam allowed the monitoring of strain gages from the west span. A total of 16 strain gages were monitored from the west span. These strain gages included the top and bottom strain gages mounted on beams 2, 4, 5, and 8 for both instrument lines A and B. Destructive testing took place on August 31, 2010. Loading was similar to that performed on the east span. The application of load ceased once the bridge was no longer able to support additional load.

### **2.3.2.3 West Span**

The frame was moved to the west span on September 2. Preparation for instrumentation installation on the west span was initiated on September 7. On September 8, instrumentation was installed and damaging the underside of the bridge occurred. The damage was imposed by cutting through the bottom of the concrete and through all of the strands in the bottom row of the three center interior beams (Beams 4-6). Two cut lines were made approximately 3 feet (0.9 m) apart about the mid-span of the beams. This was to assure little to no redevelopment of the strands. Figure 39 shows the cuts through Beams 4-6. Some concrete was chipped away to assure the bottom row of strands were completely cut (Figure 40). Testing of the west span was performed on September 9. The placement of the testing frames along with the spreader beams resulted in cylinder 1 applying approximately 68% of its load to Beam 8 and the remaining 32% to Beam 7. Cylinder 2 applied approximately 69% of its load to Beam 5 and 32% to Beam 4. Cylinder 3 applied approximately 63% of its load to Beam 2 and 37% to Beam 1. Final disassemble and removal of the frame was done on September 10.



**Figure 39: Damage Created in Beams 4-6**



**Figure 40: Verification Strands Cut**

## 2.4 Load Rating

The purpose of bridge rating is to evaluate the remaining structural capacity of a bridge. The bridge rating is expressed as a ratio of the remaining live load capacity to a given live load demand. The ratio is known as the rating factor and is aimed to assist authorities in making decisions about the need for load posting, bridge strengthening, overweight load permits, and bridge closures (Bridge Design Manual, 2004). The accuracy and magnitude of the rating factor is related to the selected rating methodology and the available information about the past performance of the bridge and its current condition. Section 905.5.1 of the Bridge Design Manual (2004) specifies that in order to rate a bridge correctly, the analytical model has to represent as much as possible the current condition of the bridge. This can be accomplished by using all available information such as design specifications, as-built drawings, material characteristics, and inspection reports.

There are three different bridge rating methodologies available, the Working (Allowable) Stress Rating (WSR) method, the Load Factor Rating (LFR) method, and Load and Resistance Factor Rating (LRFR) method. Currently, ODOT requires all bridges to be rated using the LFR method. However, after Oct. 1, 2010, all bridges designed by LRFD shall be rated according to LRFR. WSR is not used by ODOT and is not discussed any further.

The load rating system is divided into different levels of safety under which a bridge can be evaluated. LFR is based on a two level system, whereas LRFR employs a three level system. Each methodology is explained more detailed below.

### 2.4.1 LFR Rating Method

The LFR method considers the ultimate capacity of the structure and applies factors to the dead and live load. The load factors applied in this procedure are not based on reliability but on pure engineering judgment and past experience. Furthermore, no guidance is prescribed for adjusting the load factors due to possible uncertainties (Lichtenstein 2001). The two rating levels associated with the LFR method are the Inventory level and Operating level.

The rating factor for Inventory level is for the live load that can be safely supported by the bridge for an indefinite level of time (The Manual for Bridge Evaluation, 2008). The result from this evaluation is reported to the National Bridge Inventory (NBI). The load factor for the Operating level is defined as the maximum permissible live load that can be supported by the bridge. The rating factor for the Operating factor determines whether the bridge is sufficient to continue in its present state or if it has to be posted, strengthened, or closed (Bridge Design Manual, 2004). The basic rating equation employed by the LFR method is shown in Eqn. (1).

$$RF = \frac{C - A_1(DL)}{A_2LL(1+I)} \quad \text{Eqn. (1)}$$

where,

RF	=	LFR rating factor expressed as a percentage of the corresponding live load rounded to the nearest 5%.
C	=	capacity of the member at the critical location
DL	=	dead load effect
LL	=	live load effect (with distribution factor applied)
A <sub>1</sub>	=	dead load factor, 1.3 for Inventory and Operating level

- $A_2$  = live load factor, 2.17 for Inventory level and 1.3 for Operating level
- $I$  = impact factor =  $\frac{50}{L+125} \leq 0.30$
- $L$  = simple span length, ft

Each rating level has to be evaluated based upon the following truck models:

Inventory level

- HS 20 (truck or lane), GVW = 36 tons

Operating level

- HS 20 (truck or lane), GVW = 36 tons
- 2F1 (2 axle), GVW = 15 tons
- 3F1 (3 axle), GVW = 23 tons
- 4F1 (4 axle), GVW = 27 tons
- 5C1 (5 axle), GVW = 40 tons

(Note: 1 ton = 8.9 kN)

Figure 41 provides the dimensions and axle weights of each truck.

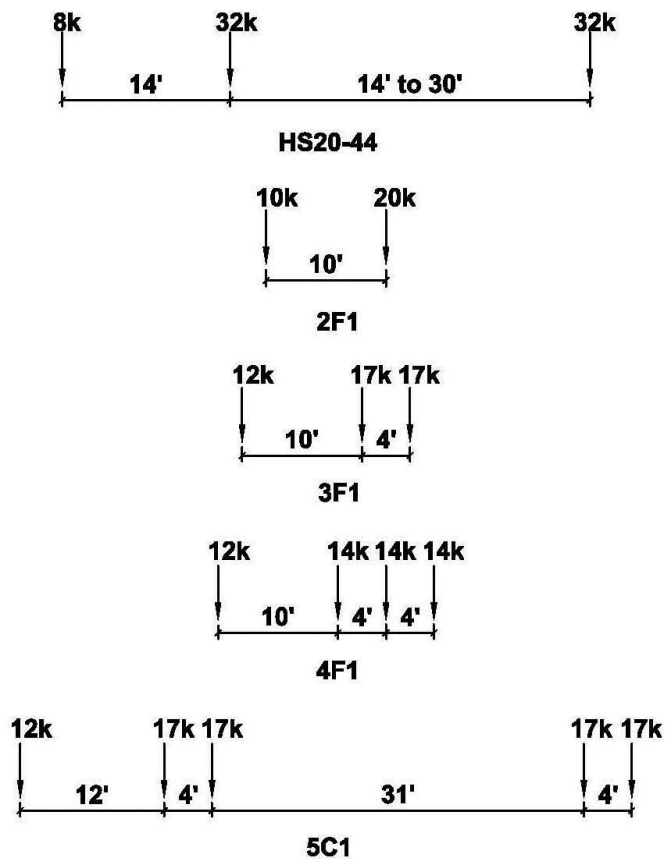


**Figure 41: Truck Configurations**

(Note: 1 kip = 4.45 kN)

The distribution of the live load to each girder can be computed according to the Standard Specifications for Highway Bridges (2002). For adjacent box beams the following equations apply:

$$g = \frac{S}{D} \leq 1 \quad \text{Eqn. (2)}$$

where

$g$  = distribution factor

$S$  = width of precast member, ft

$D$  is defined by Eqn. (3)

$$D = (5.75 - 0.5N_L) + 0.7N_L(1 - 0.2C)^2 \quad \text{Eqn. (3)}$$

where

$N_L$  = number of traffic lanes

$C$  is defined by Eqn. (4)

$$C = K \left( \frac{W}{L} \right) \text{ for } \frac{W}{L} < 1 \quad \text{Eqn. (4)}$$

$$C = K \text{ for } W/L \geq 1$$

where

$W$  = overall (edge to edge) width of bridge measured perpendicular to the longitudinal beams, ft

$L$  = span length measured parallel to longitudinal beams, ft

$K$  is defined by Eqn. (5)

$$K = [(1 + \mu) I/J]^{0.5} \quad \text{Eqn. (5)}$$

where

$I$  = moment of inertia

$J$  = St. Venant torsional constant

$\mu$  = Poisson's ratio for beams

This method allows the authorities to arrive at important decisions depending on the value of the rating factor. According to Ohio Manual for Bridge Inspection (2010), the maximum range for which the bridge does not need to be posted is above 92.5% of the Ohio Legal Load. Below this limit, posting shall be placed at the beginning of the bridge indicating the permitted load. If the rating factor is less than or equal to 15% of the Ohio Legal Load, then the bridge must be considered for closing until the required repairs or replacement are completed according to the Ohio Bridge Design Manual. Section 6A.8.1 of The AASHTO Manual for Bridge Evaluation also requires a bridge not capable of carrying a minimum gross live load weight of 3 tons (27 kN), must be closed.

## 2.4.2 LRFR Rating Method

The Load and Resistance Factor Rating (LRFR) method was developed as a procedure compatible to the reliability limit states philosophy of the LRFD bridge design code (Lichtenstein, 2001). The LRFR methodology provides a more rational, flexible and powerful evaluation strategy for existing bridges. A reliability rating approach can provide a uniform target level of safety through the use of improved resistance data, site-specific traffic data, accurate load distribution analysis, and by reducing uncertainties that are unavailable at a design point (Minervino, et. al., 2004).

The three rating levels that are part of the LRFR methodology are the Design, Legal, and Permit load rating levels. The Design load rating is the first-level and is based upon the HL-93 load. It represents the physical condition of the bridge and it relates the performance of the existing bridge to the LRFD bridge design standard. Under this level, the bridge is rated at the inventory and operating levels for the strength limit state. The second level, the Legal load rating, provides a single safe load capacity applicable to AASHTO and State legal loads. Posting and strengthening decisions can be made based upon the results of the legal load rating at the strength limit state. No evaluation is required for this level if the inventory rating factor at the strength limit state is larger than 1.0 (Lichtenstein 2001). Serviceability can also be checked and is selectively applied. The live load factors are decided based upon traffic conditions. These factors are summarized in Table 3.

**Table 3: Live Load Factors for Legal Loads**

Traffic volume	Limit State	Load factor
Unknown	Strength	1.8
ADTT > 5000	Strength	1.8
ADTT = 1000	Strength	1.65
ADTT < 100	Strength	1.4

If the bridge is sufficiently rated for carrying legal loads, then special load permits can be issued for vehicles above the established weight limits. The third level, the Permit load rating, evaluates the safety and serviceability conditions under special loads. Calibrated load factors by permit type and traffic conditions at the site are applied when evaluating the live load effects caused by the overweight truck (Lichtenstein 2001).

The LRFR rating factor is determined by Eqn (6).

$$RF = \frac{C - \gamma_{DC}DC - \gamma_{DW}DW \pm \gamma_P P}{\gamma_{LL}LL(1+IM)} \quad \text{Eqn. (5)}$$

where,

RF = Rating factor

C = Capacity, defined as  $\phi_c \phi_s \phi R_n$  for the strength limit state and  $f_r$  for the service limit states

$R_n$  = nominal member resistance (as inspected)

$f_r$  = allowable stress specified in the LRFD Specifications

$\phi_c$  = condition factor

- $\phi_s$  = system factor
- $\phi$  = resistance factor
- $\gamma_{DC}$  = LRFD load factor for structural components and attachments
- DC = Dead load effect due to structural components and attachments
- $\gamma_{DW}$  = LRFD load factor wearing surface and utilities
- DW = Dead load effect due to wearing surface and utilities
- $\gamma_P$  = LRFD load factor for permanent loads
- P = Permanent loads other than dead loads
- $\gamma_{LL}$  = Live load factor
- LL = Live load effect
- IM = Dynamic load allowance equal to 33%

The LRFR method allows for the reduction in uncertainties through the application of factors that reflect the current condition of the bridge. Two additional factors, aside from the resistance factor ( $\phi$ ) are applied to the nominal resistance of a member. The first one, the condition factor ( $\phi_c$ ), takes into account new uncertainties about the resistance of the deteriorated elements and their future degradation until a new inspection takes place. This factor does not reflect the geometric changes due to deterioration, but the influence of these variations on the structural capacity. This factor varies from 0.85 for members in poor condition to 1.0 for members in good condition (Minervino et al. 2004). The other factor, the system factor ( $\phi_s$ ), represents the ability of a bridge to redistribute the load if one or more of its elements have a structural deficiency. This factor is applied to the nominal resistance of individual elements and represents the redundancy of the entire superstructure. A factor of 1.0 represents a redundant multigirder bridge whereas a factor of 0.85 is assigned to a non-redundant system such as two girder, welded girder, and truss girder bridge (Minervino et al. 2004).

The live load models employed by the LRFR method include the HL-93 design load, the Ohio legal loads, and permit loads which depend on each State Transportation Agency. However, ODOT does not specify any overweight load. Figure 42 shows the HL-93 live load model and how it should be applied. The Ohio legal loads were previously presented.

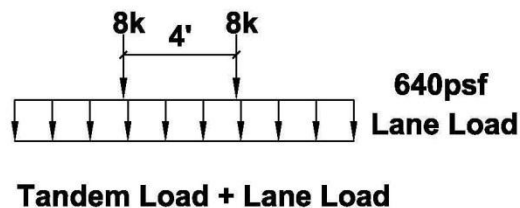
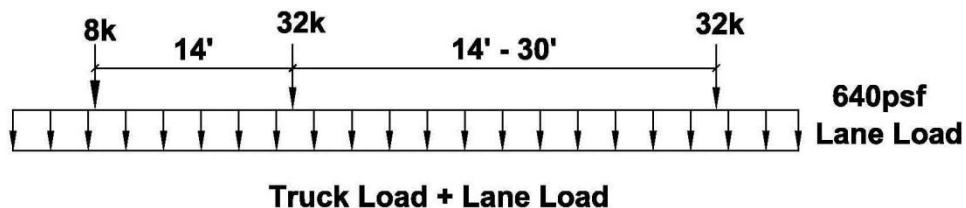


**Figure 42: HL-93 Design Live Load**

(Note: 1kip = 4.45 kN, 1 psf = 48 Pa)

The live load distribution factors are calculated according to the AASHTO LRFD Bridge Design Specifications (2010). For adjacent box beams, the moment live load distribution factors for interior and exterior girders are calculated as shown in the following equations.

Interior beam:

One design lane loaded:

$$g_{\text{int}} = k \left( \frac{b}{33.3L} \right)^{0.5} \left( \frac{I}{J} \right)^{0.25} \quad \text{Eqn. (6)}$$

$$k = 2.5(N_b)^{-0.2} \geq 1.5 \quad \text{Eqn. (7)}$$

Two or more design lanes loaded:

$$g_{\text{int}} = k \left( \frac{b}{305} \right)^{0.6} \left( \frac{b}{12.0L} \right)^{0.2} \left( \frac{I}{J} \right)^{0.06} \quad \text{Eqn. (8)}$$

where,

- b = width of beam (in)
- L = span of beam (ft)
- $N_b$  = number of beams
- I = moment of inertia ( $\text{in}^4$ )
- J = Torsional constant ( $\text{in}^4$ )

Exterior beam:

One design lane loaded:

$$g = (e)(g_{\text{int}}) \quad \text{Eqn. (9)}$$

$$e = 1.125 + \frac{d_e}{30} \geq 1 \quad \text{Eqn. (10)}$$

Two or more design lanes loaded:

$$e = 1.04 + \frac{d_e}{25} \geq 1 \quad \text{Eqn. (11)}$$

where,

$d_e$  = distance from the edge of the traffic railing to the exterior web of the exterior beam. This term is positive when the railing is outward and negative when the railing is inboard.

A correction factor (CF) due to the skew ( $\theta$ ) of a bridge has to be applied to all distribution factors and can be determined by Eqn. (11).

$$CF = 1.05 - 0.25 \tan(\theta) \leq 1 \quad \text{Eqn. (11)}$$

When the legal load rating at the strength limit state is not satisfactory, the posting process is initiated. LRFR provides a methodology for determining the posting load. However, each Transportation Agency can apply their own posting policy. The Manual of Bridge Evaluation (2008) recommends limiting the legal load according to Eqn. (12), if the RF lies between 0.3 and 1.0. If the RF is below 0.3, the code recommends forbidding the passage of a particular vehicle or to close the bridge if it is unsafe under all legal loads.

$$\text{Safe Posting Load} = \frac{W}{0.7} (\text{RF} - 0.3) \leq 1 \quad \text{Eqn. (12)}$$

where,

W = Weight of rating vehicle

RF = Legal load rating factor

For this research the Load factors shown in Table 4 were used. Only Strength I Load case was considered in order to compare with field results.

**Table 4: Strength I Load Factors**

$\gamma_{DC}$	$\gamma_{DW}$	Design Load		Legal Load $\gamma_{LL}$
		Inventory $\gamma_{LL}$	Operating $\gamma_{LL}$	
1.25	1.50	1.75	1.35	1.51

## 3. RESULTS

### 3.1 Nondestructive Testing

The results of the nondestructive testing are provided below. Each of the methods utilized provided insight into the bridge on specific items prior to destructive testing.

#### 3.1.1 Ground Penetrating Radar Results

The results of the GPR on the top surface of the bridge are shown in Figure 43. The areas of red in Figure 43 are areas of possible concrete distress. However, this may be slightly misleading. The first issue involves the shear reinforcement being at a different height near the center of the beam (see Figure 3). If the GPR unit scanned right above that location it would show up as poor concrete. The guardrails made access difficult near the edges of the bridge. This was the distress in the concrete was actually visible. The piers also show up differently since the shear reinforcement of the beams no longer exists at these closure pour locations. Based on these issues and the GPR plot in Figure 43, the overall condition of the top surface of the bridge was relatively good.

Figure 44 shows the GRP data from scanning the underside of the west span. The figure is shown as if viewed upward from below the bridge. The origin of the plot is the southwest corner (Beam 1 near the abutment). Red areas in Figure 44 are locations of concern. However, one major difficulty with scanning below the bridge is related to the gaps between the beams. The surfaces between the beams are often at slightly different elevations causing difficulty in performing a smooth transition from one beam to the next. These gaps appear as the long streaks in the GPR data. In addition, the width of the bridge in Figure 44 is less than the actual bridge width. This is caused by having to lift the scanning cart slightly for the gaps and unevenness between the beams. Water in the stream also did not allow access to reaching the full length of the span. However, the GPR method does point out an issue with the far right hand edge of the bridge in Figure 44. This is Beam 9, which did have significant damage and performed poorly in the destructive testing.

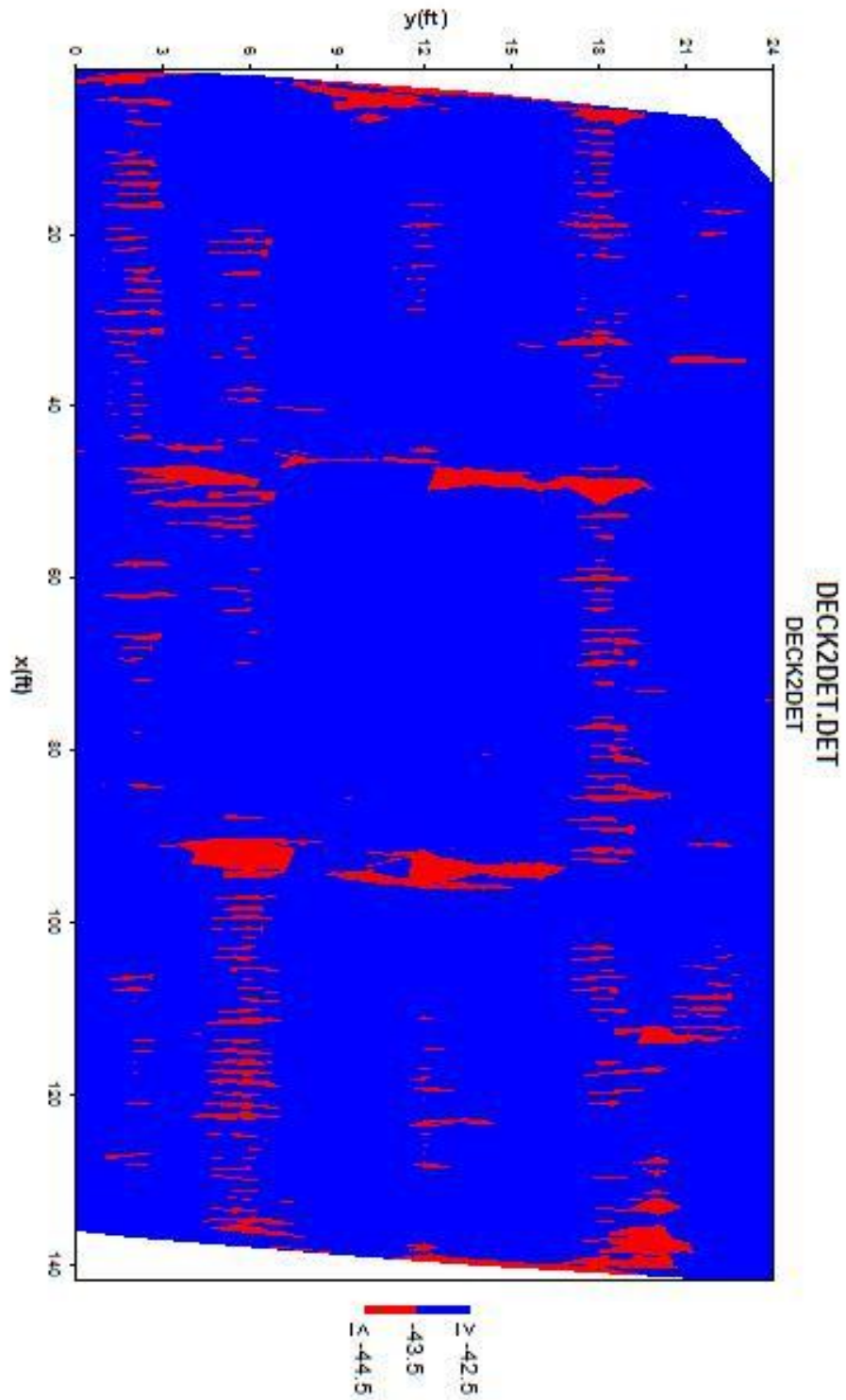
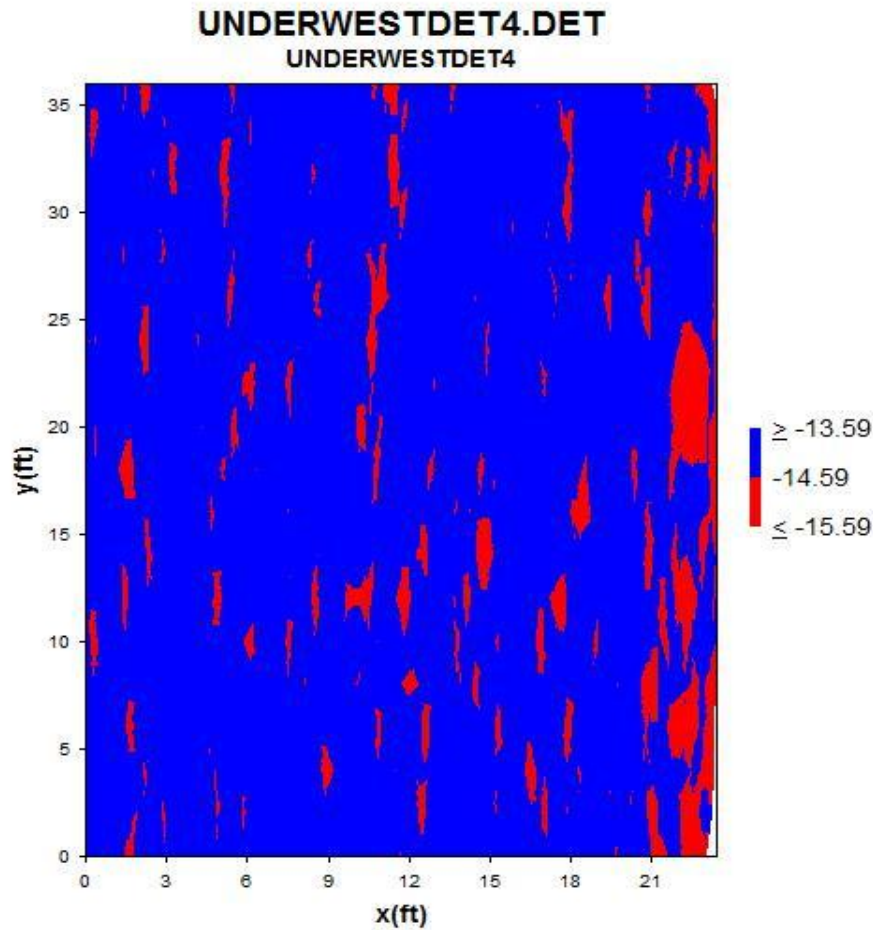


**Figure 43: GPR of Top Surface**



### 3.1.2 Magnetic Results

The University of Toledo performed magnetic nondestructive testing on a portion of the bottom of beams 2, 3, 4, and 9 of the East span on August 11<sup>th</sup> and 12<sup>th</sup>. The test area existed on interior Beams 2, 3, and 4 and exterior Beam 9. Areas were selected based upon visual inspection to encompass areas ranging from little to no corrosion up to heavily corroded areas.

Each Magnetic Flux Leakage (MFL) test for the interior beams was approximately 12.5 feet (3.8 m) long and started at approximately 189 inches (4.8 m) from the pier cap. For Beam 9, each MFL test was approximately 9 feet (2.7 m) long that started approximately 186 inches (4.7 m) from the abutment. Each MFL test is identified with data for a specific track which covers an area with a scan width of 8 inches (203 mm) and a scan length indicated for the beams. The transverse locations of all of the MFL tracks are shown in Figure 45. All MFL tests were performed by supporting the MFL equipment on a temporary wooden platform and moving the equipment on a set of wheels along the underside of the box girders. The start and end points for all tests were marked on the underside of the box girders.

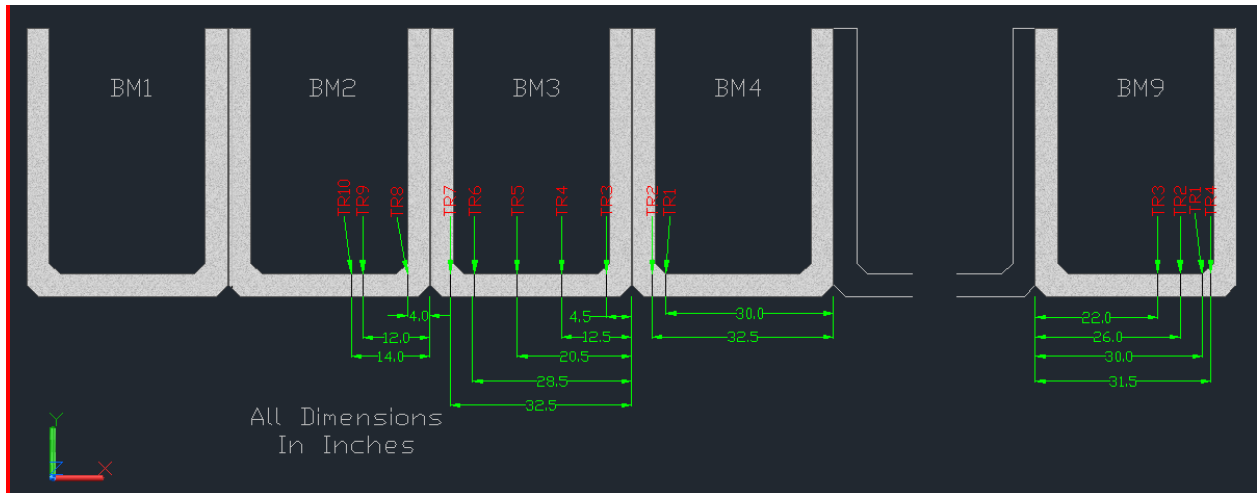
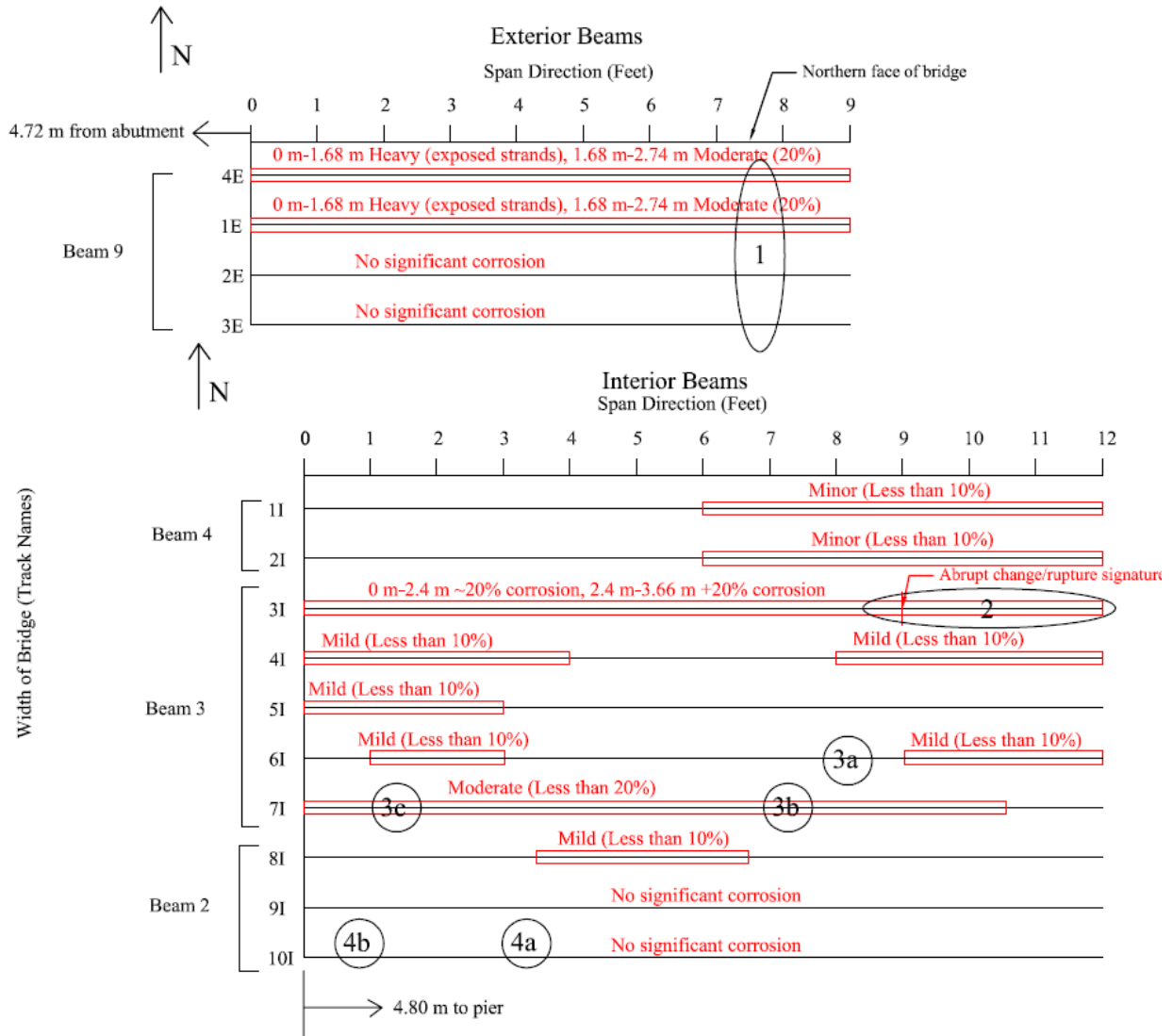


**Figure 45: MFL Test Tracks**

The Induced Magnetic Field (IMF) method was carried out following the MFL tests. Due to time restraints, it was decided to investigate two tracks, Track 3I and 7I. Track 3I had visible signs of corrosion and spalling toward the pier end, while Track 7I had no visible signs of corrosion but the MFL scan had indicated moderate corrosion. The MFL corrosion map in Figure 46 details the location of the test tracks. It also details the amount of corrosion found in each track according to the MFL scan. Finally, the circled numbers represent the locations of dissection following the MFL and IMF scans.

Figure 47 shows MFL results for sensor 4, which was located at the center of the scan width, for Tracks 1I, 3I, 7I and 10I. The graph is a plot of magnetic leakage field (in terms of Hall sensor output voltage) as detected along the length of the track scanned. The peaks in the graph indicate the presence of transverse stirrups along the beam. The peak-to-peak width of the signal indicates the stirrup spacing in the box-beam. Indications of irregular spacing of stirrups can also be seen for Track 10I in the figure within the first 3 ft. (0.9 m) of the test scan. The signal variations between peaks indicate the level of corrosion along the prestressing strand indicated in the figure. The evidence of strand fracture, or abrupt change, at the location of 9 ft. (2.7 m) can be seen for Track 3I as an abrupt interruption in the signal. It can also be noted that the decreasing nature of peak-to-peak signal amplitude indicates the increasing depth of steel inside the concrete.



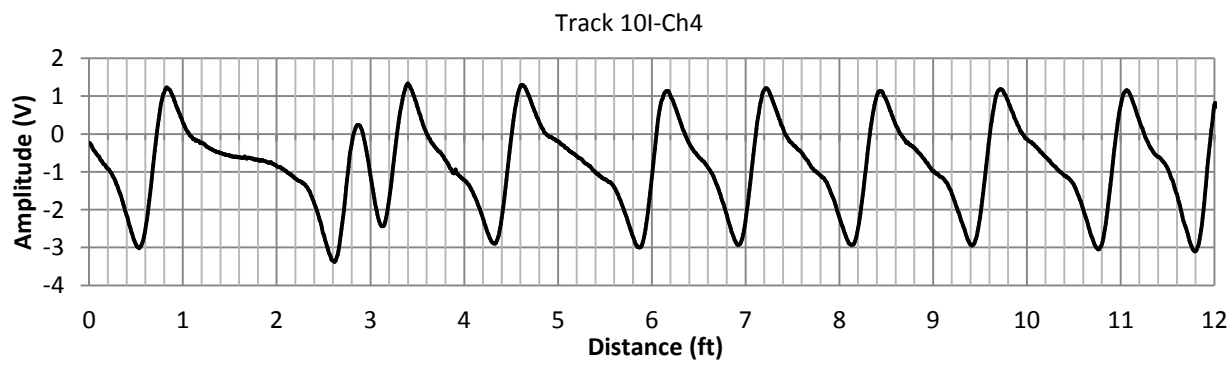
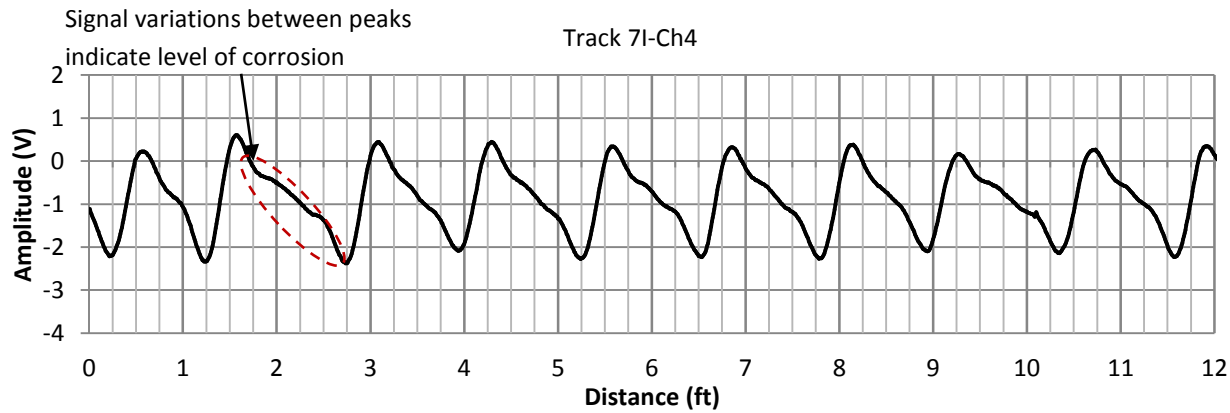
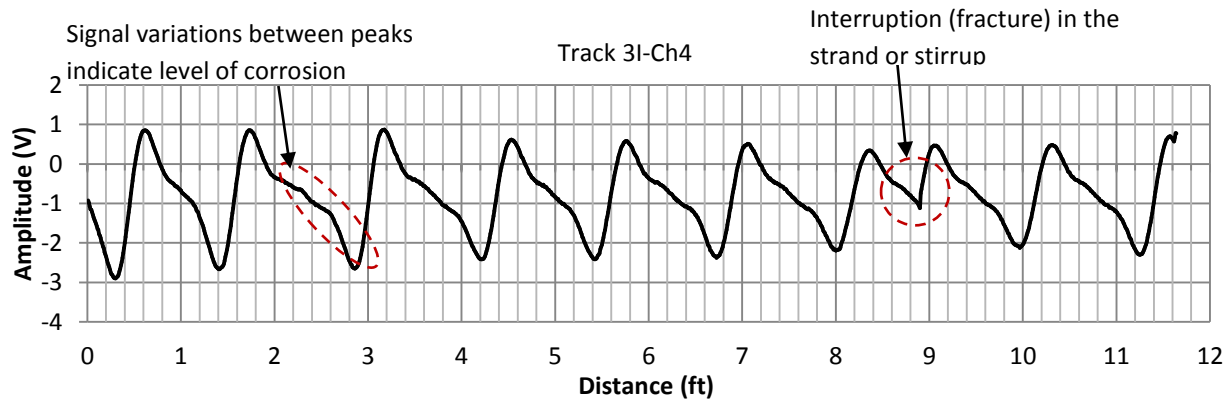
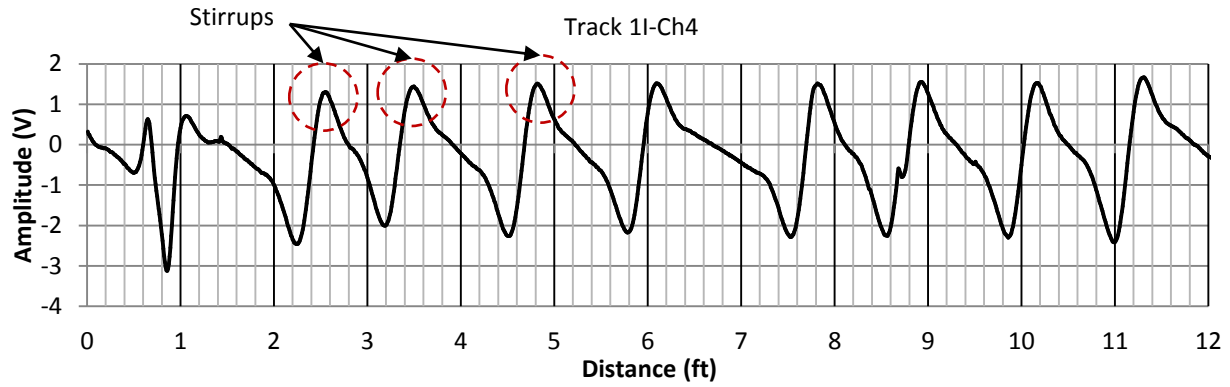
**Note:**

— = Corrosion Location (Corrosion Severity Details Above Track)

⊗ = Visual Dissection Locations

**Figure 46: Track Layout / MFL Corrosion Map**

(Note: 1' = 0.305 m)



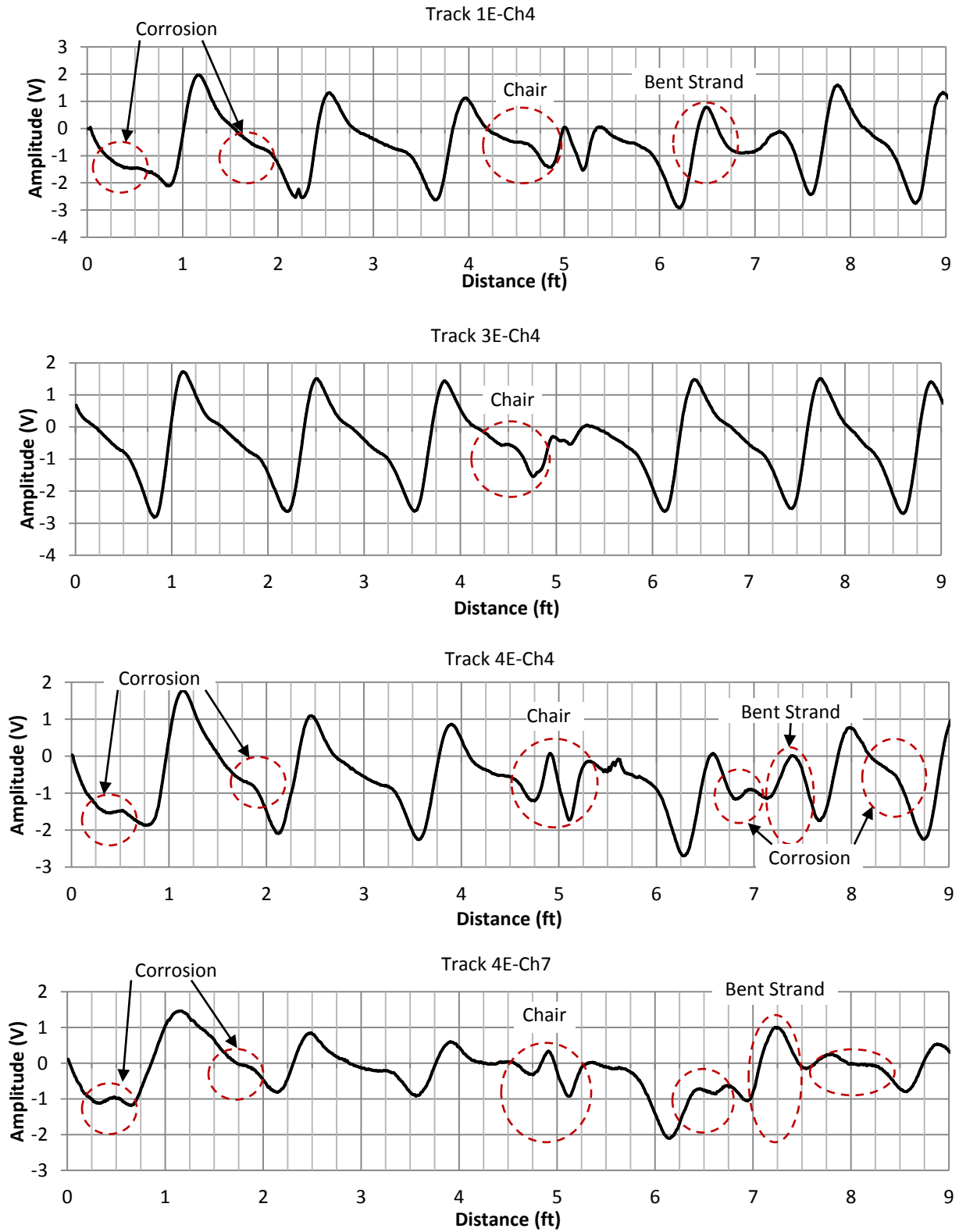
**Figure 47: MFL Scan Data Tracks 1I, 3I, 7I, and 10I**  
 (Note: 1' = 0.305 m)

Figure 48 shows MFL data for Tracks 1E and 3E from sensor 4, which is located at the center of the scan width. For Track 4, the data is displayed from sensors 4 and 7 where sensor 7 is located at the outside edge of the beam (north edge) of the scan width. Clear indications of the presence of steel chairs as well as exposed and bent strands are shown in the data from different tracks as marked in Figure 48. The bumps or bends in the signal between the peaks indicate the presence of chairs at that point inside the box beam. Points of corrosion are indicated by uneven signal amplitude between peaks of the signal. The bent strand refers to exposed strand on the exterior of the beam which is hanging down. The estimate of corrosion is made by zooming in on the magnetic field signal and making a correlation to the existing laboratory measurements. This method for determining the corrosion is qualitative and provides estimates of corrosion in ranges, (e.g. 10%-15%). While this estimate is not precise, it is sufficient to allow DOT officials to accurately assess the condition of the box beams in a bridge.

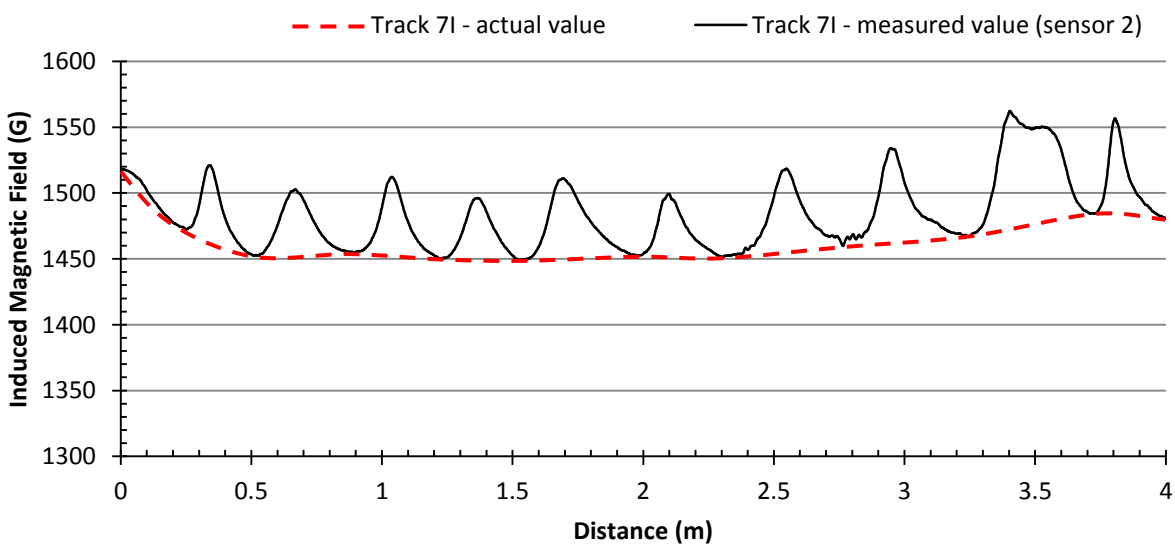
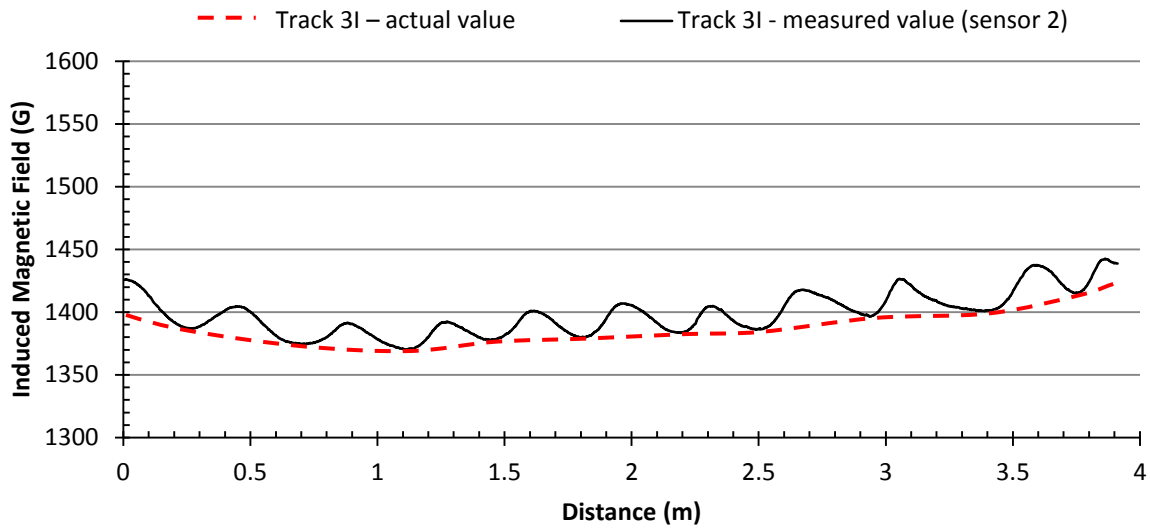
For the Induced Magnetic Field (IMF) procedure, tracks 3I and 7I were scanned along a length of approximately 12 ft. (3.7 m). For the bridge test, the strand closest to the bottom of the box beam is embedded 1.75 in. (44.5 mm) deep inside the beam. Accounting for the diameter of the strand, the edge of strand is approximately 1.5 in. (38.1 mm) from the concrete surface. During testing, a gap of roughly 0.5 in. (13 mm) – 0.75 in. (19 mm) was maintained between the pole face and the concrete surface being scanned in order to avoid damage to the sensors fixed on the pole face. Thus, the average gap between the pole and the strand was 2 in. (50.8 mm) - 2.25 in. (57.2 mm). However, the surface under the bridge is not completely flat. This curvature caused for a slight variation of distance between sensor and strand. This needs to be taken into consideration during estimation of strand cross-section from the measured data. The magnetic field induced in the strand is very sensitive to the distance between the strand and the sensor. It was assumed the strands inside the box beams were at a constant distance from the magnet pole face. However, the natural deflection of the beam and the unknown of the actual cover between strand and pole face could lead to inaccuracies in the test results. There were uncertainties in the estimate of the healthy cross-section area for the strand due to the uncertainty in the distance between the strand and the sensor on the electromagnet. Another uncertainty in the test data is stability of magnet strength. The electromagnet used in the test varies in strength as the magnet heats up with use. An estimation of the stable strength of the magnet was made to obtain these results. In the future, a thermocouple should be used to monitor temperature of the scans, which can be used to determine the stable strength of the magnet for specific test scans. Figure 49 shows the test results for IMF scan for Tracks 3I and 7I.

Figure 50 shows the magnetic field values for a laboratory test replicating the IMF scans for track 3I and track 7I. This laboratory test utilized prestressing strand magnetized using the same electromagnet used in the field test, held at a constant distance of 2.2 in. from the sensor. The graphs show the healthy value of gauss ( $B_{healthy}$ ) for tracks 3I and 7I as well as the baseline value with the electromagnet on and no steel present ( $B_0$ ). The values from Figure 50 were obtained using the same wooden beam that was performed in conjunction with this research (Titus, 2011). In order to determine the percentage corrosion for the scanned width, the values obtained from the field test ( $B_{corr}$ ) from Figure 49 are used in the following equation.

$$\text{Percentage loss} = \left( 1 - \frac{(B_{corr} - B_0)}{(B_{healthy} - B_0)} \right) \times 100$$



**Figure 48: MFL Scan Data Tracks 1E, 3E, and 4E**  
 (Note: 1' = 0.305 m)



**Figure 49: IMF Field Results for Interior Beam**

(Note: 1' = 0.305m)

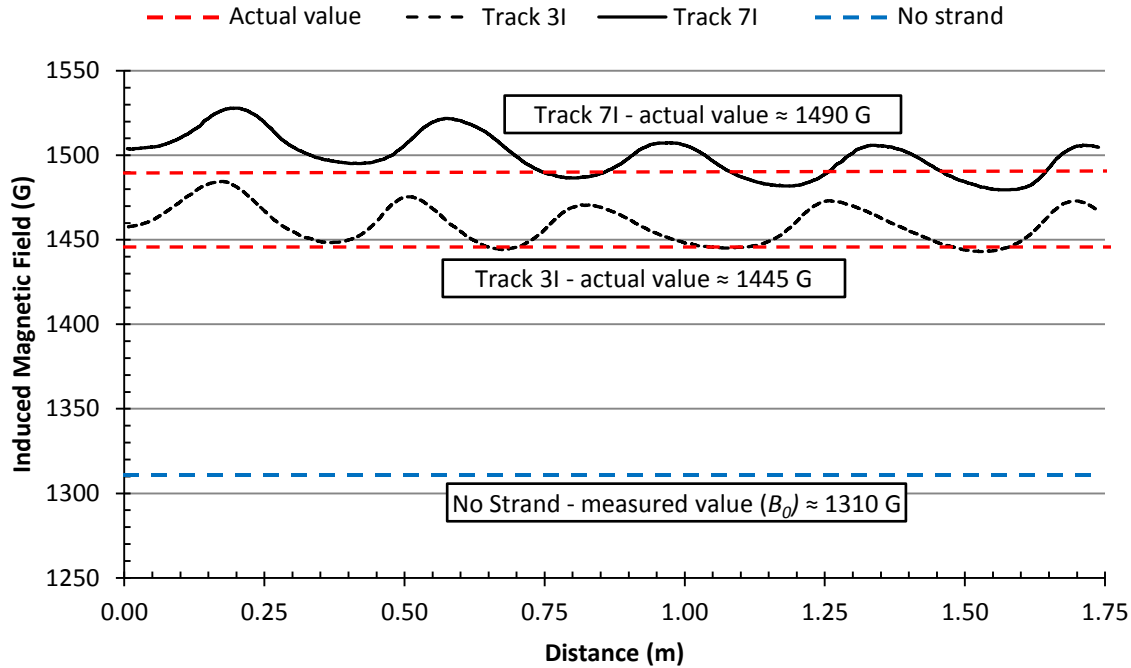


**Figure 50: Laboratory Results Tracks 3I and 7I w/ 2.2” between Pole Face/ Strand**  
 (Note: 1’ = 0.305 m)

Table 5 shows the percent corrosion for the scans at regular intervals for scan 3I and 7I. The results obtained are based on two assumptions; the stable strength of the magnet at the time of the test scan and the actual distance from strand to sensor. These variables can have a large effect on the results obtained from the IMF scans. As previously discussed, the stable strength of the magnet can be documented by installing a thermocouple of the electromagnet. For this test, laboratory experimentation was used to estimate the stable magnet strength at the time of the field tests. In order to accurately assess the distance from strand to sensor, a procedure must be developed. That said, the results from the test were not accurate over the entire length of the scan, but they did indicate corrosion. The results were accurate for the last few feet of the scan. The authors believe that over this range, the distance from sensor to strand was 2.2 in., and the strand was farther from the sensor for the rest of the scan (where higher corrosion was indicated than actually found). This premise cannot be verified though, since no measurements could be taken for distance from the sensor to the strand for the tracks. Overall, the IMF field test indicated corrosion, but more updated field tests are necessary to determine with confidence the accuracy of the test system. If the distance of the strand from the sensor can be measured too while scanning the tracks then the accuracy of the results would be improved.

After the field tests were completed, concrete was chipped away to expose the bottom layer of strands. Due to the difficulty of exposing strands, only specific areas of interest were selected based upon visual and magnetic inspection results (see Figure 46). The strands were then removed from the bridge and examined in the lab to determine their level of corrosion. This was necessary to determine the accuracy of the MFL and IMF testing. Observations are provided in Table 6.

**Table 5: IMF Corrosion Estimates for Tracks 3I and 7I**

Distance (ft)	Corrosion (%)	
	Track 3I	Track 7I
1	44	6
2	50	19
3	54	18
4	54	19
5	50	19
6	46	19
7	44	19
8	42	17
9	39	12
10	35	10
11	31	7
12	27	3

(Note: 1' = 0.305 m)

**Table 6: Comparison of Strand Loss to MFL and IMF Methods**

Track I.D.	MFL method (% corrosion)	IMF method (% corrosion)	Strand Condition
<b>Interior Beams</b>			
1I	<<10%	---	---
2I	<<10%	---	---
3I	~20%	27 – 54%	10%-30%
4I	<10%	---	5%
5I	<10%	---	---
6I	<10%	---	No significant corrosion
7I	<20%	3 - 19%	No significant corrosion
8I	<10%	---	---
9I	No significant corrosion	---	No significant corrosion
10I	No significant corrosion	---	No significant corrosion
<b>Exterior Beams</b>			
4E	~20%	---	20%
1E	~20%	---	15%-20%
2E	<10%	---	10%-15%
3E	No significant corrosion	---	5%

The results shown in Table 6 for MFL show an accurate correlation between the test results and actual condition of the strand. MFL indicated moderate corrosion (20%) in Track 7I, but upon concrete removal, very little corrosion was found in the strands. While the inaccuracy of a false positive is not desirable, bridge inspectors would be erring conservatively as opposed to the more dangerous situation of not finding corrosion in a damaged strand. The MFL testing predicted medium to heavy corrosion in Area 2 of Beam 3, which can be seen in Figure 51. The strands from 8 – 10 in. (203 – 254 mm) which were all/partially exposed show heavy corrosion. The previously embedded strands, from 4 – 7 in. (102 – 178 mm), show corrosion that gets

progressively lighter as the tape measure numbers decrease. The magnetic testing was accurate in this region, except that a full break in strands as depicted in the MFL scan was not found.



**Figure 51: Area 2 of Beam 3 Exposed**

The results from the IMF test indicated corrosion in the prestressing strand. However, when compared with the findings after concrete removal, the IMF method needs to be refined to improve its accuracy. In order to obtain a truly accurate reading, the distance between strands and sensor face must be known. In the future this issue must be addressed. Commercial methods have been identified as possible solutions, such as using a device to measure the depth of strand inside a concrete beam (e.g. Proceq Profometer 5+). A thermocouple can also be installed which can measure temperature which can be correlated to stable magnetic strength.

### **3.1.3 Truck Testing Results**

The results of the deflections across the width of the bridge along instrument lines A and B from static truck loadings are summarized in Figures 52 and 53, respectively. For almost all load cases, the deflection of the beams along instrument line A was larger than instrument line B. This is expected since line A is near midspan and line B is closer to the west pier. LC1 with the placement of a single truck (#8) resulted in small deflections but shows the larger deflections occurring near the position of the truck with lower deflections near the opposite side for both instrument lines. This shows good distribution of the load in both transverse and longitudinal directions. LC 2 and LC 3 was placement of the trucks in both driving lanes to produce maximum positive and negative moments, respectively. Both LC2 and LC3 show nearly constant deflection across the bridge except for the exterior beams which show slightly less deflection. This shows good transverse distribution of the loads. LC4 and LC5 were similar to truck placement of LC2 and LC3, respectively, except the trucks were positioned as far south as possible instead of in the lanes. This resulted in higher deflections in beams 1-4 and lower deflections in beams 6-9 and nearly the same deflection in Beam 5. LC7 and LC8 loading and positioning of loads were similar to LC4 and LC5, respectively. Recall, LC7 and LC8 were performed after cutting of the continuity steel over the west pier. The recorded deflections between LC4 and LC7 as well as LC5 and LC8 show minimal differences. This leads to the conclusion that just cutting the continuity steel over the pier was not sufficient to separate the

effect of the adjacent span. The bearing of the bottom of the beams against the closure pour concrete over the pier likely limited rotation of the beams and created continuity over the pier. LC6 was placement of all trucks in the center span after the continuity steel at the pier was cut. Upward deflection occurred at both instrument lines A and B and deflections were similar. This again reinforced that continuity still existed even though the steel had been cut.

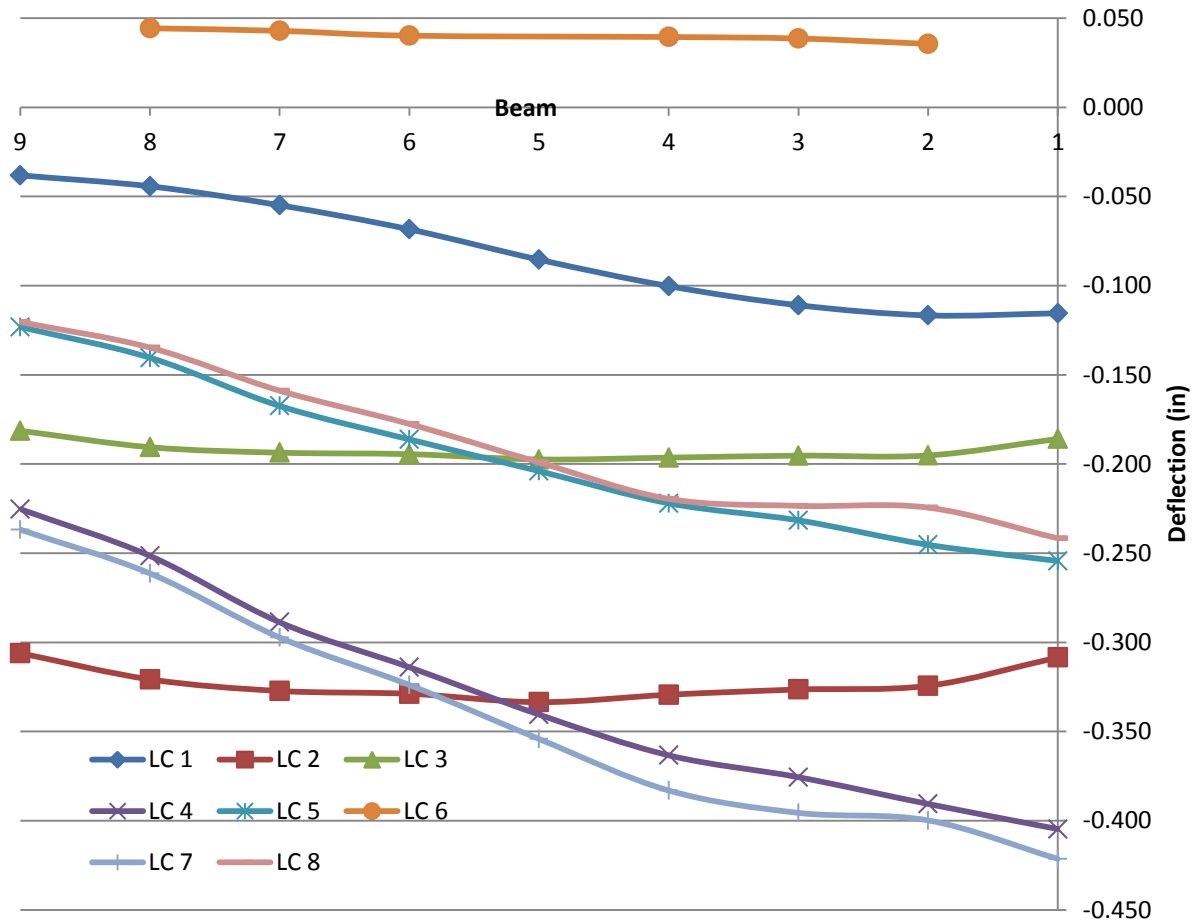


**Figure 52: Instrument Line A - Truck Tests**  
 (Note: 1" = 25.4 mm)

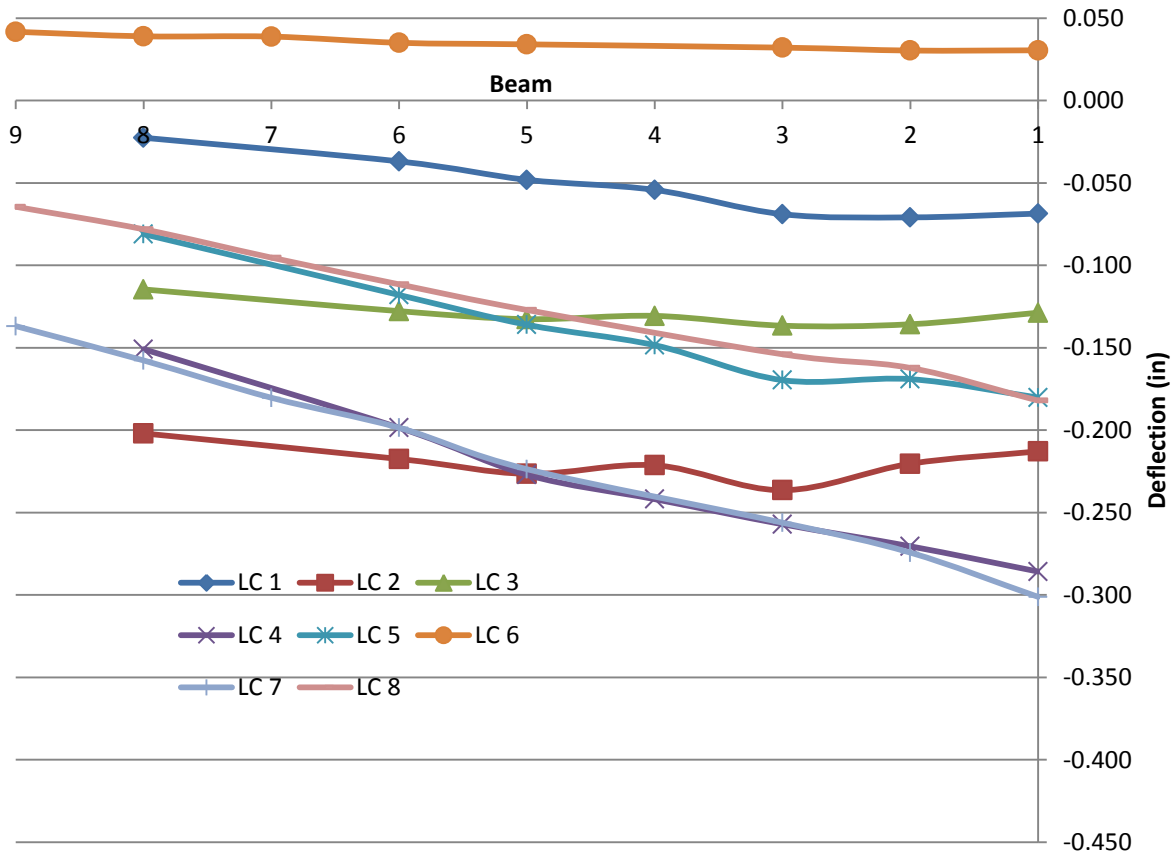


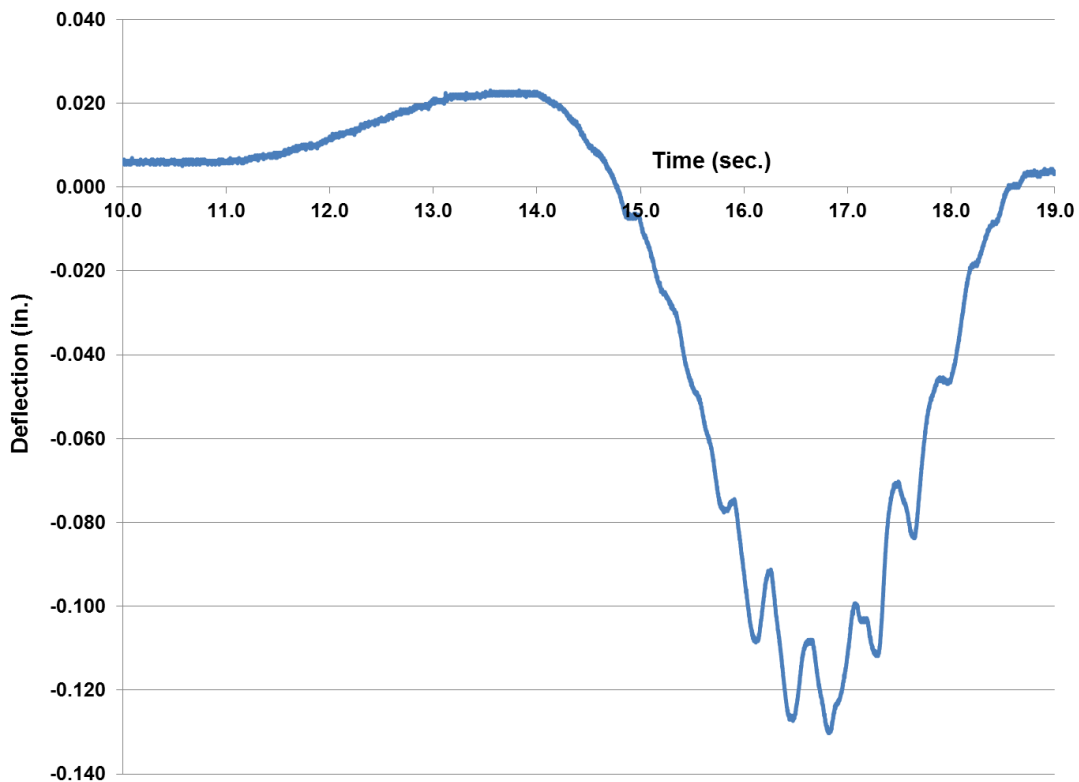
**Figure 53: Instrument Line B - Truck Tests**  
 (Note: 1" = 25.4 mm)

The dynamic effects on the bridge were investigated by calculating the dynamic load allowance for a single truck passing over the bridge. The dynamic load allowance (DLA) is a factor applied to the live load in order to account for vehicular dynamic effects, and by definition can be calculated in one of three ways. The DLA can be calculated by either dividing the maximum instantaneous dynamic response by the maximum static response, the dynamic response occurring at the location of the maximum static response by the maximum static response, or the maximum dynamic response by the static response occurring at the location of the maximum dynamic response. Even though the third method may be the most precise, the first method has been accepted as the definition in the AASHTO LRFD Specifications (Marsh, 1998).

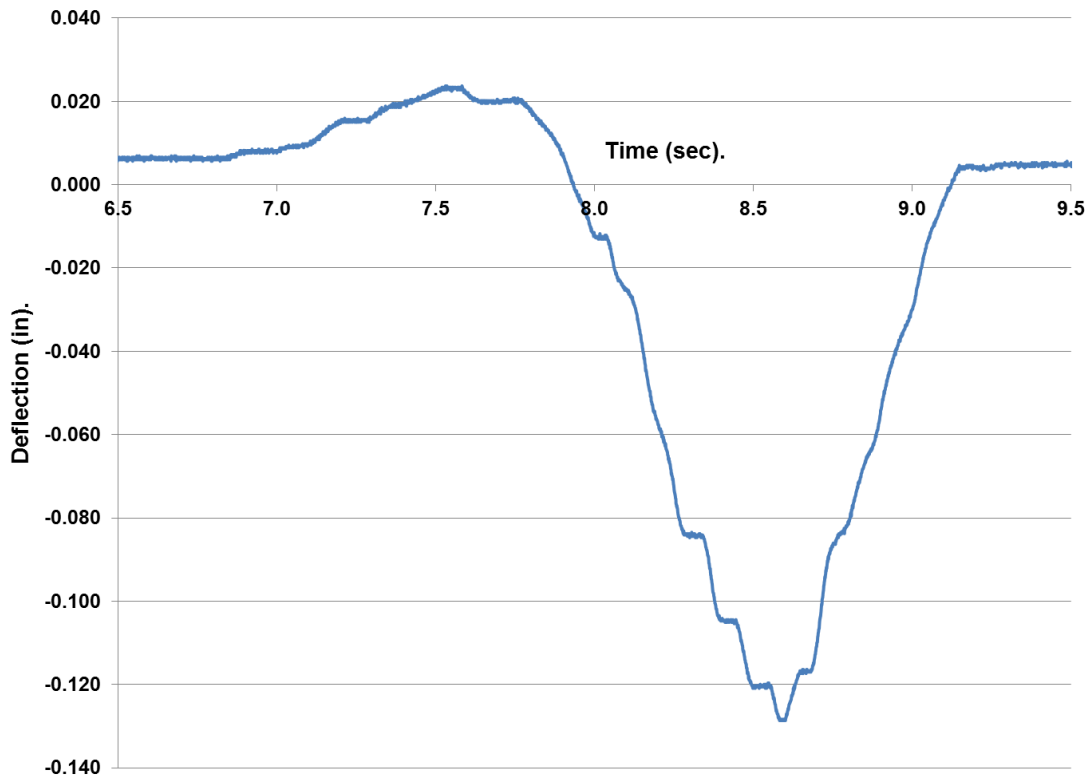
In this research project, string potentiometer locations limited the way in which the dynamic load allowance could be calculated. Since the maximum dynamic response of the bridge does not occur exactly at instrumentation line A, the actual maximum response was not measured. Instead, the maximum dynamic response at instrumentation line A was used with the static deflection at instrumentation line A (approximate location of maximum static). DLA calculations were completed by using the retrieved data and dividing the maximum dynamic response by the maximum static response from the truck load case 1 occurring at instrumentation line A. The accuracy of the DLA calculations may have also been affected by the static and dynamic truck locations. In the static case the bridge was loaded on the south side and in the

dynamic test the truck passed over in the north lane. The loading conditions created a transverse deflection profile that was opposite for each case. Assuming the bridge deflects similarly when loaded symmetrically in either lane, the maximum static and dynamic values were used to calculate the DLA.

Figures 54 and 55 show the instrument line A data for Beam 8 as the truck passes at 10 mph (16 kph) and 35 mph (56 kph), respectively. As both figures show, Beam 8 deflects upward as the truck is in the center span and prior to the truck entering the west span. This is again showing continuity of the bridge over the pier. As the truck enters the span, deflections increase downward until the truck begins leaving the span and bridge. The maximum deflections by the two truck speeds are approximately the same. The rapidly changing deflection, as the truck is within the span, is likely the vibration caused by the truck loading. This effect is more noticeable in the 10 mph (16 kph) speed than the 35 mph (56 kph) speed. Plots were created for all beams and were similar to Figures 54 and 55, but the magnitude of the deflections changed. The data from individual beams was then used to generate maximum deflections across the width of the bridge.

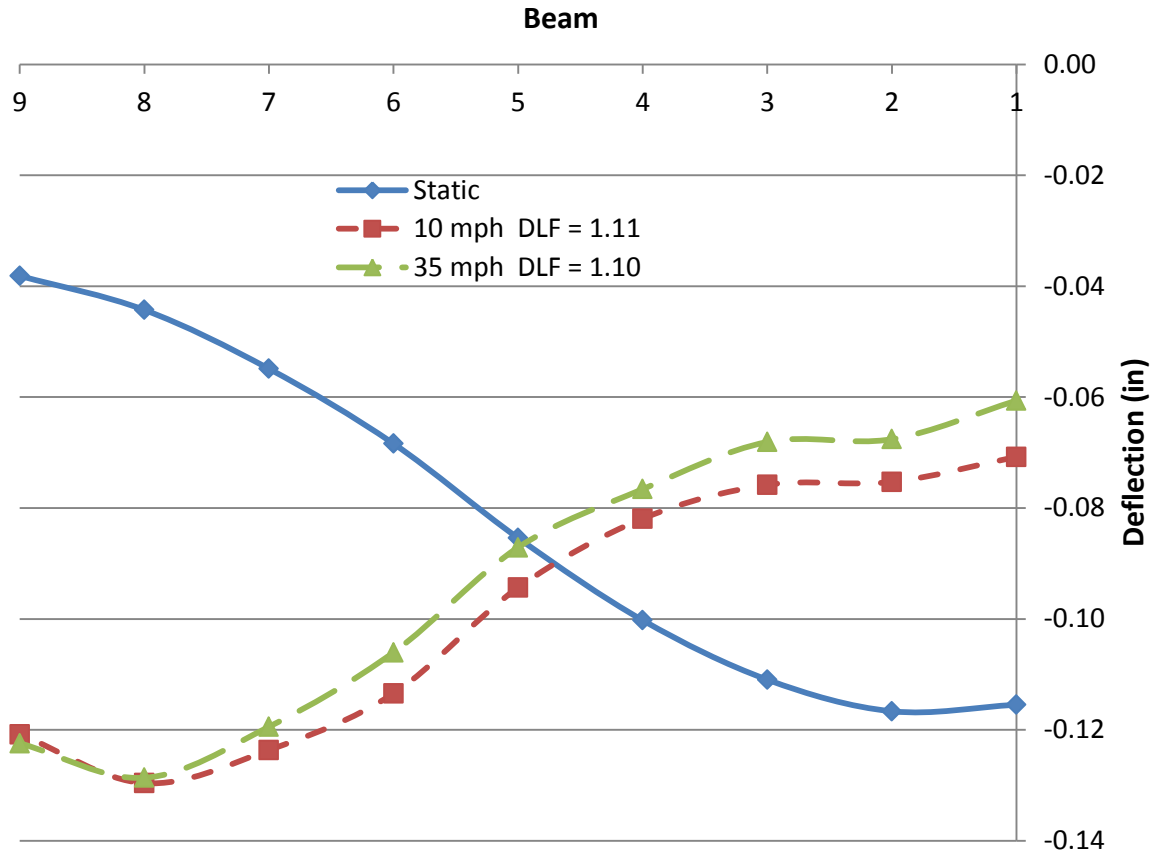


**Figure 54: 10 mph Moving Truck Deflection (Beam 8 – Instrument Line A)**  
(Note: 1mph = 1.61 kph, 1" = 25.4 mm)



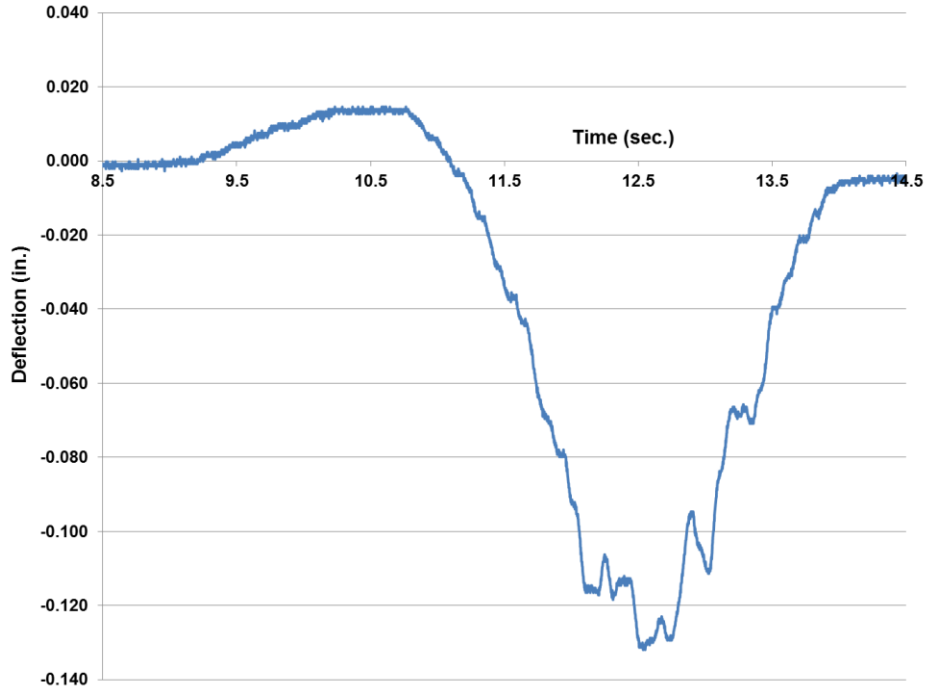
**Figure 55: 35 mph Moving Truck Deflection (Beam 8 – Instrument Line A)**  
 (Note: 1mph = 1.61 kph, 1" = 25.4 mm)

Figure 56 compares the maximum deflections at instrument line A across the width of the bridge from static LC1 and the moving truck at 10 mph (16 kph) and 35 mph (kph) prior to cutting of the continuity reinforcement over the pier. In both dynamic loading cases the truck traveled from east to west. Interestingly, the response to the truck moving at higher speed was slightly less except on Beam 9. However, this difference was less than 0.01" (0.25 mm) and DLF was basically the same at 1.10.

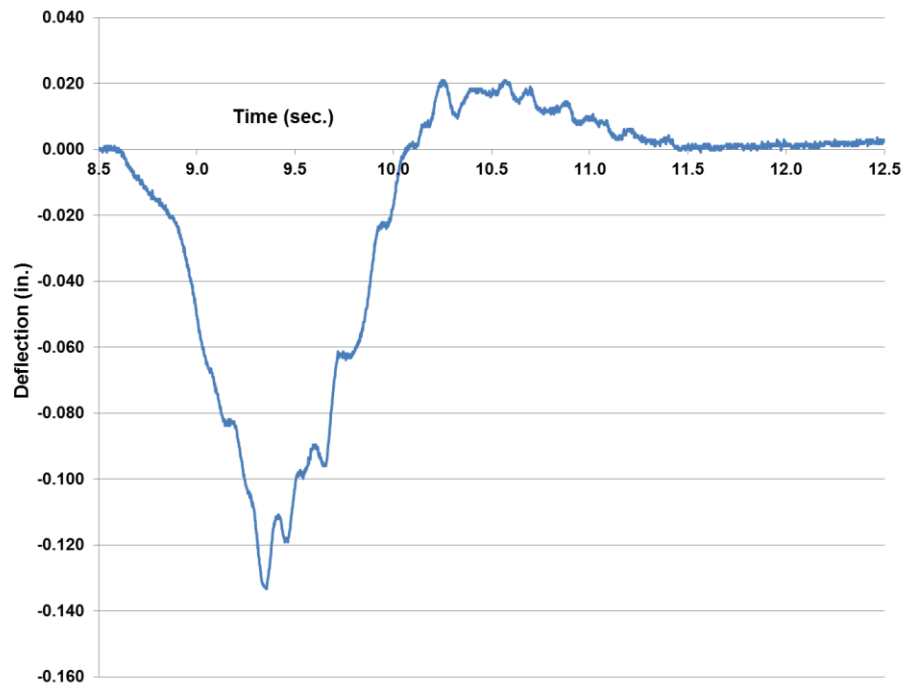


**Figure 56: Maximum Dynamic and Static Deflection (Truck # 8)**  
 (Note: 1" = 25.4 mm)

Figures 57 and 58 show the instrument line A data for Beam 8 as the truck passes at 10 mph (16 kph) and 35 mph (56 kph), respectively, after the cutting of the continuity reinforcement over the pier. As both figures show, the Beam 8 deflects upward as the truck is in the center span once again showing continuity between spans even though the reinforcement was cut. Figure 58 also shows that the truck was actually run in the opposite direction (from approach slab to west span) compared to the other truck tests (from center span to west span). However, the results were still very similar in magnitude. The results in Figures 57 and 58 show more vibration than in Figures 54 and 55, where the continuity reinforcement had not been cut. This is likely due to the bump that was created at the pier when the asphalt was removed to cut the continuity reinforcement and then patched.

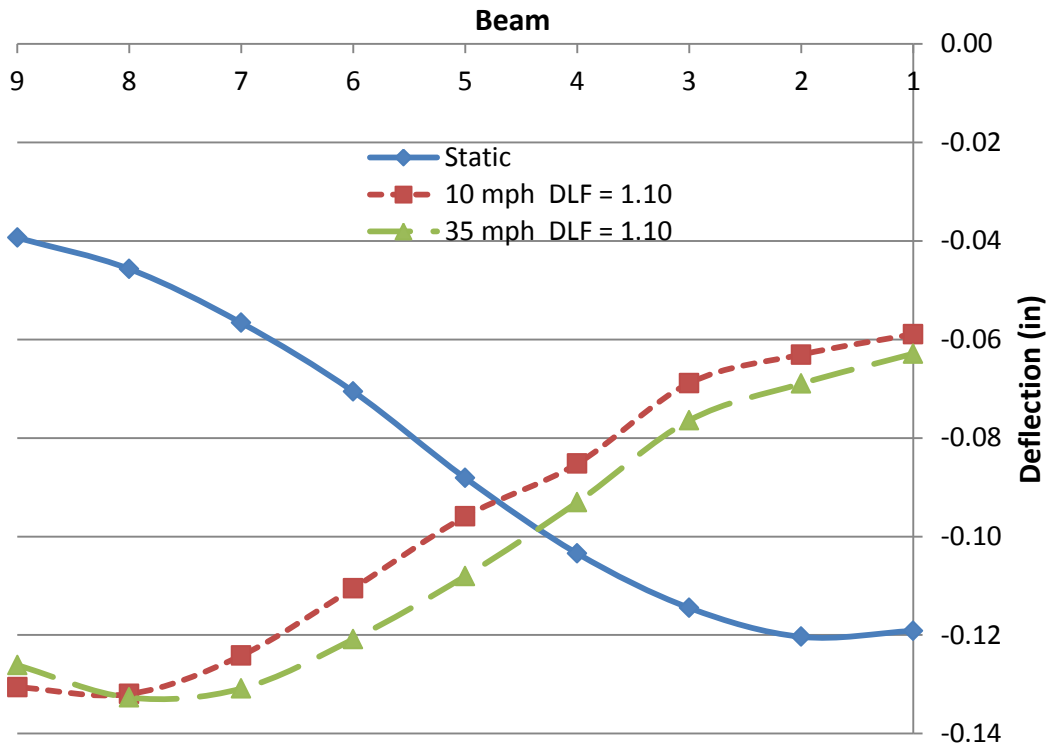


**Figure 57: 10 mph Moving Truck Deflection w/o Continuity Reinforcement  
(Beam 8 – Instrument Line A)**  
(Note: 1mph = 1.61 kph, 1” = 25.4 mm)



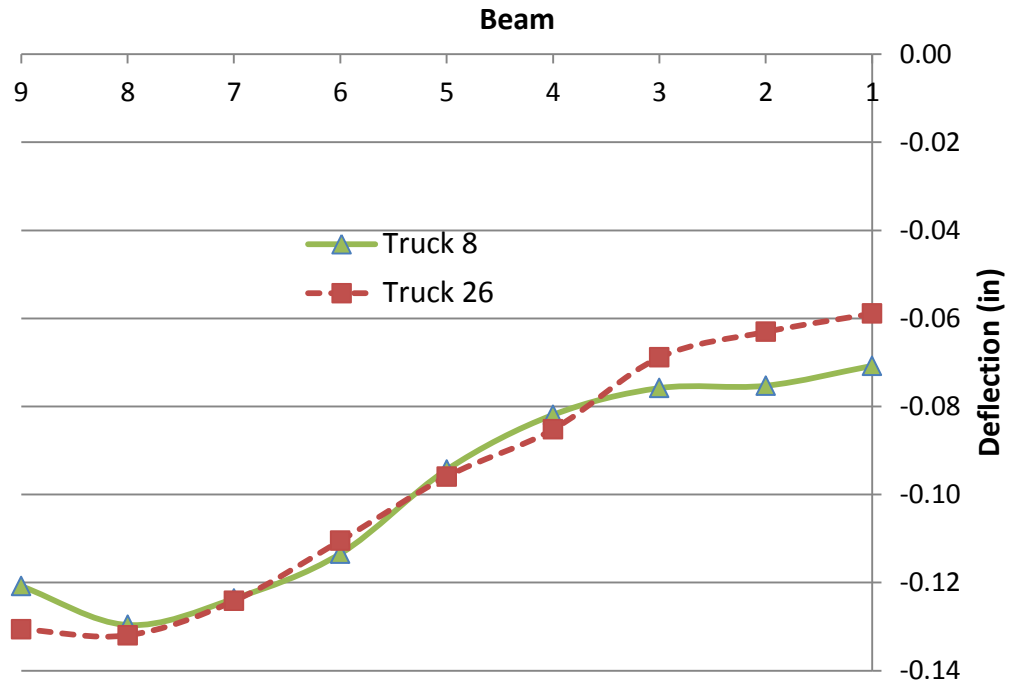
**Figure 58: 35 mph Moving Truck Deflection w/o Continuity Reinforcement  
(Beam 8 – Instrument Line A)**  
(Note: 1mph = 1.61 kph, 1” = 25.4 mm)

Figure 59 shows the results from static LC1 and the dynamic truck loading after the cutting of the continuity reinforcement over the pier. In this instance the higher truck speed resulted in slightly higher deflections, except at Beam 9. It should also be noted that in these particular tests, the truck moved east to west at 10 mph (16 kph) and west to east at 35 mph (56 kph). In addition, truck 26 was slightly heavier than truck 8 that was used for the static case. Therefore, the static deflections were magnified by the increased weight of truck 26. For both cases, the DLF was equal to 1.10 which was no change from prior to cutting the continuity reinforcement over the pier.



**Figure 59: Max. Dynamic vs. Static (Truck #26)**  
 (Note: 1mph = 1.61 kph, 1" = 25.4 mm)

Figures 60 and 61 compare the deflections from the moving truck loads prior to (truck 8) and after (truck 26) cutting the continuity reinforcement for 10 mph (16 kph) and 35 mph (56 kph), respectively. For the 10 mph (16 kph) condition, no significant differences occur. For the 35 mph (56 kph) case, slightly higher deflections were measured on the majority of the beams after the continuity reinforcement was cut (truck 26). However, it should be noted the truck was slightly heavier and traveled west to east, while truck 8 traveled east to west.



**Figure 60: Joint Effect (10 mph)**  
 (Note: 1mph = 1.61 kph, 1" = 25.4 mm)

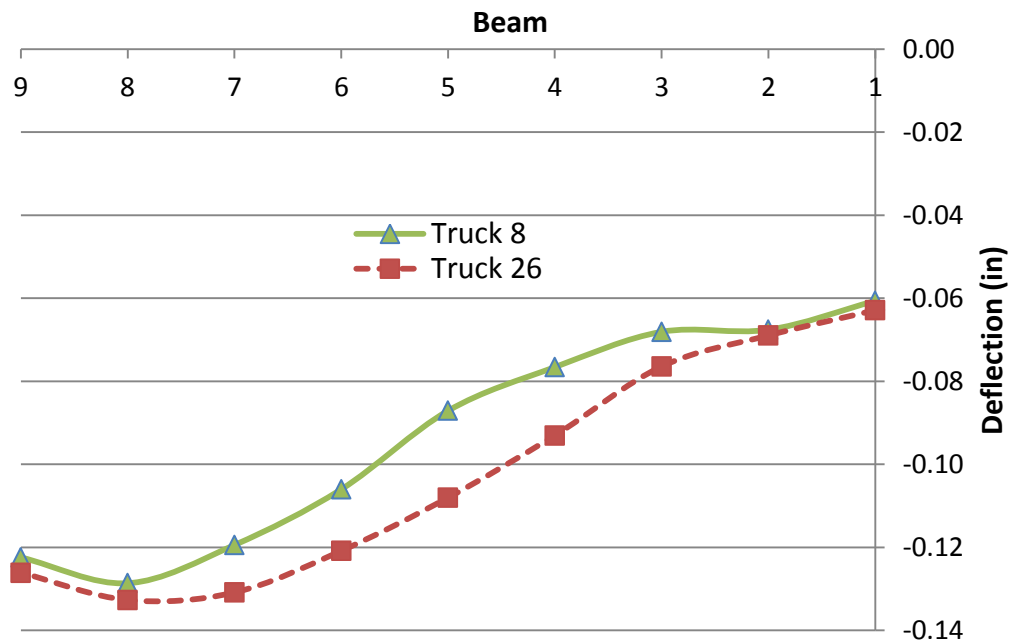


**Figure 61: Joint Effect (35 mph)**  
 (Note: 1mph = 1.61 kph, 1" = 25.4 mm)

### 3.2 Concrete Coring

Concrete cores were taken from the East span after destructive testing to assure the removal of cores did not affect the results of destructive testing. Cores were only removed from the East span since the Middle span was not accessible after destructive testing and the West span was not in a safe condition to remove cores due to collapse. The cores samples were taken approximately 17' (5.2 m) from east abutment end of East Span across the width of the bridge near the diaphragm in order to avoid the void in the beams while still attempting to avoid the transverse tie bar. The cores were taken through the depth of the beams. However, the cores could not be obtained at full length and therefore there was typically a top and bottom portion and often a middle section. The cores were numbered from the south toward the north.

The cores were tested for compressive strength in accordance with ASTM C 39/C 39M-03. Since many of the samples did not have length-diameter ratios (L/D) greater than 1.75, ASTM C 42/C 42M-03 correction factors for the samples were utilized. Interpolation, as allowed by ASTM, was used to determine correction factors for L/D between the values provided by ASTM. The results of the compressive testing on the cores are provided in Table 7.

**Table 7: Concrete Core Test Results**

Core	Diameter (in)	Height (in)	Adjusted $f'_c$ (psi)	Unit Weight (pcf)	E (ksi)	
					Eqn. 13	$\sigma$ - $\epsilon$ plot
C2T	4.008	8.29	9,479	149	5,822	5,463
C4B	4.001	8.58	10,499	148	6,063	4,876
C1T	3.995	9.67	8,513	146	5,385	4,012
C3T	3.990	10.01	10,204	145	5,831	3,769
C2B	4.005	6.77	9,555	146	5,699	4,156
C5T	4.002	6.44	10,140	148	6,012	4,064
C1B	3.985	6.50	11,733	148	6,436	4,763
C4T	4.006	5.51	11,132	145	6,103	-
Average			10,157	-	5,919	4,443

(Note: 1" = 25.4 mm, 1 psi = 6.89 kPa, 1 pcf = 158.9 N/m<sup>3</sup>, 1 ksi = 6.89 MPa)

The compressive strength of the cores ranged from 8,513 psi (58.7 MPa) to 11,733 psi (80.8 MPa) with an average of 10,157 psi (70.0 MPa). The compressive strengths exceeded the expected strengths. However given the age and condition of the concrete, this is not unreasonable. The Young's modulus of elasticity (E) for the concrete cores was determined by two different procedures. The first method involved using Eqn. 13 from the AASHTO Bridge Design Specifications

$$E = 33,000 w^{1.5} \sqrt{f'_c} \quad \text{Eqn. (13)}$$

where,

w = unit weight of the core (kcf)

$f'_c$  = compressive strength of the core (ksi)

The other procedure for determining E involved determining the slope of the stress-strain plot from the tests. As shown in Table 6, using Eqn. 13 to determine E always resulted in higher and more reasonable values based on the compressive strengths observed. The stress-strain curve method resulted in lower values than expected and was difficult to perform due to the nonlinearity of curves.

### 3.3 Chloride Testing

In order to perform testing for chlorides, concrete powder samples were removed from the bottom portion of the concrete cores by drilling into the cores and collecting material per AASHTO Standard T 260-97(05). The chloride testing was performed to determine the chloride ion content and its potential to accelerate corrosion. Given that corrosion due to chlorides can cause significant deterioration over time and have a major impact on the strength of the structure, the chloride levels were examined and compared to threshold levels determined from the literature. The bottom section of the core was chosen since chloride contents near the prestressing strand were of most interest. It was typically attempted to take two samples from each core for testing. However, several cores split or cracked while drilling to obtain the samples. For cores where two samples could be taken, the first sample was taken from near the surface to a depth of typically less than 1” (25.4 mm). The second sample was then taken to a depth of 1” (25.4 mm) or slightly more. This was mainly dependent on the height of the core and to assure the core was still sound for compression testing after proper preparation. The results of the chloride testing are shown in Table 8. As can be seen from the results, most of the samples showed a chloride content of approximately 0.04%. This chloride level exceeds the threshold level of 0.025% set in Phase I of this research. Though the chloride contents exceeded the threshold level, only minor to no corrosion of strands was observed.

**Table 8: Chloride Test Results**

Chloride Testing			
Core	Sample	Depth (in)	Chloride (%)
C1B	C1B-1	0-1.25	0.0420
	C1B-2	1.25-2	0.0408
C2B	C2B-1	0-0.75 (Split while drilling)	0.0349
C3B	C3B-1	0-0.25 (Cracked while drilling)	0.0390
	C3B-2	Split while drilling	0.0396
C4B	C4B-1	0-0.75	0.0325
	C4B-2	0.75-1.25	0.0325
C5B	C5B-1	0-1.5 (Split while drilling)	0.0231
C6B	C6B-1	0-0.625	0.0682
	C6B-2	0.625-1	0.0360

(Note: 1” = 25.4 mm)

### 3.4 Destructive Testing

#### 3.4.1 East Span

The deflection data recorded from the East span was very erratic due to what was believed to be excessive movement of the support frame for the string potentiometers. Efforts were made to remove this movement by utilizing the string potentiometers attached to the loading frame. Though some data for beams right below the loading frames could be developed by this procedure, beams away from the loading frames and their attached string potentiometers continued to show unusable deflection data. However, quality load and strain data still provided significant information on the behavior of the bridge. It should also be noted that the strain presented throughout this report is a relative strain because the absolute strain prior to the installation of strain gages is unknown.

Figures 62-64 show the strains in the bottom of the beams along instrument line H for the individual loading of cylinders 1-3 to 100 kips (445 kN). Positive strains are tensile. In Figure 62 where cylinder 1 was loaded to 100 kips (445 kN), the behavior of the bottom strains across the width of the bridge were generally expected. The strain was highest for Beam 8, which was at the location of the loading from cylinder 1. The strains increased in the beams as the load increased. It should also be noted that as the load increases from 69 kips (307 kN) to 100 kips (445 kN), the strain in Beams 3, 5, and 6 show almost no increase in strain while Beams 1, 2, and 4 increase. Beams 3 and 5 were the most damaged beams with 6 strands cut each and Beam 6 had 3 strands cut. Beam 2 also had 3 strands cut but Beams 4 and 1 did not have any damage induced. Therefore, it appears the undamaged beams start to acquire more load more than the damaged beams.

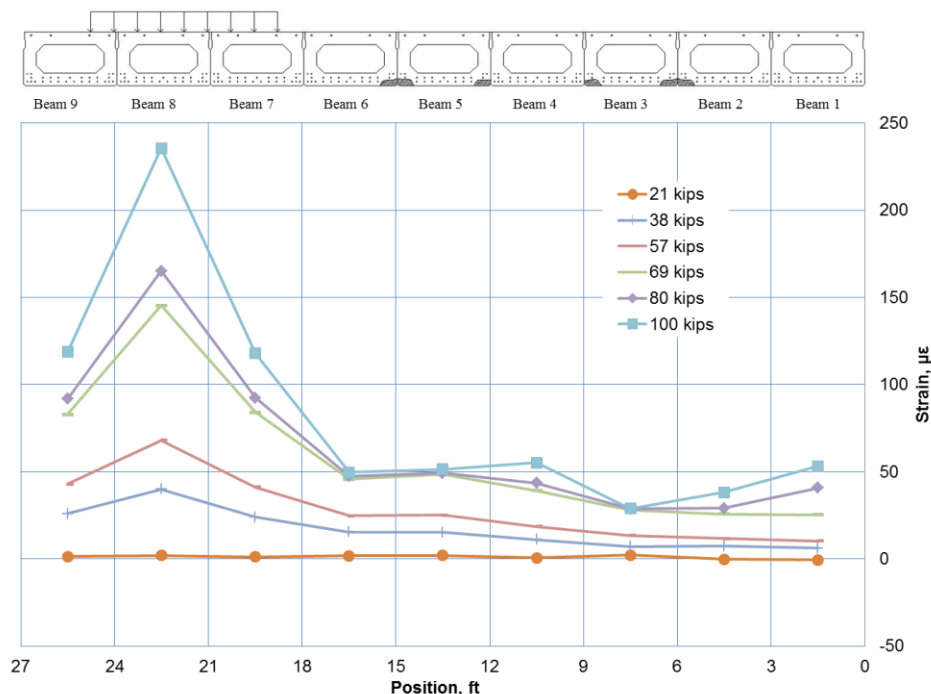
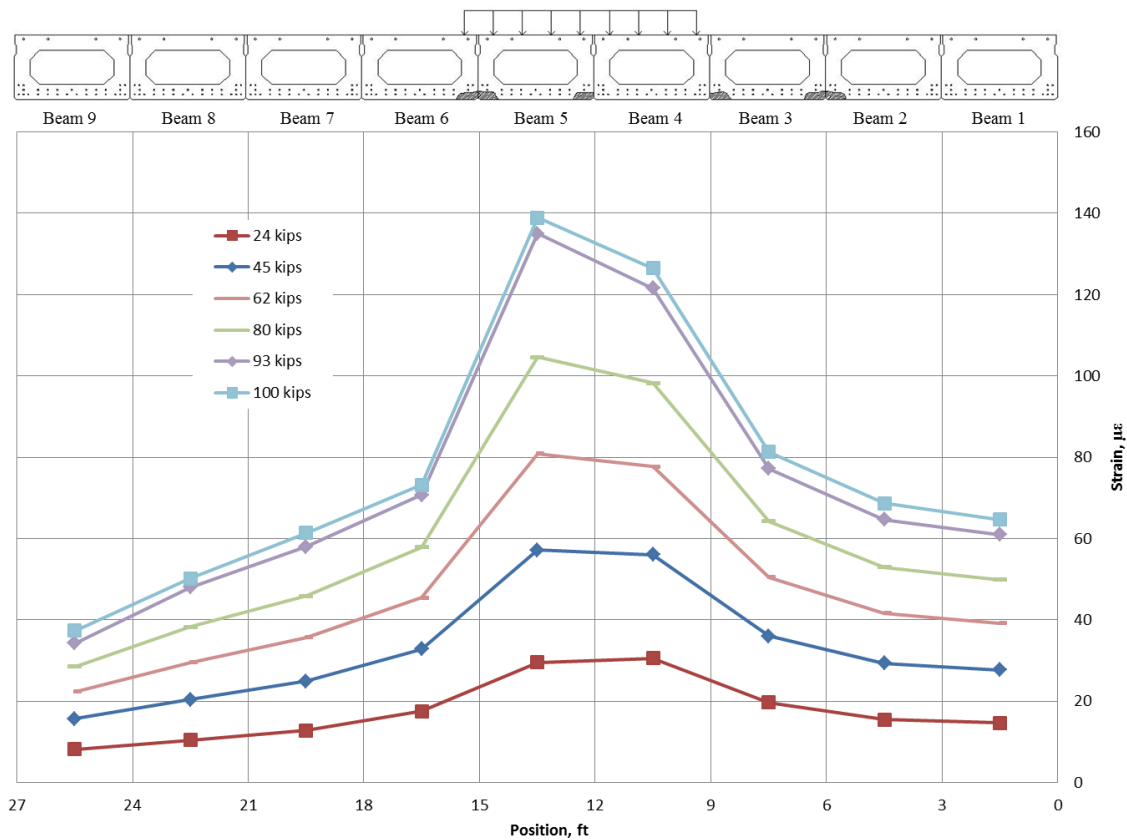


**Figure 62: Bottom Strain Profile Instrument Line H (Cylinder 1 – 100 K)**

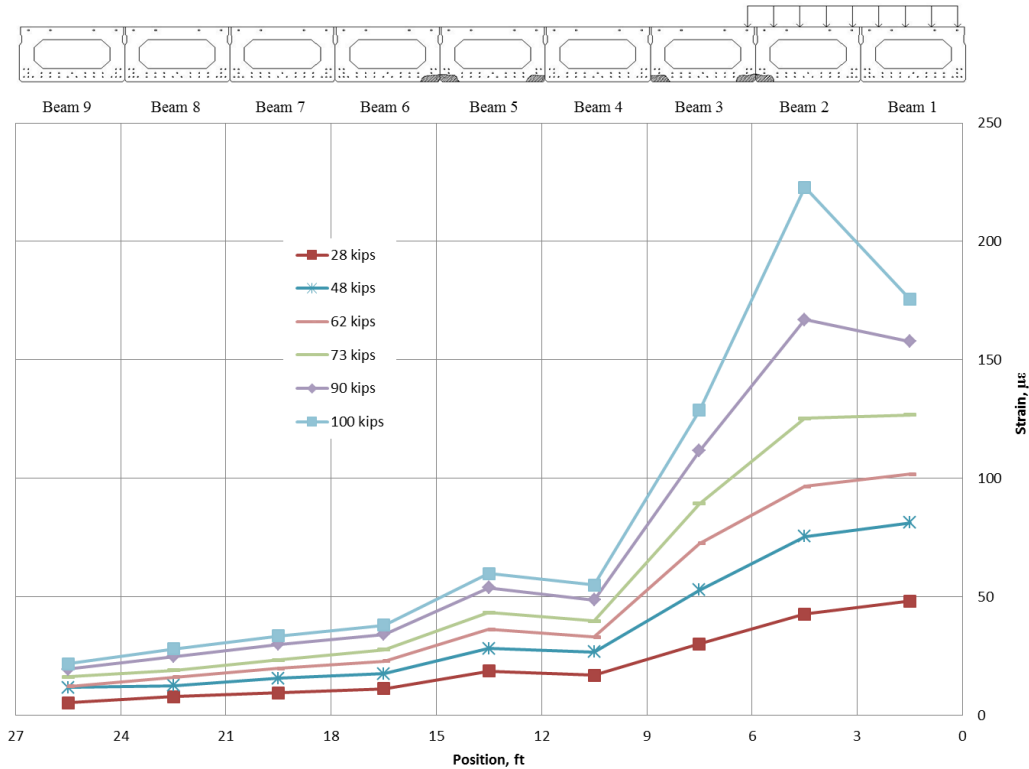
(Note: 1 kip = 4.45 kN)

Figure 63 shows the strains across the bottom of the bridge along instrument line H for the 100 kip loading sequence at cylinder 2. At lower load, the strains are relatively symmetric about the center of the bridge with higher strains existing on Beams 4 and 5 where the load was applied. As the loading increases, the strains in Beams 4 and 5 become significantly larger than the other beams. However, the peak strains in Beams 4 and 5 are less than the peak strains in the fully loaded beam (8) for the cylinder 1 loading sequence (Figure 62).

Figure 64 provides the bottom strains in the beams along instrument line H for the 100 kip (445 kN) cylinder 3 loading sequence. As with the other loading locations, the strains are highest at the location of the load and taper off away from the loading. However, the strains on the opposite side of the loading are much less than the opposite side strains when the load was at cylinder 1 (Figure 62). In addition, the effective of the damaged beams does not show up in the plots.



**Figure 63: Bottom Strain Profile Instrument Line H (Cylinder 2 – 100 K)**  
 (Note: 1 kip = 4.45 kN)



**Figure 64: Bottom Strain Profile Instrument Line H (Cylinder 3 – 100 K)**  
 (Note: 1 kip = 4.45 kN)

The top strains along instrument line H across the width of the bridge while loading is applied to all cylinders is shown in Figure 65. The top strains are shown since at higher loads the strains in the bottom of the bridge become unusable due to cracking of the concrete. Strain was not monitored in Beam 9 since the poor condition of the concrete did not allow the mounting of a top gage to the beam. In general, the strains increase with increasing load. However, Beam 4 has significantly higher strain as the total loading increased above 249 kips (1,108 kN). Table 9 provides the cylinder loads for each total load the strains were plotted for in Figure 65. Though the load is highest on cylinder 2 for some of the total load plots, it is not significantly higher than the load in cylinder 1 or 3. At the 364 kip (1,620 kN) total load, the load on cylinder 2 is even lower than the load on cylinder 2. Therefore, it is concluded that a larger portion of the load is being transferred into Beam 4. This makes sense since Beam 4 was not damaged.

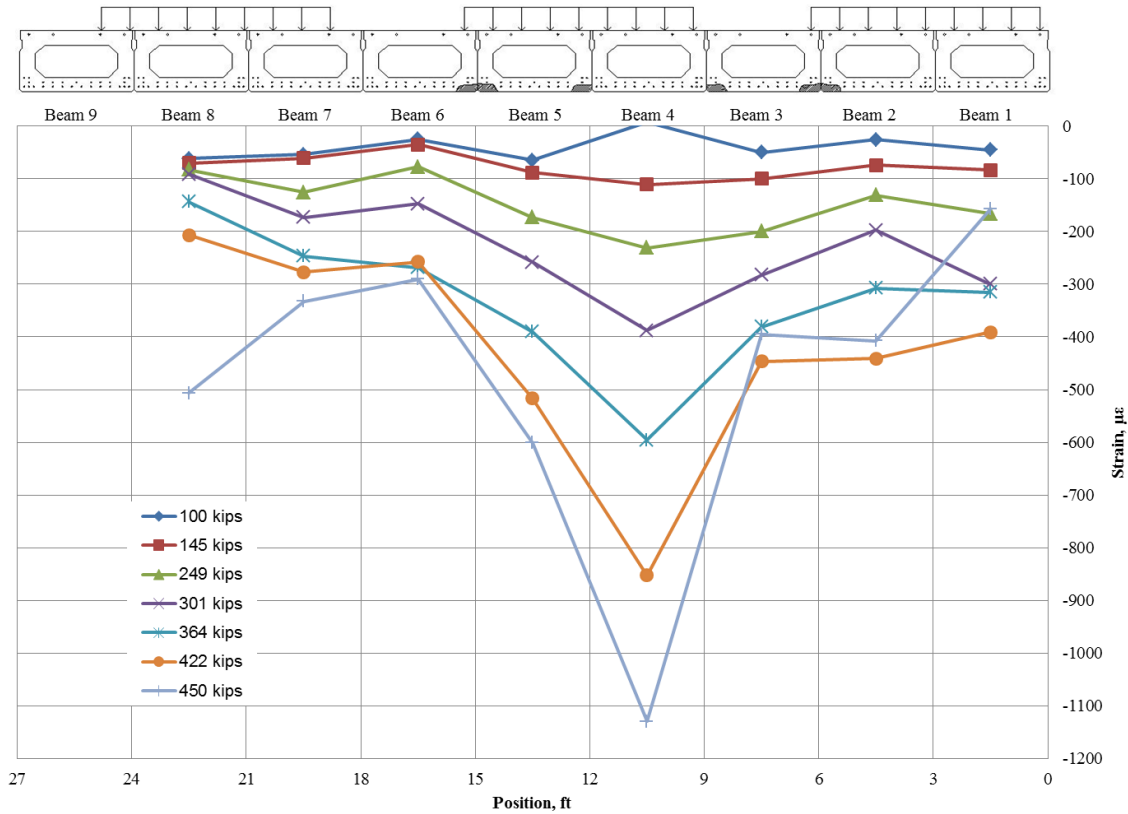


**Figure 65: Top Strain Profile Instrument Line H (All Cylinders)**  
 (Note: 1 kip = 4.45 kN)

**Table 9: Cylinder Load Distribution (East Span)**

Total Load (kips)	Cylinder Load (kips)		
	1	2	3
100	48	52	0
145	42	45	59
249	90	97	62
301	107	118	76
364	138	125	100
422	135	156	132
450	156	156	138

(Note: 1 kip = 4.45 kN)

Figure 66 provides the average top strain along the instrument line H versus the total applied load to the East span. Though the strains are negative (compression), the absolute values were plotted for comparison with other data from other spans. As can be seen from Figure 66, the plot is relatively linear until approximately 250 kips (1,113 kN). The plot then becomes relatively linear again with a reduced slope. The behavior shown in the plot is somewhat similar to that of a single beam.

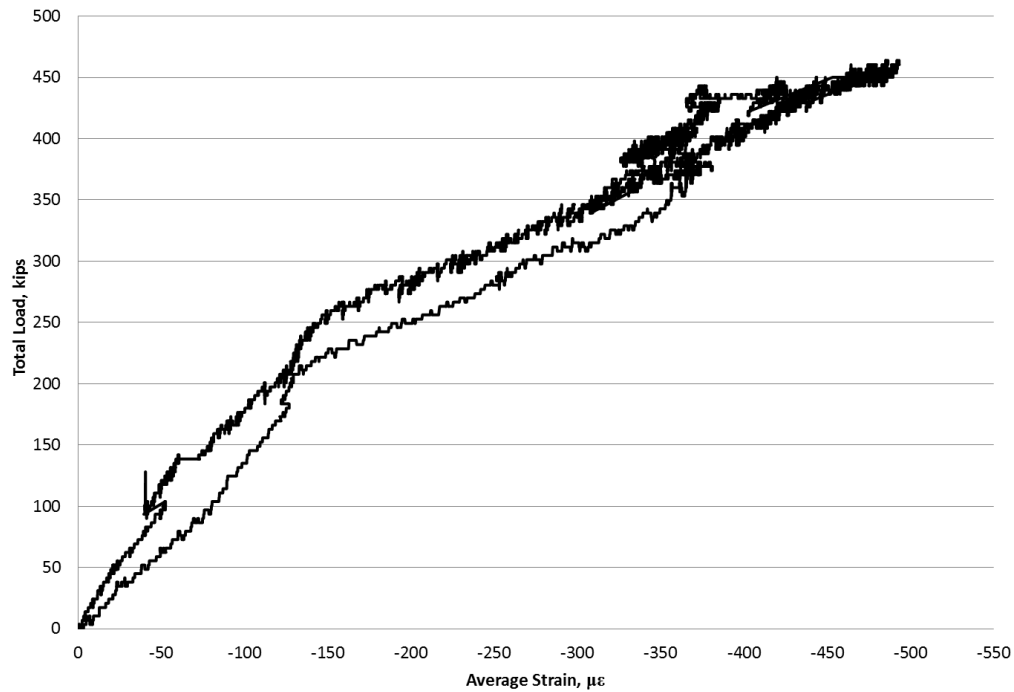


**Figure 66: Average Top Strain vs Load - Instrument Line H (All Cylinders)**  
 (Note: 1 kip = 4.45 kN)

During ultimate loading of the East span, flexural cracking was initiated in the beams and then resulted in water leaking from the cracks indicating the voids of the boxes contained water. This water was significant judging from the duration of leakage (see Figure 67). The bridge failed by crushing of the top flange concrete mainly in the outer beams (Beams 1 and 9). Additional load was no longer able to be supported by the bridge and testing was terminated in order to assure damage to the loading system did not occur. Figure 68 shows the top flange of Beam 1 crushing significantly. Figure 69 shows the flexural cracking and concrete crushing failure of Beam 1. Figure 70 shows the crushing of the top flange of Beam 9 and the buckling of the compression reinforcement. Figure 71 shows the flexural cracking and spalling of Beam 9.



**Figure 67: Flexural Cracking and Void Water Leakage**



**Figure 68: Concrete Crushing in Beam 1**



**Figure 69: Flexural Cracking and Concrete Crushing in Beam 1**



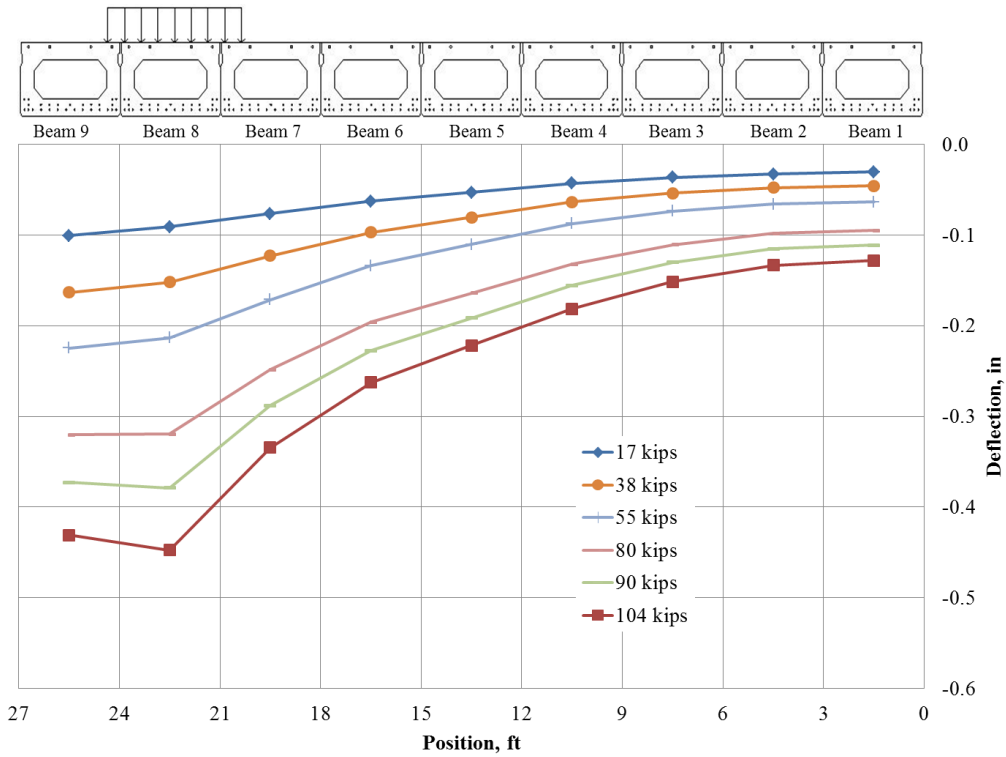
**Figure 70: Concrete Crushing and Buckling of Compression Reinforcement in Beam 9**



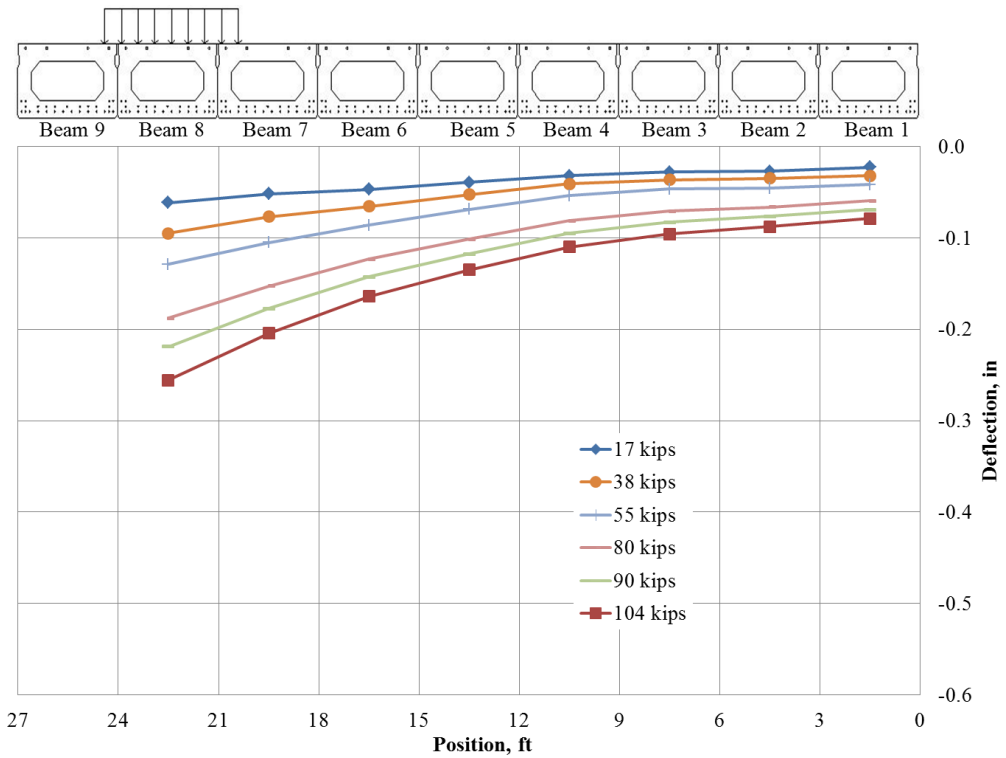
**Figure 71: Flexural Cracking and Spalling of Concrete in Beam 9**

### **3.4.2 Center Span**

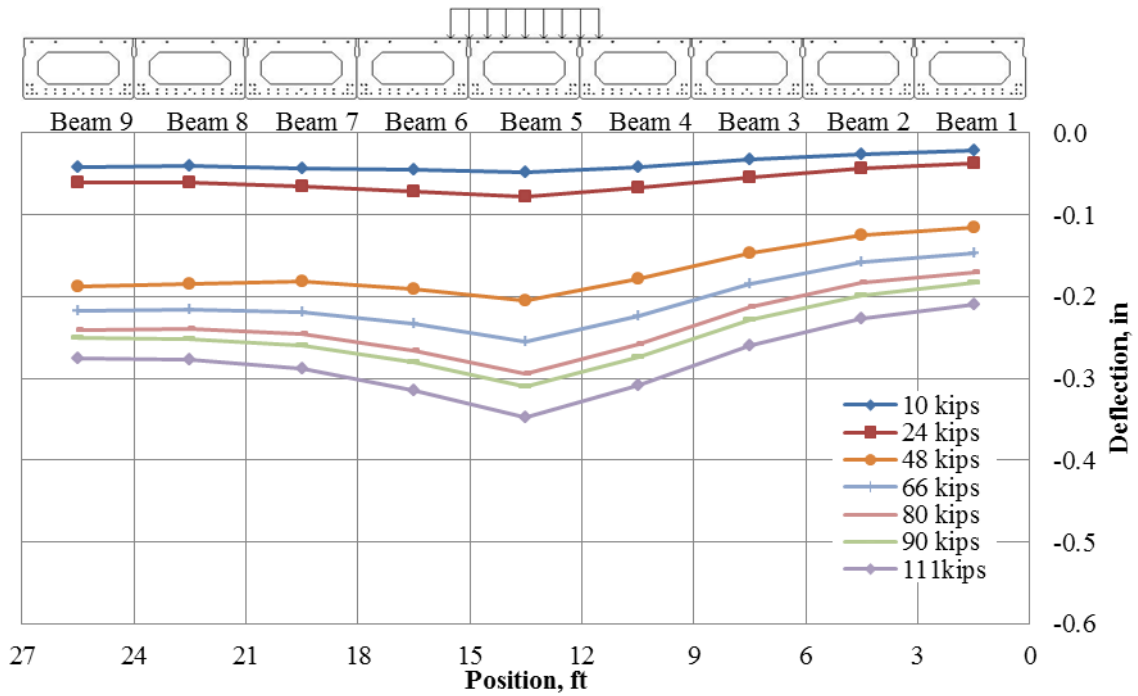
Figures 72-77 show the deflection response of the bridge as the load increases to approximately 100 kips (445 kN) on a single cylinder while no load is applied to the other cylinders. Deflections were not monitored on Beam 9 for instrument line D because of the poor condition of the top of Beam 9 would not allow an anchor to be set in order to mount the wire of the string potentiometer. In general, for all three cylinders and both instrument lines, the deflections increased fairly consistently across the bridge as the load was increased. However, for the loading applied to cylinder 2, larger deflections occurred on the north edge of the bridge (Beams 8 and 9) than on the south edge (Beams 1 and 2). This was observed at both instrument lines E and D. This implied that the northern beams were less stiff than the southern beams or load transfer was not completely symmetrical. This may have been due to the effect of the asphalt being left in place on the south side. The asphalt may not have directly increased stiffness, but rather shifted the neutral axis of the beams and/or improved the distribution of the load to the beams longitudinally and transversely. The figures for the loading applied by cylinder 3 showed that once the loading was reduced to 55 kips (245 kN), the deflection was higher than at slightly higher loads of 59 kips (263 kN) during the initial loading stage. This implies some damage to the beams accompanied by permanent deformation.



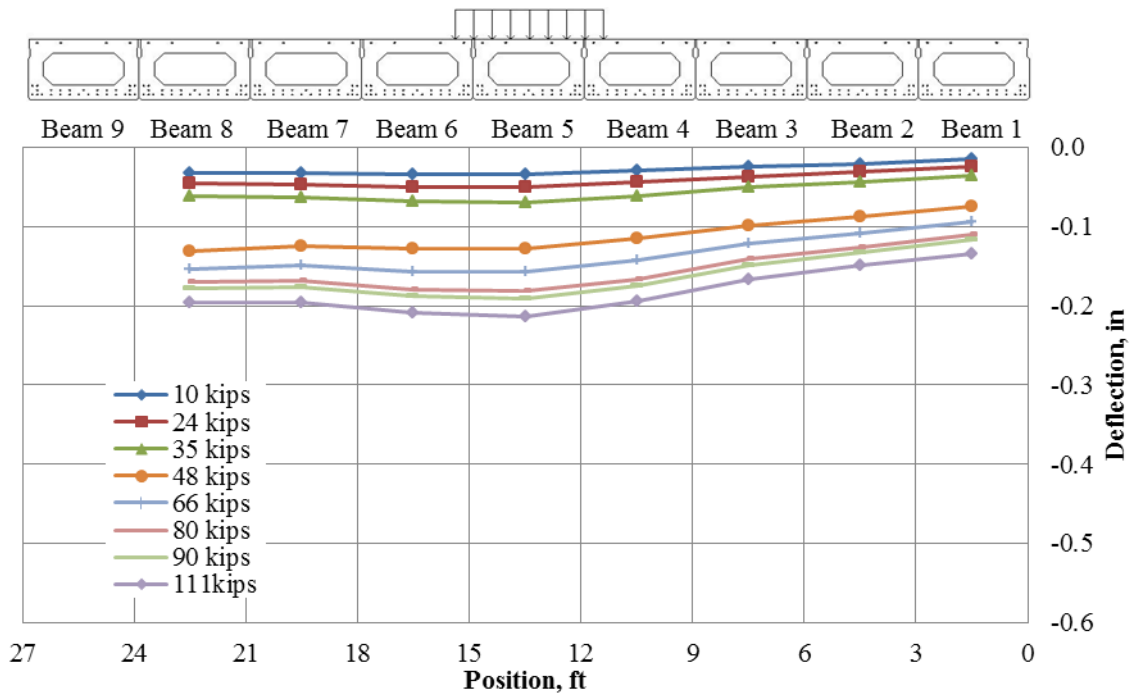
**Figure 72: Deflection Profile Instrument Line E (Cylinder 1 – 100 K)**  
 (Note: 1 kip = 4.45 kN, 1" = 25.4 mm)



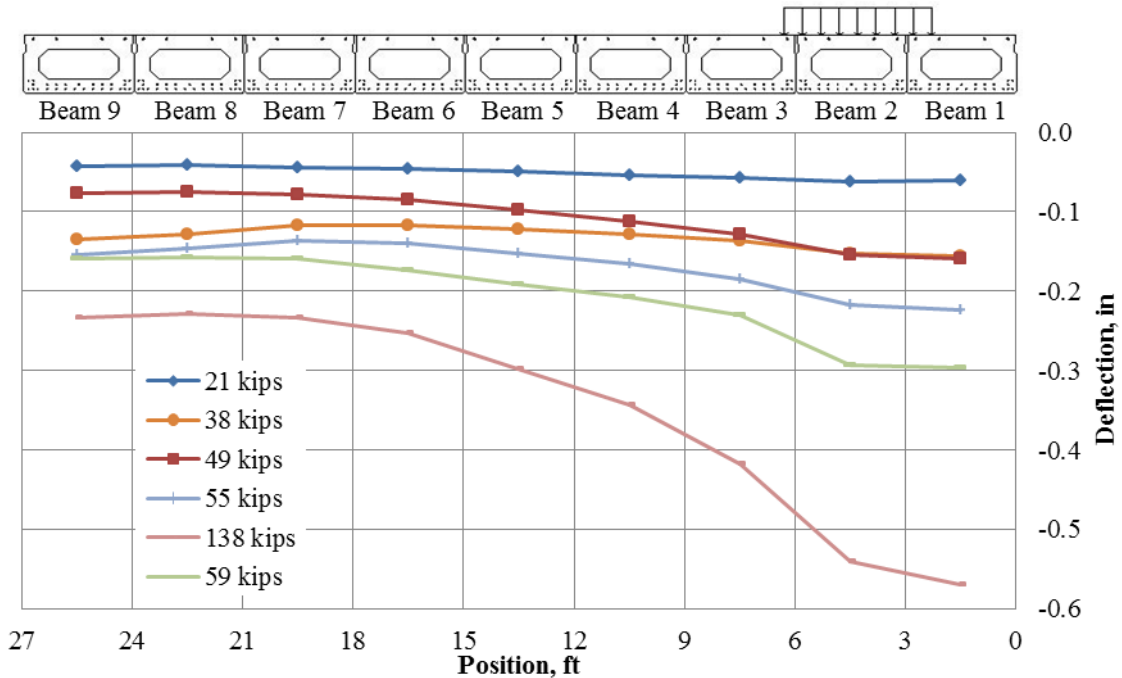
**Figure 73: Deflection Profile Instrument Line D (Cylinder 1 – 100 K)**  
 (Note: 1 kip = 4.45 kN, 1" = 25.4 mm)



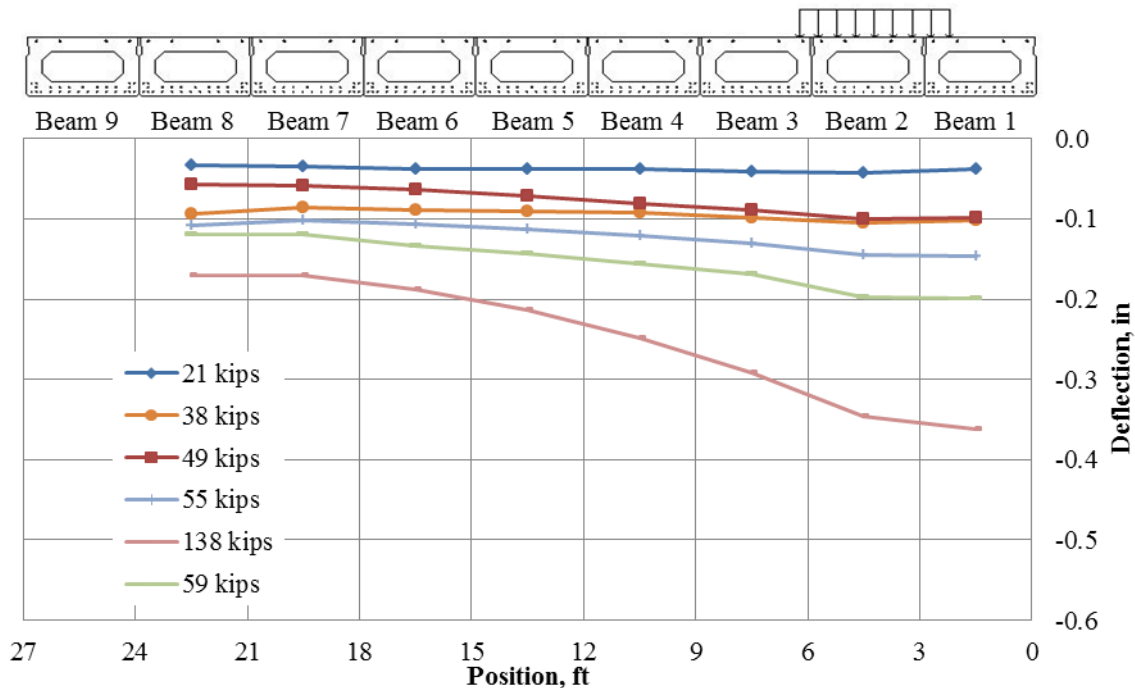
**Figure 74: Deflection Profile Instrument Line E (Cylinder 2 – 100 K)**  
 (Note: 1 kip = 4.45 kN, 1" = 25.4 mm)



**Figure 75: Deflection Profile Instrument Line D (Cylinder 2 – 100 K)**  
 (Note: 1 kip = 4.45 kN, 1" = 25.4 mm)



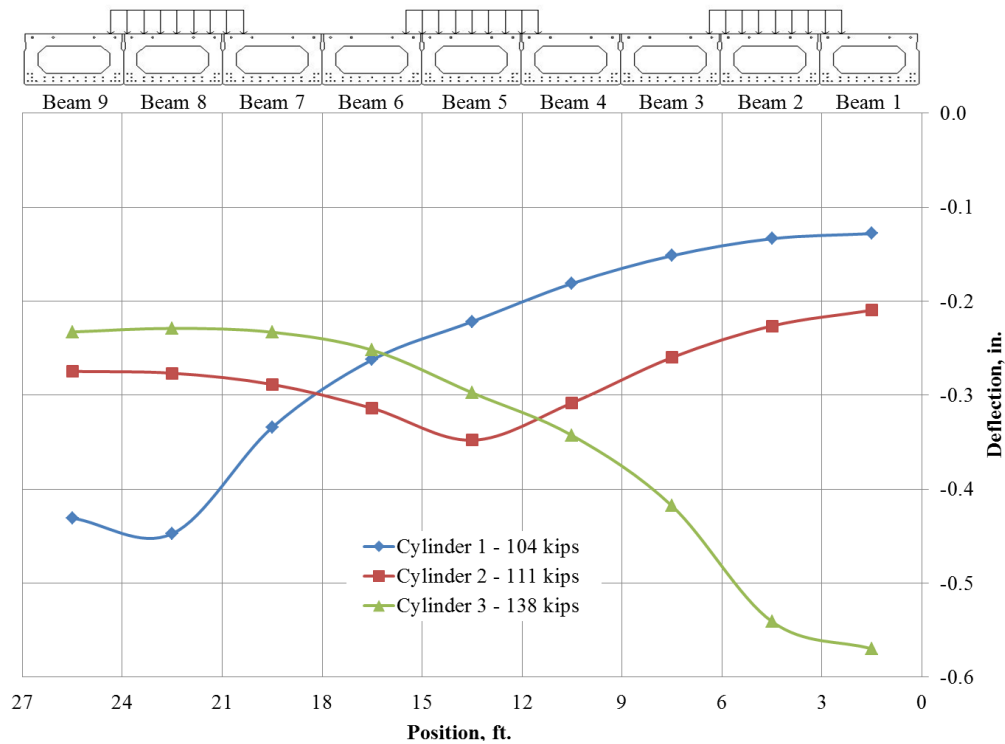
**Figure 76: Deflection Profile Instrument Line E (Cylinder 3 – 100 K)**  
 (Note: 1 kip = 4.45 kN, 1" = 25.4 mm)



**Figure 77: Deflection Profile Instrument Line D (Cylinder 3 – 100 K)**  
 (Note: 1 kip = 4.45 kN, 1" = 25.4 mm)

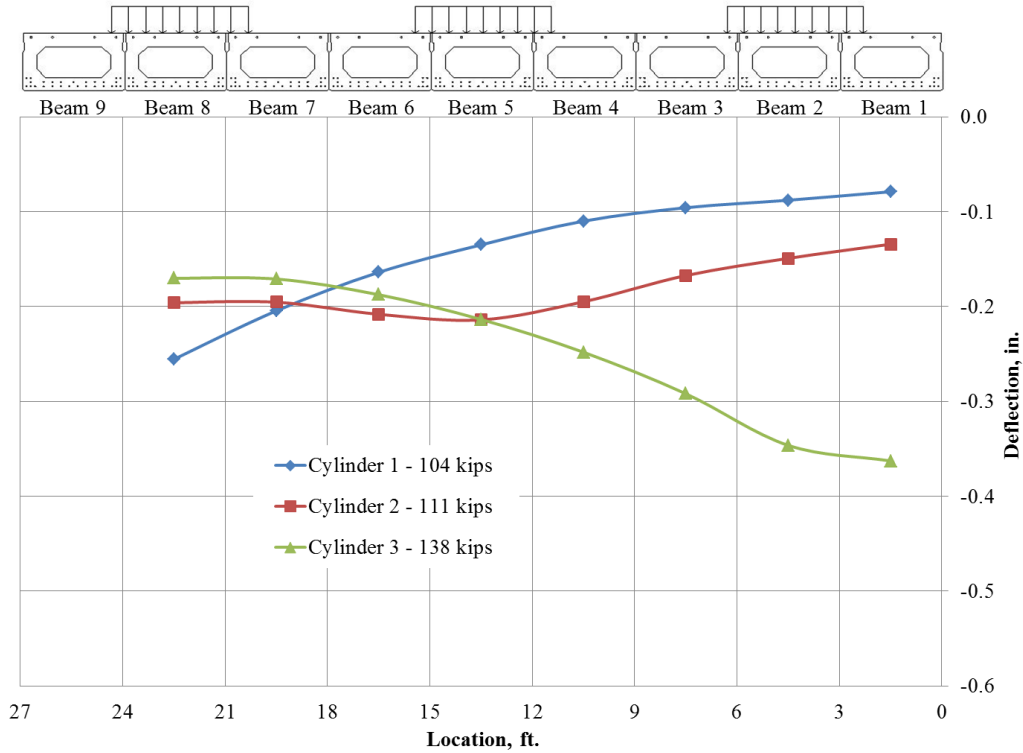
Figure 78 shows the deflection profile along instrument line E for an approximately 100 kip (445 kN) load on each of the three cylinders. The deflections are consistent with the loading in that the deflections for cylinders 1 and 3 are close to mirror images. The deflections for

cylinder 3 are higher due to the higher load on cylinder 3 compared to cylinder 1. The other issue is near the opposite end from the loading. For cylinder 1, the deflections continue to decrease on Beams 3 to 1. However for cylinder 3, the deflections on opposite end of the load location for Beams 7-9 are nearly constant. In addition, the deflections from the loading of cylinder 2 are skewed higher toward Beam 9 (north side). This leads to the belief that this side of the bridge was not as stiff as the south side. Again, this may have been from the asphalt being left in place over the south side beams. The D instrument line shows similar results to the E instrument line (Figure 79).



**Figure 78: Deflection Profiles Instrument Line E**

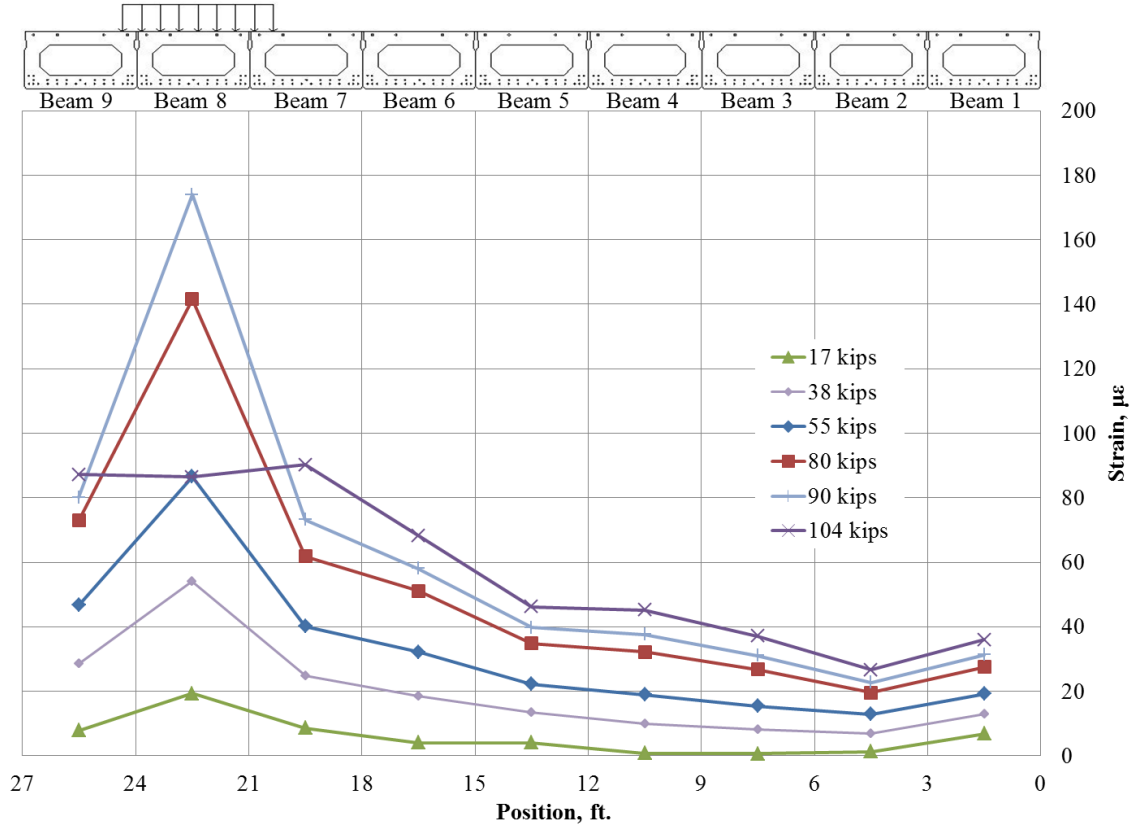
(Note: 1 kip = 4.45 kN, 1" = 25.4 mm)



**Figure 79: Deflection Profiles Instrument Line D**

(Note: 1 kip = 4.45 kN, 1" = 25.4 mm)

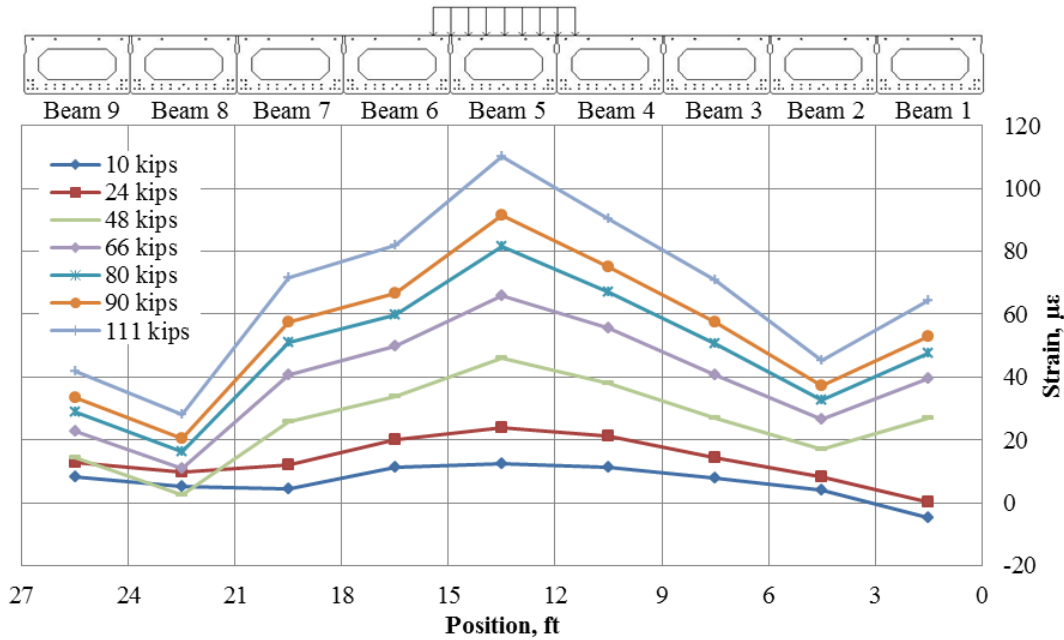
The strains in the bottom of the beams along instrument line E for the individual 100 kip cylinder loads are shown in Figures 80-82. In Figure 80, the strains increase with load as expected. The strains are highest in the beams that are directly loaded. However, the strain in Beam 8 drops when the load increases from 90 to 104 kips. This appears to be an issue with the concrete the gage was adhered to or the strain gage itself. The strains across the beams appear to be slightly more linearly distributed than the strains experienced in the East span for the same loading condition. This was likely due to the damage caused in the East span.



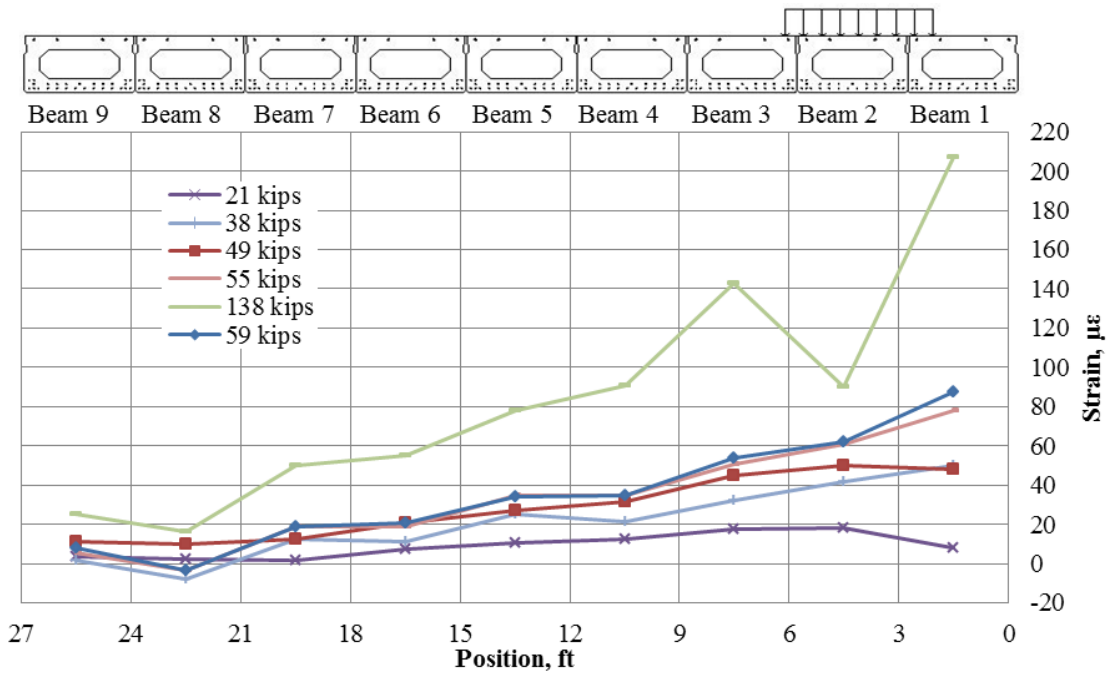
**Figure 80: Bottom Strain Profile Instrument Line E (Cylinder 1 – 100 K)**  
 (Note: 1 kip = 4.45 kN, 1" = 25.4 mm)

Figure 81 shows the bottom strain at instrument line E for the 100 kip (445 kN) loading in cylinder 2. The strain in Beam 8 shows a large drop in strain and may signify something occurred either to the gage or concrete during the loading of cylinder 1 above 90 kips. Another interesting observation is that the strain in Beam 2 also shows and relatively large drop in comparison to the surrounding beam strains.

The bottom strain at instrument line E for the 100 kip (445 kN) loading in cylinder 3 is shown in Figure 82. At low loads the strain in Beam 8 was actually slightly negative which continues to indicate something occurred either to the gage or concrete during the loading of cylinder 1. The strain in Beam 2 also shows expected behavior until the load increases to 138 kips (614 kN), in which the strain in Beam 2 drops in comparison to the surrounding beam strains.



**Figure 81: Bottom Strain Profile Instrument Line E (Cylinder 2 – 100 K)**  
 (Note: 1 kip = 4.45 kN, 1" = 25.4 mm)



**Figure 82: Bottom Strain Profile Instrument Line E (Cylinder 3 – 100 K)**  
 (Note: 1 kip = 4.45 kN, 1" = 25.4 mm)

After loading and unloading with each individual cylinder, load was applied to each cylinder and maintained as another cylinder increased load. Figure 83 shows the deflection across the bridge at instrument line E as the total load from all cylinders increased. Table 10 provides how the total load was distributed from the three cylinders. When the maximum load of approximately 450 kips (2,003 kN) was obtained, the bridge was no longer able to support

higher total load and deflections increased. Initially, the deflections are fairly consistent across the width of the bridge. However, after the maximum load was reached Beams 1, 2 and 8 showed slightly higher deflections even though more load is applied from cylinder 2 to the middle bridge beams compared to the outside beams. The deflection profile remained the same even after the load was decreased. The deflection across the width of the bridge is much higher at lower loads after the peak loading was reached, resulting in permanent deformation. It should be noted that the data for the string potentiometer attached to Beam 5 was not usable from the test.

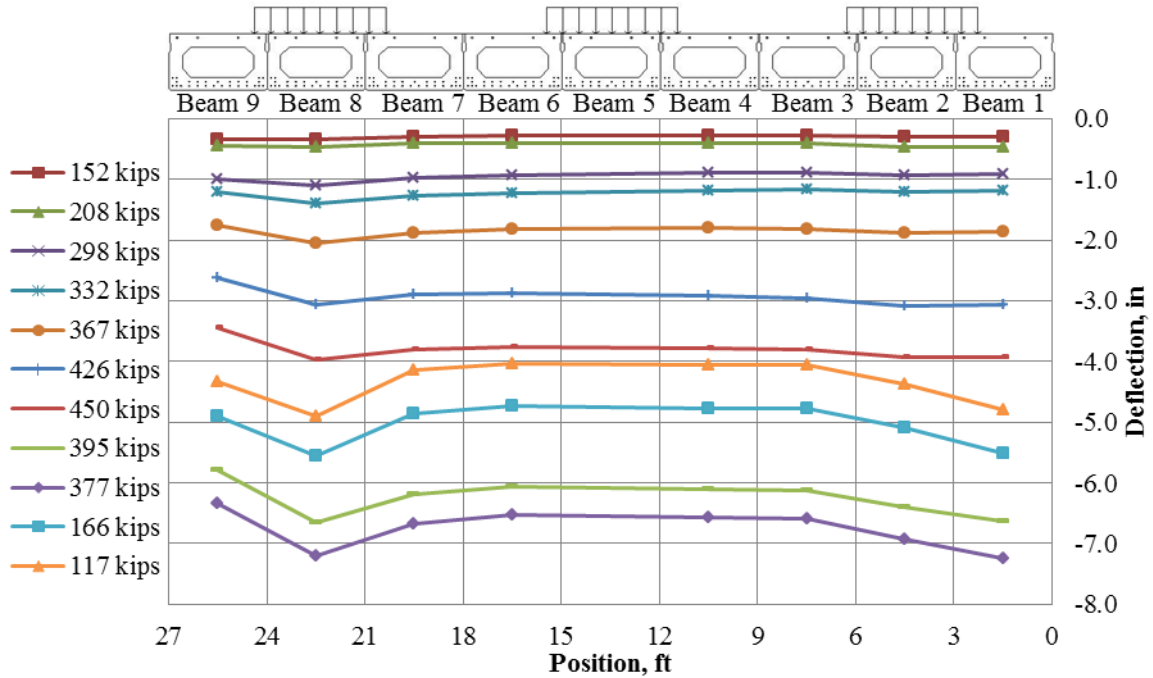


**Figure 83: Total Load and Instrument Line E Deflection (Center Span)**

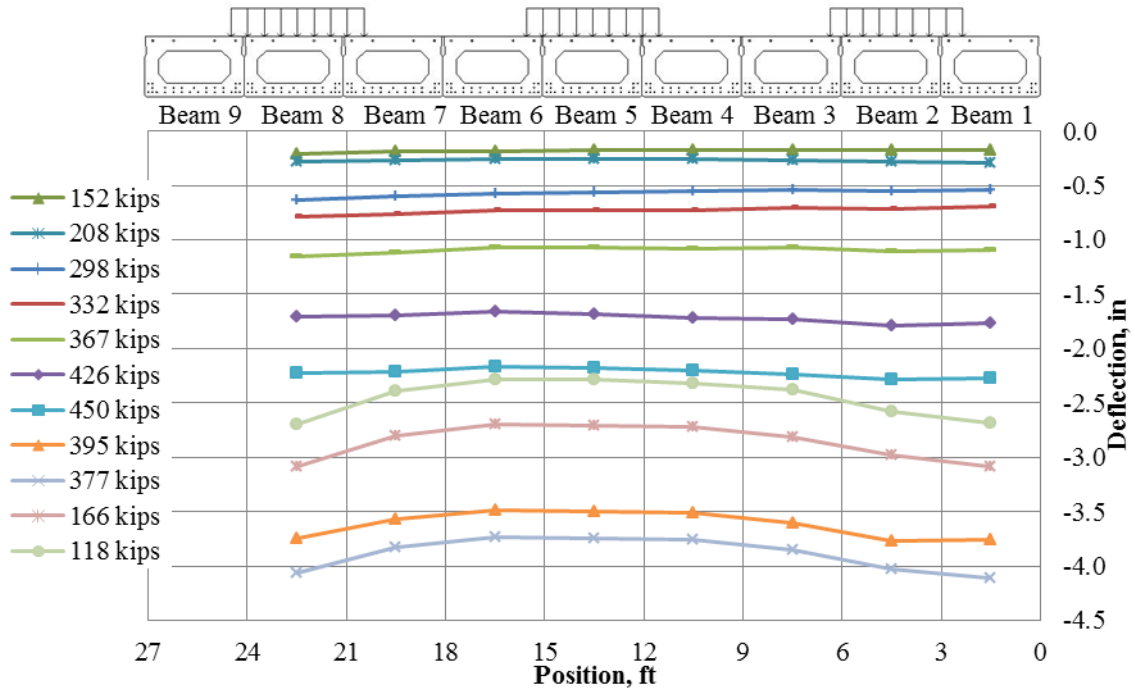
(Note: 1 kip = 4.45 kN, 1" = 25.4 mm)

**Table 10: Cylinder Load Distribution (Center Span)**

Total Load (kips)	Cylinder Load (kips)		
	1	2	3
152	55	45	52
208	66	59	83
298	111	87	100
367	132	104	132
426	128	135	163
450	142	159	149
395	100	180	114
377	97	183	97
166	35	93	38
117	20	73	24

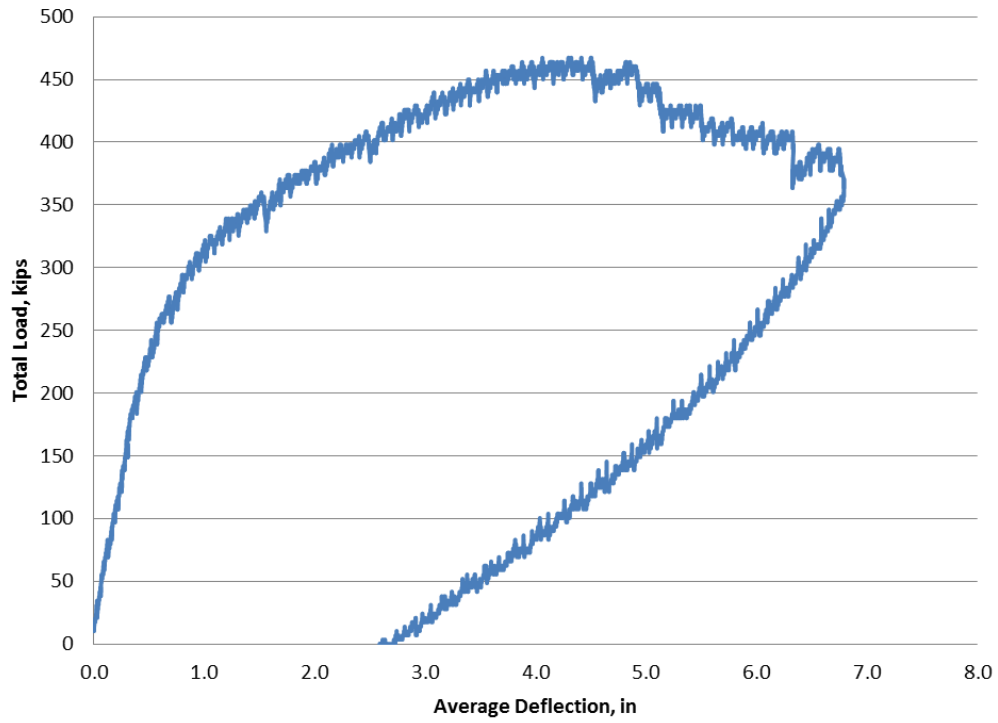
(Note: 1 kip = 4.45 kN, 1" = 25.4 mm)

Figure 84 shows the deflection across the bridge at instrument line D as the total load from all cylinders increased. The behavior is similar to instrument line E with the exception that the deflections are much lower due to the location of instrument line D.



**Figure 84: Total Load and Instrument Line D Deflection (Center Span)**  
 (Note: 1 kip = 4.45 kN, 1" = 25.4 mm)

Figure 85 and 86 show the total load from all the cylinders versus the average deflection of all the beams along instrument lines E and D, respectively. The figures show a linear behavior for the bridge until the total load reaches approximately 200 kips (890 kN). The average deflection of the bridge then becomes nonlinear. After the maximum load of approximately 450 kips (2,003 kN) was reached, the load dropped off as deflection increased. The bridge was then unloaded and permanent average deflections of approximately 2.75" (69.9 mm) and 1.50" (38.1 mm) remained at instrument lines E and D, respectively.



**Figure 85: Total Load and Instrument Line E Average Deflection (Center Span)**  
 (Note: 1 kip = 4.45 kN, 1" = 25.4 mm)

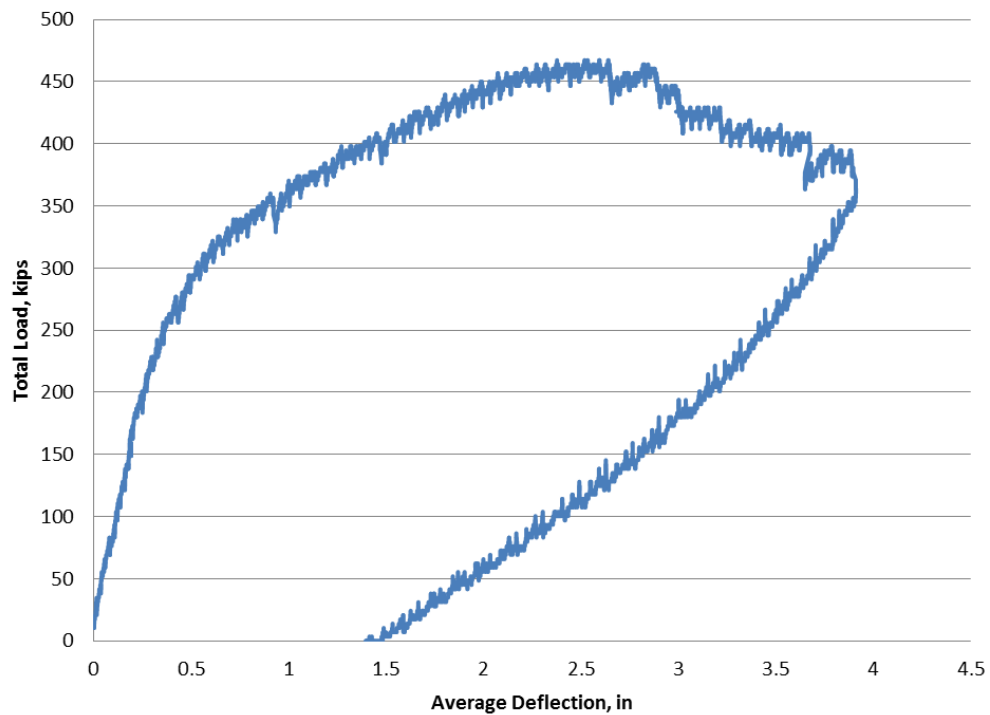


**Figure 86: Total Load and Instrument Line D Average Deflection (Center Span)**  
 (Note: 1 kip = 4.45 kN, 1" = 25.4 mm)

Figure 87 shows the center span after testing was terminated. Figure 88 shows the failure of Beam 1 near midspan by crushing of the top flange and flexural cracking of the bottom flange. The top of Beams 1-3 are shown in Figure 88. The asphalt over Beam 1 is buckling which is likely the result of the crushing of the top flange of Beam 1. Figure 89 shows large relative deflections between Beams 2 and 3 caused by failure of the shear keys between the beams. Figure 90 shows the large deflection of Beam 9 and the failure near midspan. Figure 91 shows the closer view of the underside of Beams 8 and 9 along with the cracking and spalling of concrete. Figure 92 shows the crushing of the top flange of Beam 8.



**Figure 87: Beam 1 Failure**



**Figure 88: Buckling of Asphalt Overlay on Beams 1-3**



**Figure 89: Failure of Shear Key**



**Figure 90: Spalling and Crushing of Beam 9**



**Figure 91: Spalling and Cracking of Beams 8 and 9**



**Figure 92: Crushing of Beam 8 Top Flange**

### **3.4.3 West Span**

Figures 93-98 show the response of the west span as the load increases to approximately 100 kips (445 kN) on a single cylinder while no load is applied to the other cylinders. In general, for all three cylinders and both instrument lines, the deflections increased fairly consistently across the bridge as the load was increased. For the loading on cylinder 1 and deflections along instrument line A (Figure 93), Beam 8 deflected the most as would be expected since the majority of the load was applied to Beam 8. However, the deflection of Beam 9 was greater than that of Beam 7 even though Beam 7 had about 1/3 of the load applied to it and no load was directly applied to Beam 9. Along instrument line B, the deflection of Beam 8 and 9 were basically the same throughout the loading process (Figure 94). The behavior of Beam 9 was likely due to its poor condition.

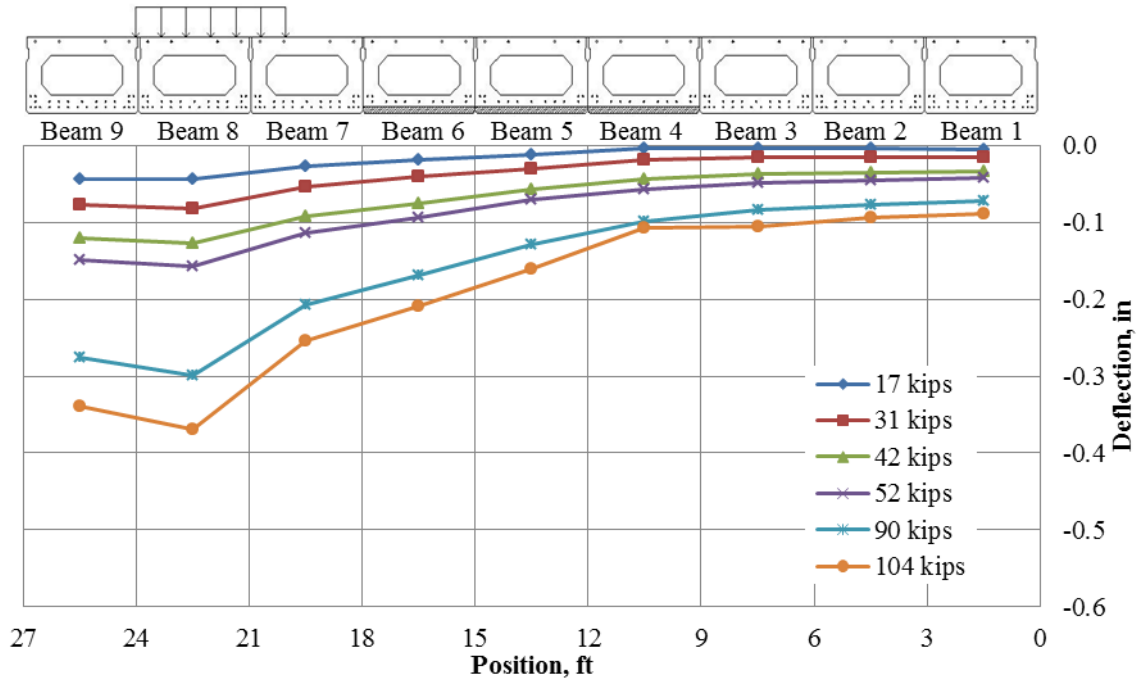


**Figure 93: Deflection Profile Instrument Line A (Cylinder 1 – 100 K)**  
 (Note: 1 kip = 4.45 kN, 1" = 25.4 mm)

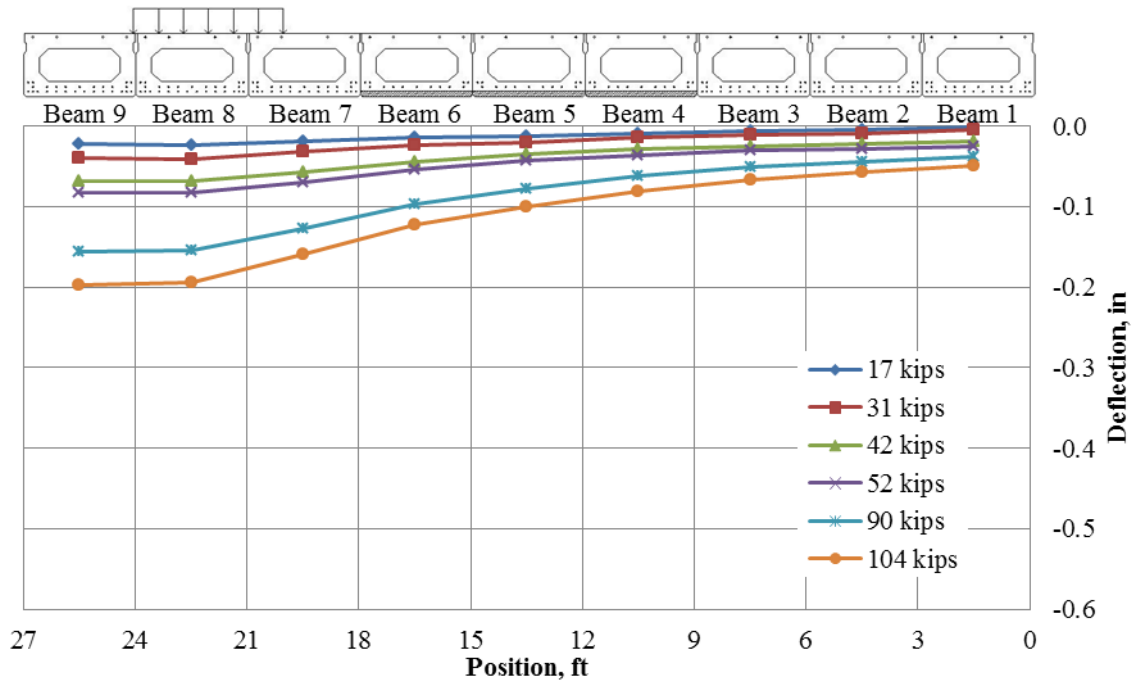


**Figure 94: Deflection Profile Instrument Line B (Cylinder 1 – 100 K)**  
 (Note: 1 kip = 4.45 kN, 1" = 25.4 mm)

The loading of cylinder 2 applied approximately 2/3 of the load to Beam 5 and the remaining 1/3 to Beam 4. The deflections of the beams across the bridge at instrument line A were a little sporadic at lower loads but then smoothed out at higher load (Figure 95). Beam 5 had the largest deflection and the deflection was nearly symmetric about Beam 5. Along instrument line B, Beam 4 and 5 had approximately the same deflection at lower loads, but at higher loads Beam 4 actually had slightly higher deflections (Figure 96). The largest deflections from cylinder 2 loading were much less than that for cylinder 1 loading showing good distribution of the load.

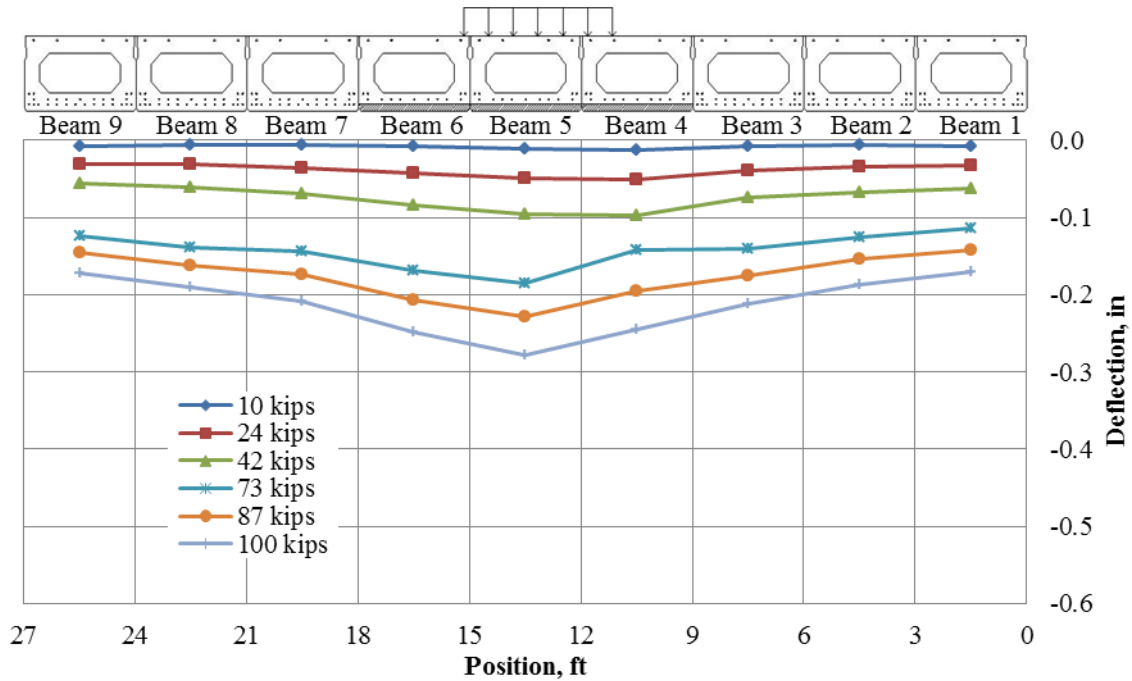


**Figure 95: Deflection Profile Instrument Line A (Cylinder 2 – 100 K)**

(Note: 1 kip = 4.45 kN, 1" = 25.4 mm)

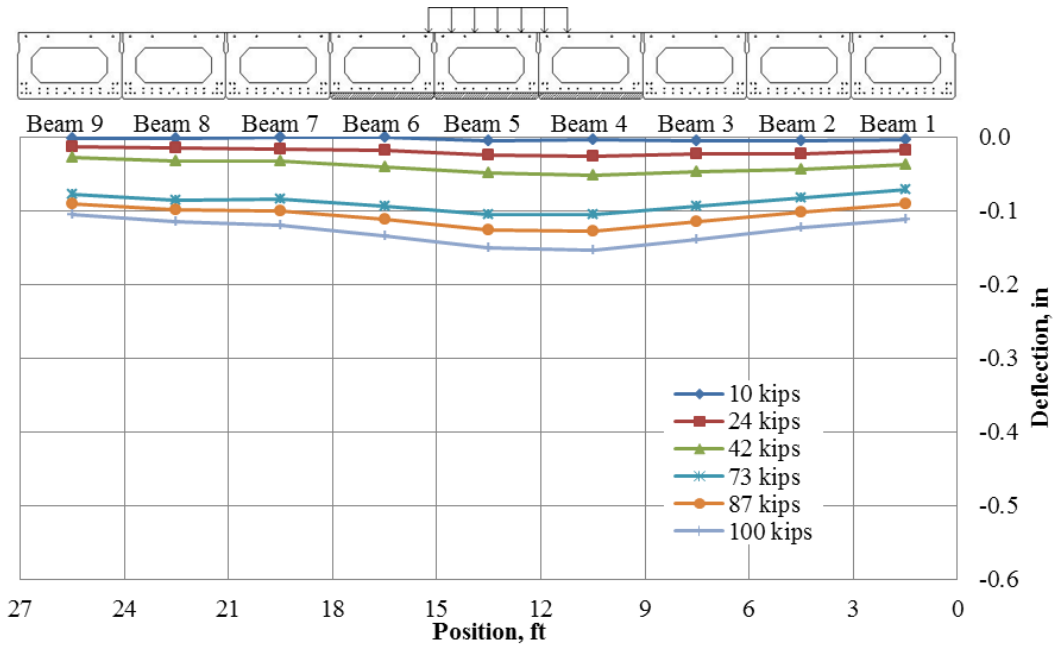


**Figure 96: Deflection Profile Instrument Line B (Cylinder 2 – 100 K)**  
 (Note: 1 kip = 4.45 kN, 1" = 25.4 mm)

The loading on cylinder 3 showed small increases in deflections at Beam 4 along instrument line A as the loads increased (Figure 97). The largest deflections occurred at Beams 1 and 2 and were relatively similar. This as was expected due to the loading applied directly to these beams. However, Beam 1 showed higher deflection than Beam 2 along instrument line B (Figure 98).

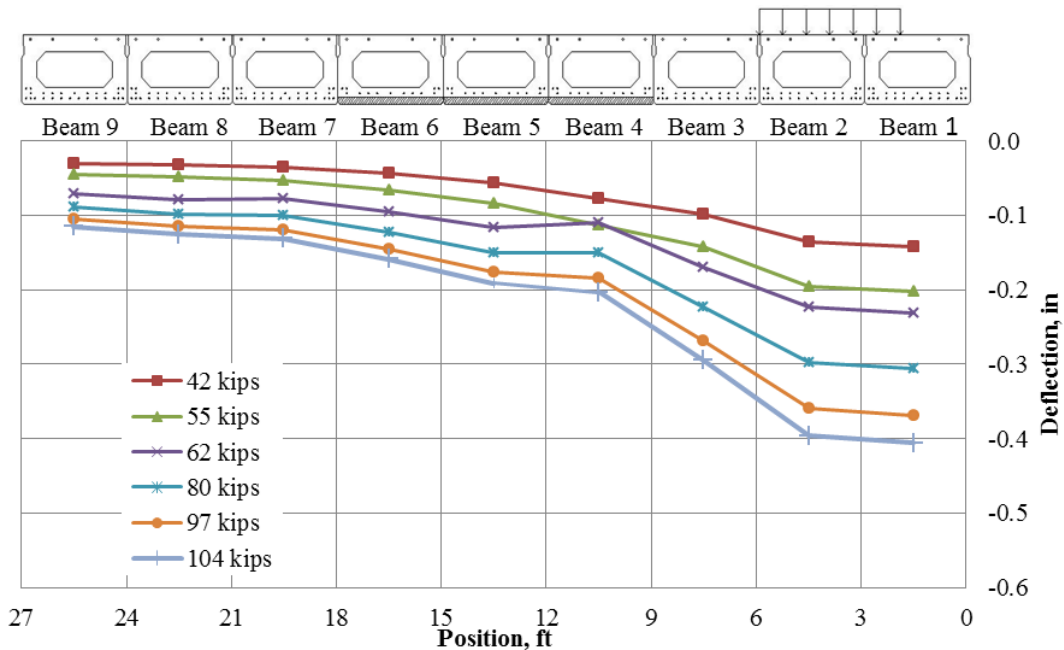


**Figure 97: Deflection Profile Instrument Line A (Cylinder 3 – 100 K)**  
 (Note: 1 kip = 4.45 kN, 1" = 25.4 mm)

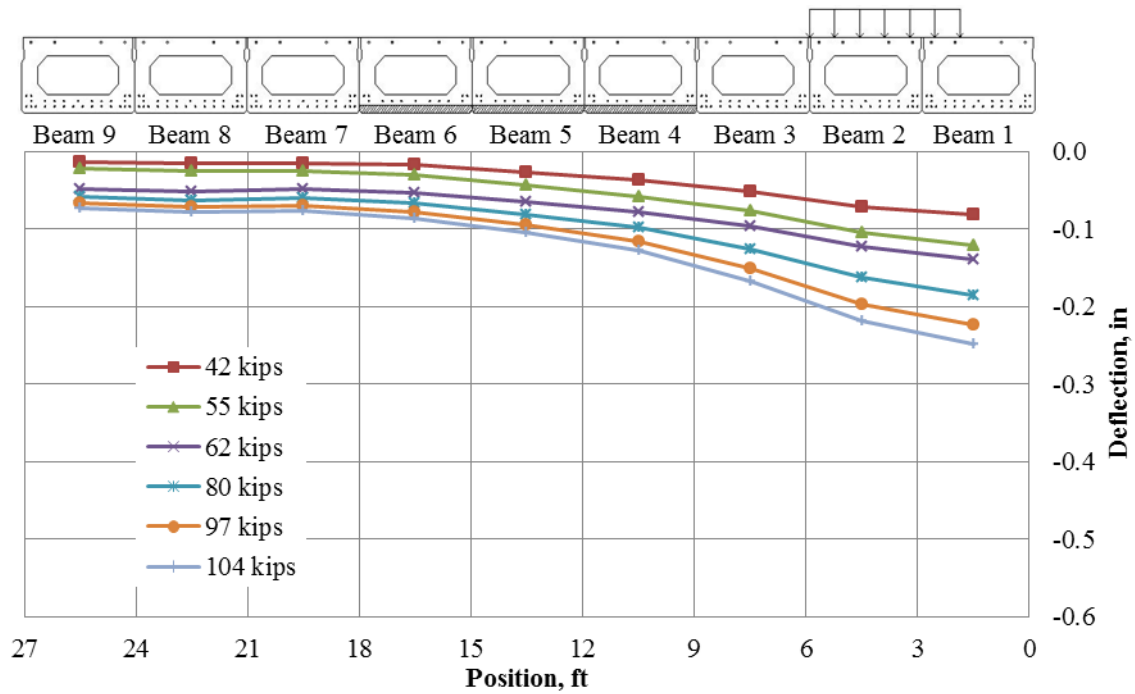


**Figure 98: Deflection Profile Instrument Line B (Cylinder 3 – 100 K)**

(Note: 1 kip = 4.45 kN, 1" = 25.4 mm)

Figure 99 shows the deflections across the bridge for 100 kip (445 kN) loads on each of the three independent cylinders. The deflections are consistent with the loading in that the deflections are symmetric for cylinder 2 and the deflections for cylinders 1 and 3 are close to mirror images. The differences for deflections from loading at cylinders 1 and 3 can be attributed to cylinder 1 loaded two interior beams (7 and 8) while cylinder 3 loaded one inside and one outside beam (beams 1 and 2). Loading from cylinder 3 also produced higher relative deflections across the width of the bridge. This behavior is also showed in Figure 100 at instrument line B.

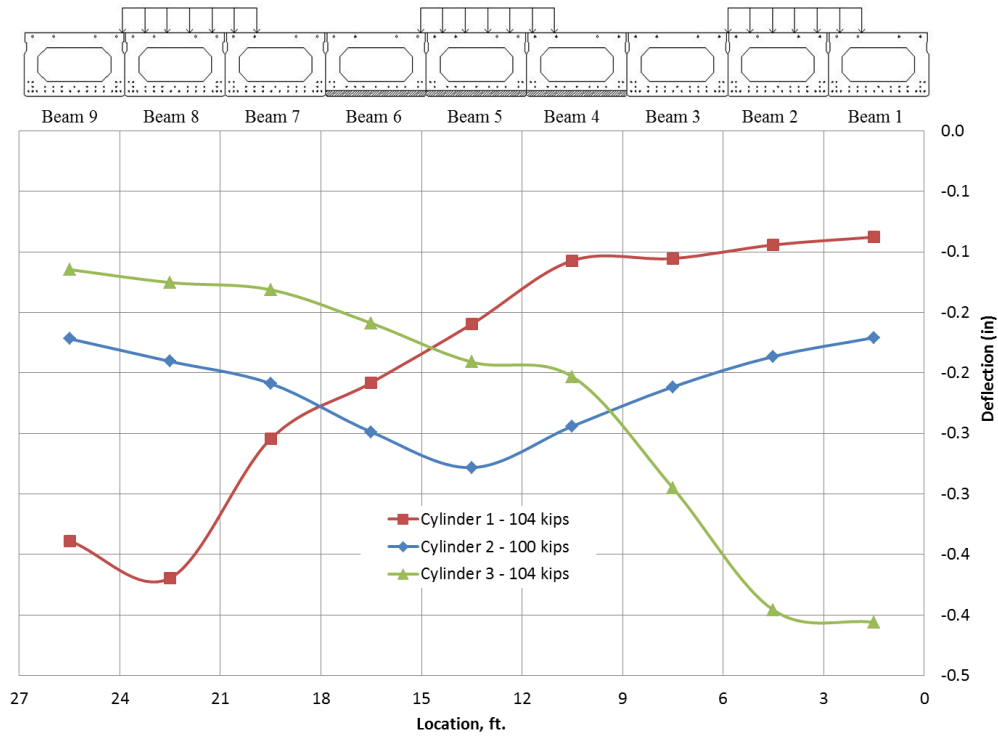


**Figure 99: Deflection Profiles Instrument Line A**  
 (Note: 1 kip = 4.45 kN, 1" = 25.4 mm)

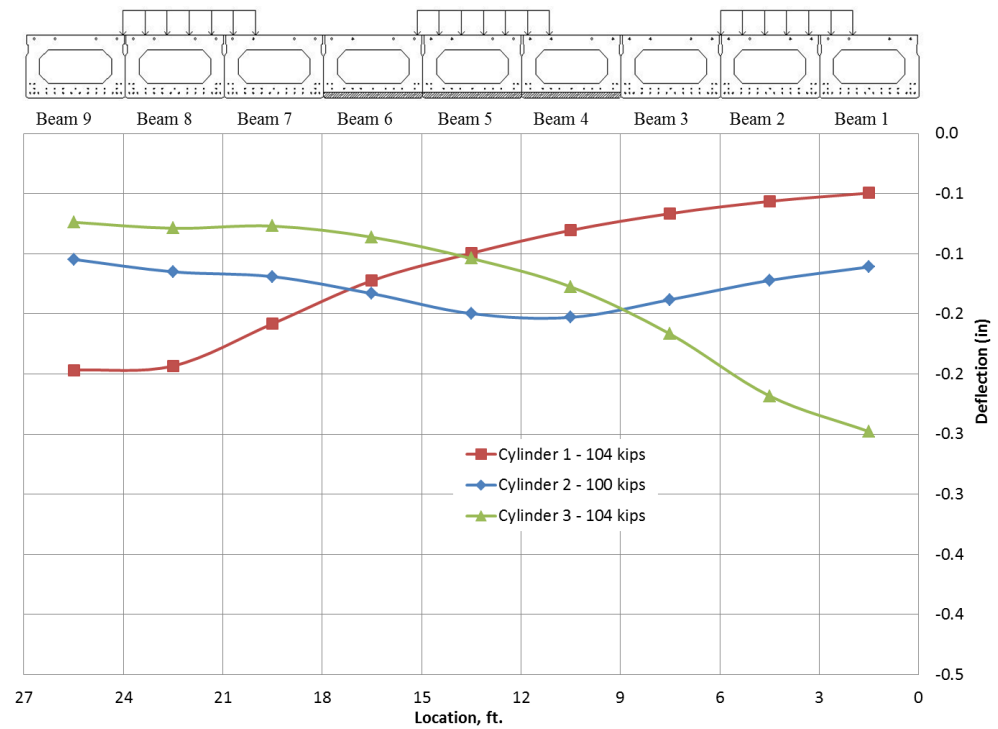
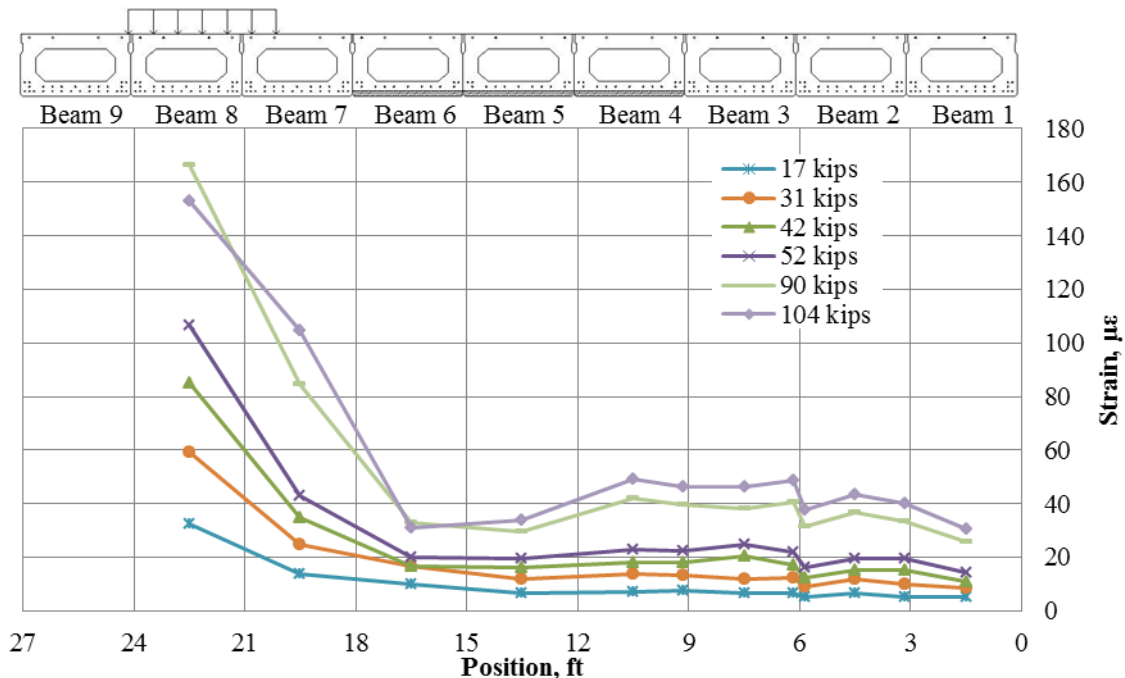


**Figure 100: Deflection Profiles Instrument Line B**  
 (Note: 1 kip = 4.45 kN, 1" = 25.4 mm)

Figures 101-103 show the strains in the bottom of the beams along instrument line A for the individual loading of cylinders 1-3 to 100 kips (445 kN). Positive strains are tensile. In addition, the distance along the width of the bridge is provided since multiple gages were mounted on some beams. In particular, Beam 2 had 3 gages placed along its width, and Beams 3 and 4 each had 2 gages mounted along their width.

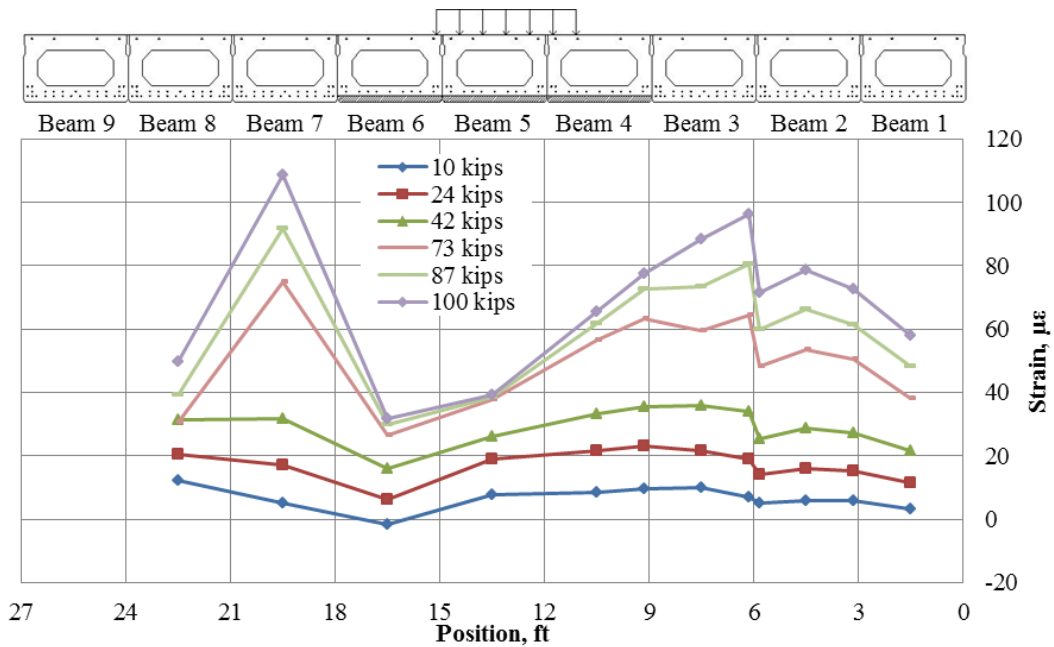
In Figure 101 where cylinder 1 was loaded to 100 kips (445 kN), the behavior of the bottom strains across the width of the bridge were generally expected. The strain was highest for Beam 8, which was at the location of the loading from cylinder 1. Beam 9 showed no change in strain is was likely due to failure of the gage. The remaining strains increased in the beams as the load increased. However, it should also be noted that as the load increased from 42 kips (187 kN) to 104 kips (463 kN), the strain in Beams 5 (13.5 ft.) and 6 (16.5 ft.) showed little increase in strain while the strains in the other beams increased. Beams 5 and 6 were two of the three beams that were damaged, but the other damaged beam (Beam 4) did not exhibit the same behavior. At higher loads, the strains between Beams 2 and 3 showed a jump in the strain. It did appear the undamaged beams (Beams 2 and 3) started to acquire more strain than the damaged beams.

Figure 102 provides the bottom strain data along instrument line A for the width of the bridge as cylinder 2 was loaded to approximately 100 kips (445 kN). Even though the load was applied primarily to Beams 4 (10.5 ft.) and 5 (13.5 ft.), the strains in damaged Beams 4, 5 and 6 showed lower strain than the adjacent beams (Beams 4 and 7) especially at higher loads. This was likely due to translation of the damaged beams due to their damage states. The jump in strain between Beams 2 and 3 are also still noticeable.



**Figure 101: Bottom Strain Profile Instrument Line A (Cylinder 1 – 100 K)**

(Note: 1 kip = 4.45 kN, 1' = 0.305 m)



**Figure 102: Bottom Strain Profile Instrument Line A (Cylinder 2 – 100 K)**  
 (Note: 1 kip = 4.45 kN, 1' = 0.305 m)

The bottom strain data along instrument line A for the width of the bridge as cylinder 3 was loaded to approximately 100 kips is shown in Figure 103. Even though the load was applied primarily to Beams 1 (1.5 ft.) and 2 (4.5 ft.), the strains in damaged Beams 4, 5 and 6 showed lower strain than the adjacent beams (Beams 4 and 7) especially at higher loads. This was likely due to translation of the damaged beams due to their damage states. The jump in strain between Beams 2 and 3 is also still noticeable.

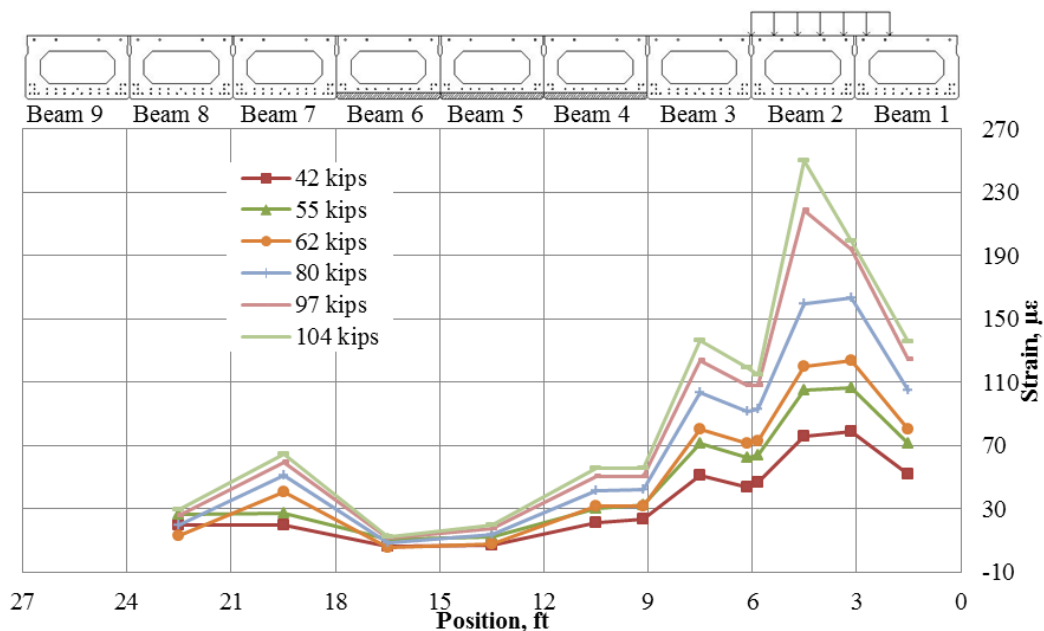


**Figure 103: Bottom Strain Profile Instrument Line A (Cylinder 3 – 100 K)**  
 (Note: 1 kip = 4.45 kN, 1' = 0.305 m)

After loading and unloading with each individual cylinder, load was applied to each cylinder and maintained as another cylinder increased load. Figures 104 and 105 show the deflection across the bridge at instrument lines A and B, respectively, as the total load from all cylinders increased. Table 11 provides how the total load was distributed from the three cylinders. When the maximum load of 367 kips (1,633 kN) was obtained the bridge was no longer able to support higher total load and deflections increased. Initially, the deflections are fairly symmetric about Beam 5. The deflection of Beam 9 begins to show less of an increase in deflection compared to all the other beams after a total load of 251 kips (1,117 kN). At the maximum load, the deflection of Beam 9 is approximately 1” (25.4 mm) less than Beam 8 and approximately 1.5” (38.1 mm) less than Beam 5. The behavior is likely due to loss of the shear key for Beam 9. Beams 4-6 show the largest deflection as the load is highest in cylinder 2. With the exception of Beam 9, the deflection is relatively uniform across the bridge even after the maximum load has been reached.

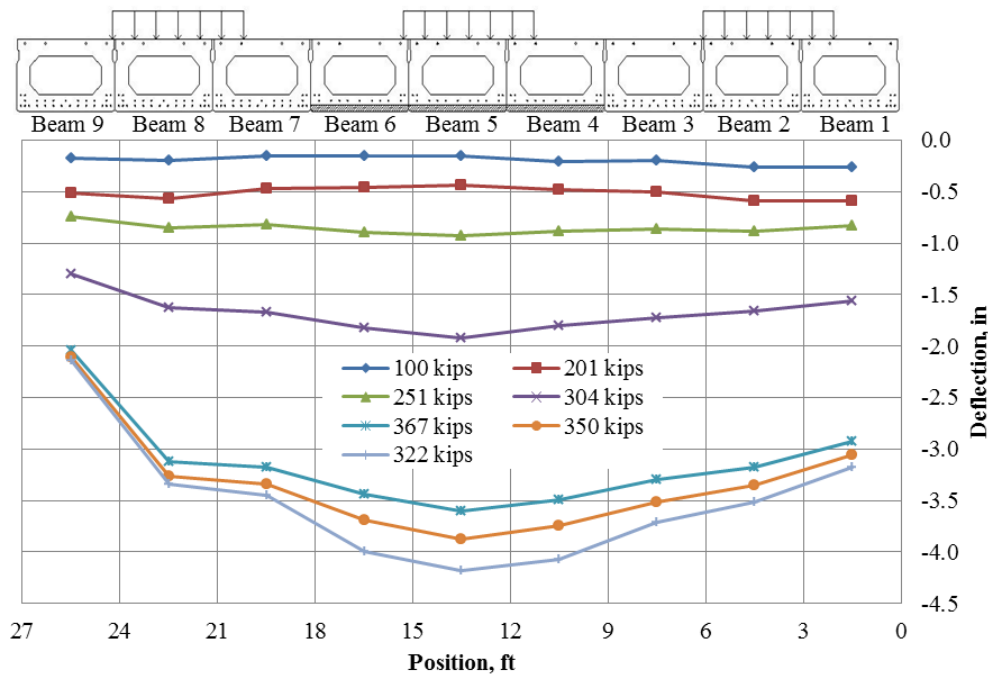


**Figure 104: Total Load and Instrument Line A Deflection (West Span)**

(Note: 1 kip = 4.45 kN, 1” = 25.4 mm)

**Table 11: Cylinder Load Distribution (West Span)**

Total Load (kips)	Cylinder Load (kips)		
	1	2	3
100	42	0	58
201	100	0	101
251	58	140	53
304	42	226	36
367	83	201	83
350	59	239	52
322	49	242	31

(Note: 1 kip = 4.45 kN)

Instrument line B had deflections that were relatively more uniform across the width of the bridge (Figure 105). This instrument line was near one of the transverse ties in the bridge and this was likely the reason for the consistency in deflections.

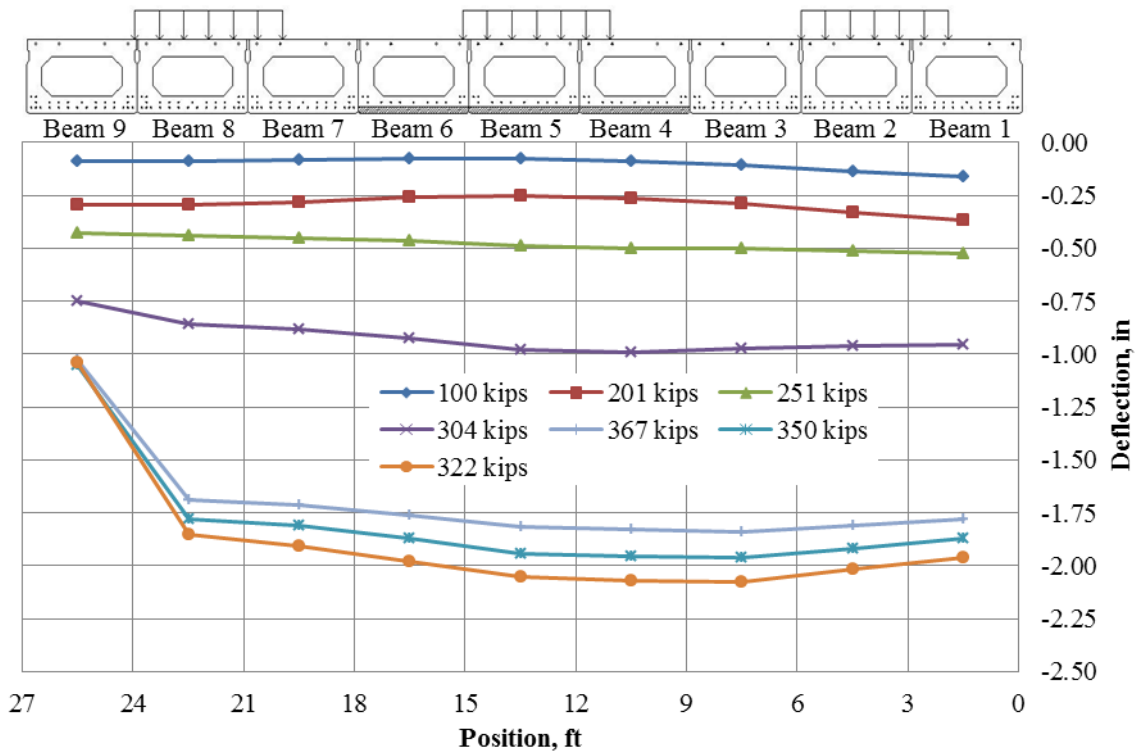


**Figure 105: Total Load and Instrument Line B Deflection (West Span)**

(Note: 1 kip = 4.45 kN, 1" = 25.4 mm)

Figure 106 shows the total load from all the cylinders versus the average deflection along instrument line A of all the beams. The figure shows a linear behavior for the bridge until the total load reaches approximately 200 kips (890 kN). The average deflection of the bridge then becomes nonlinear. After the maximum load of 363 kips (1,615 kN) is reached, the load drops off as deflection increases. The bridge was then unloaded due to reaching stroke limitations on the cylinders. Upon unloading a permanent average deflection of 1.30" (33 mm) remained.

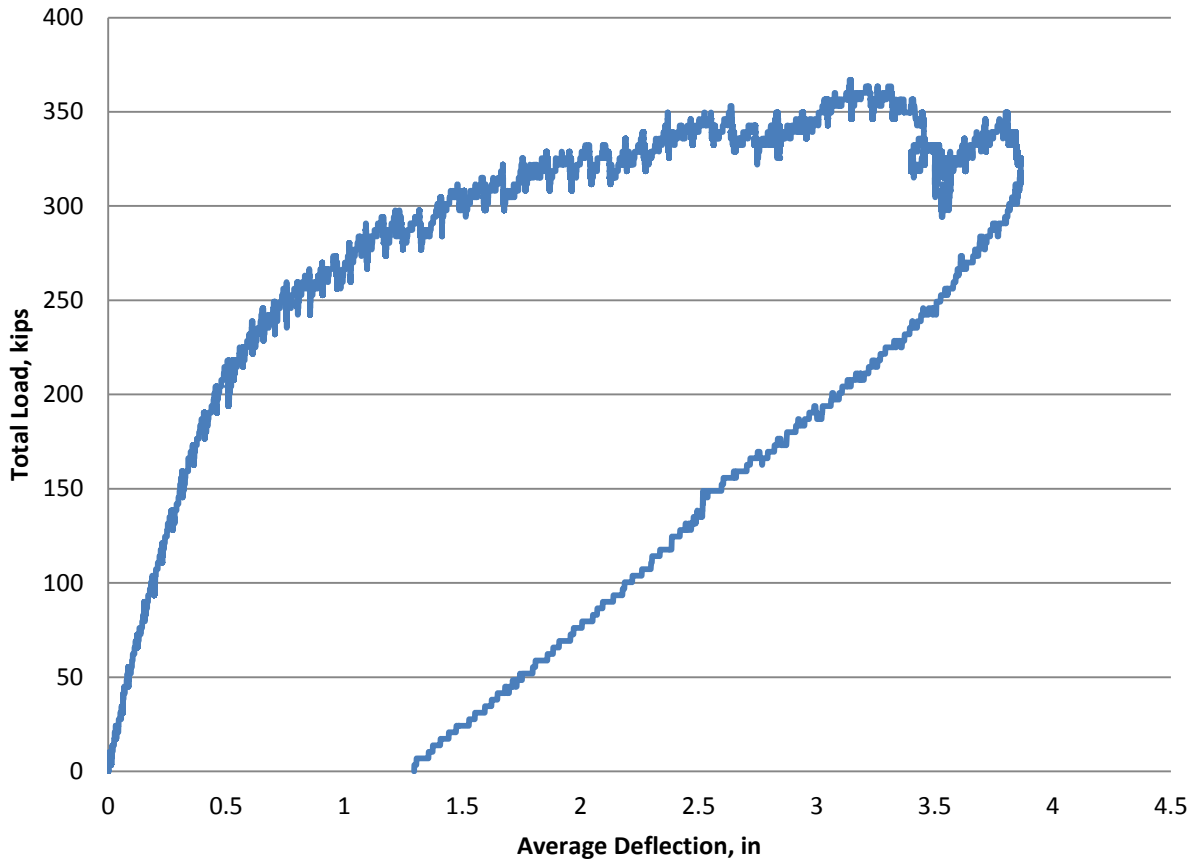


**Figure 106: Total Load and Instrument Line A Average Deflection (West Span)**

(Note: 1 kip = 4.45 kN, 1" = 25.4 mm)

After providing additional shims to allow for further deflections, the load was reapplied with the cylinders. The west span's deflection behavior along instrument line A during this loading sequence is shown in Figure 107. Notice the deflections of Beams 4-6 began to greatly exceed that of the other beams once a total load of 274 kips (1,219 kN) was achieved. The bridge was unable to maintain this load level and deflections continued to increase. The 274 kip (1,219 kN) total load did not reach the level of the total load achieved prior to shimming. In addition, load was unable to be increased in the middle cylinder loading Beams 4 and 5 but higher loads were achieved on cylinder 1 loading Beams 7 and 8. Deflections of Beams 7 and 8 increased more rapidly as well. The total loads and the load on each cylinder are provided in Table 12. Figure 108 provides the deflection behavior at instrument line B. The behavior was in general the same as along instrument line A with lower deflections. However, the deflections did not consistently increase even if the load was dropping off.

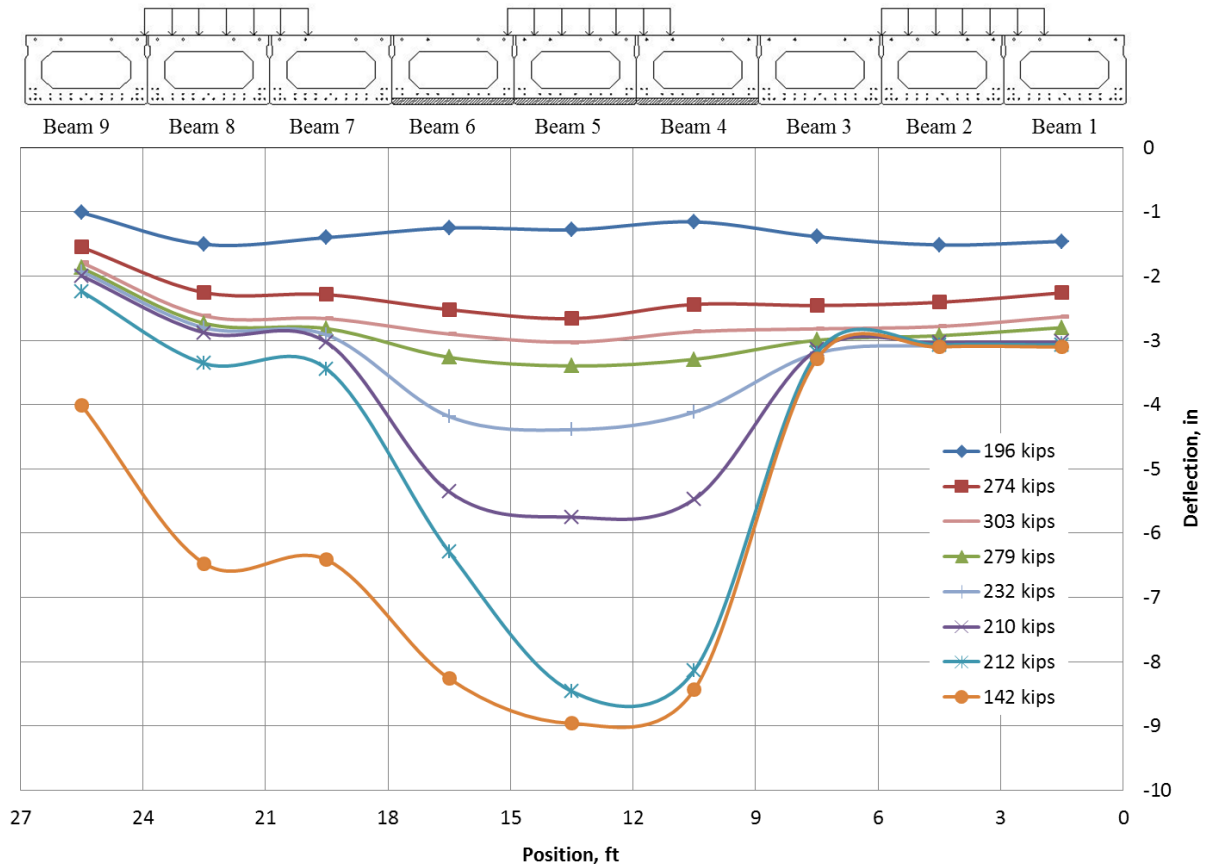
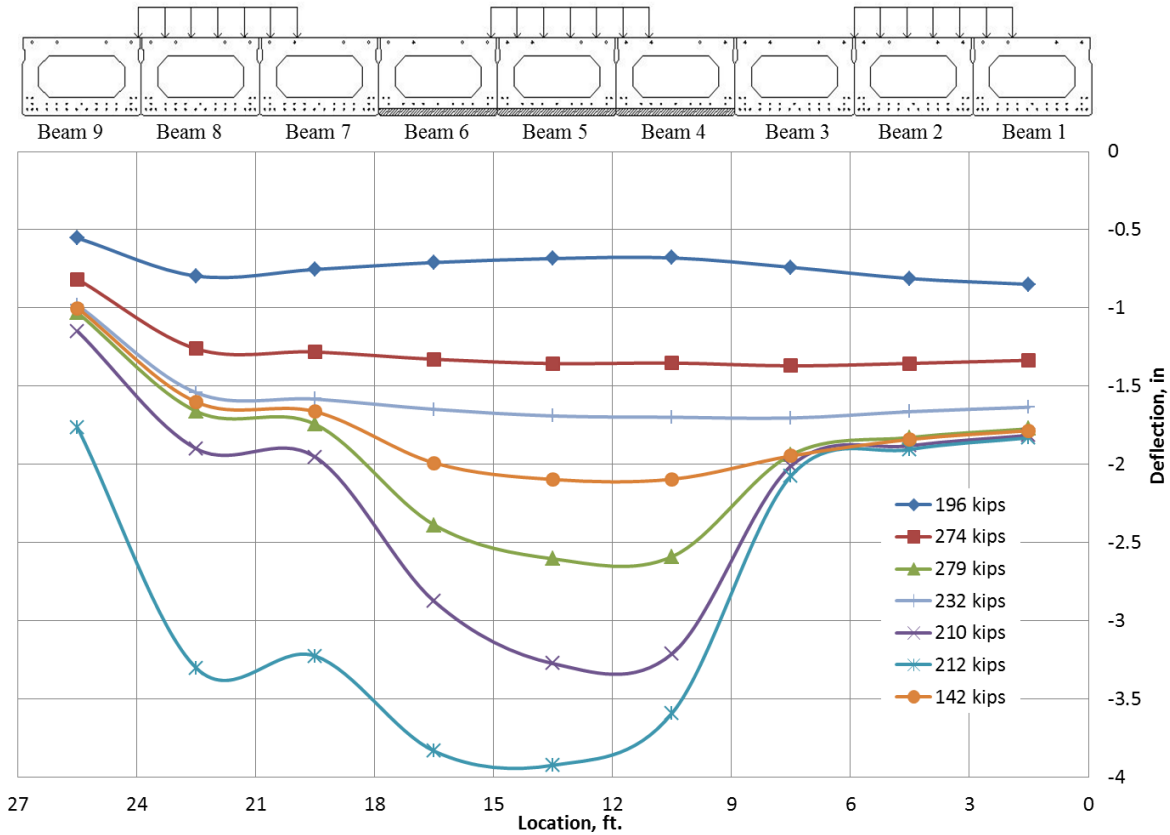


**Figure 107: Total Load and Instrument Line A Deflection after Shimming (West Span)**  
 (Note: 1 kip = 4.45 kN, 1" = 25.4 mm)

**Table 12: Cylinder Load Distribution after Shimming (West Span)**

Total Load (kips)	Cylinder Load (kips)		
	1	2	3
196	94	0	102
274	51	182	41
279	51	190	38
232	42	168	22
210	33	148	29
212	101	90	21
142	98	28	16

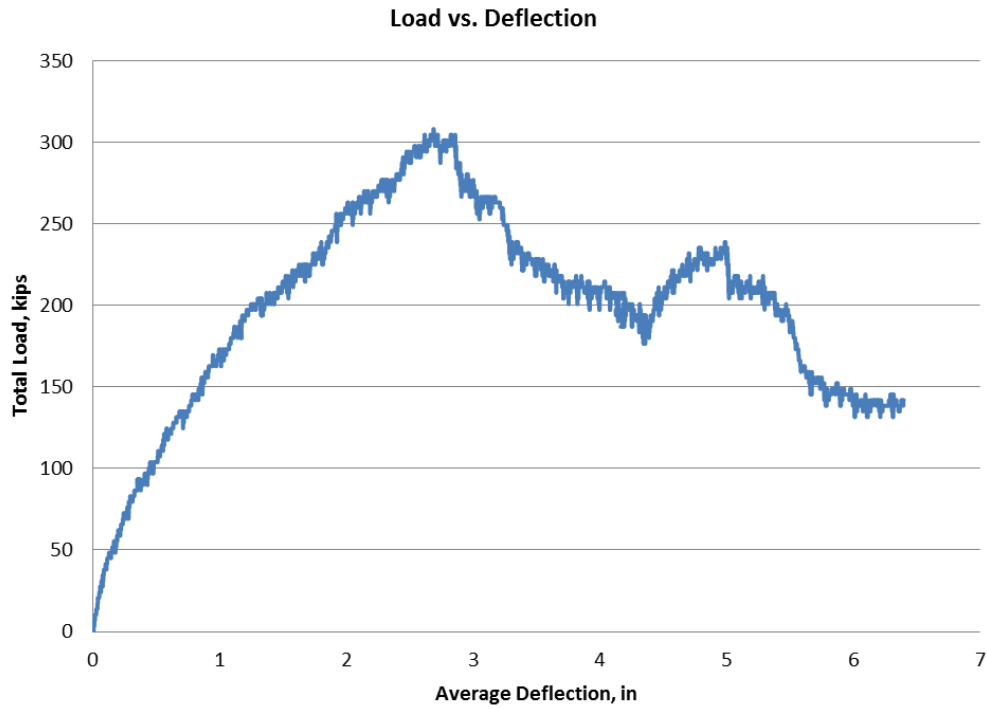
(Note: 1 kip = 4.45 kN)



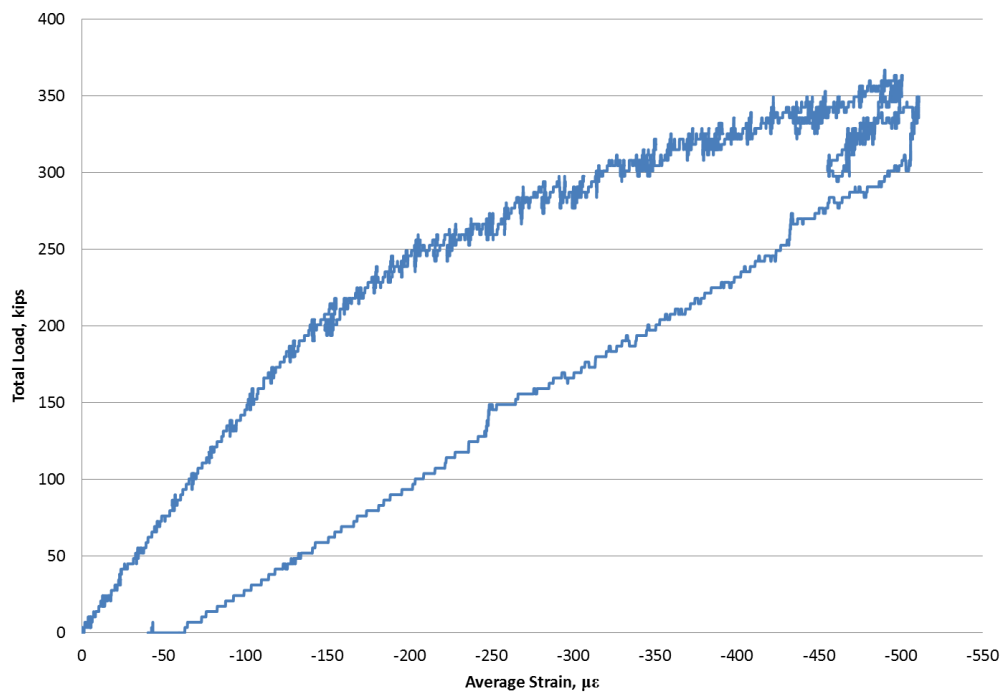
**Figure 108: Total Load and Instrument Line B Deflection after Shimming (West Span)**  
 (Note: 1 kip = 4.45 kN, 1" = 25.4 mm)

Figure 109 shows the total load from all the cylinders versus the average deflection along instrument line A of all the beams after the shimming process. The figure shows minor linear behavior to start before becoming nonlinear. A maximum load of approximately 300 kips (1,335 kN) is reached at an average deflection of nearly 3" (76.2 mm) before load decreases as the average deflection continues to increase.

The average strain across the bottom of the bridge along instrument line A versus the total applied load prior to shimming is shown in Figure 110. The average strain is relatively linear up to approximately 200 kips (890 kN). The curve then continues approximately linearly at a flatter slope until the peak load is reached.



**Figure 109: Total Load and Instrument Line A Average Deflection after Shimming (West Span)**  
 (Note: 1 kip = 4.45 kN, 1" = 25.4 mm)



**Figure 110: Average Top Strain vs. Load - Instrument Line A (All Cylinders)**  
 (Note: 1 kip = 4.45 kN)

Figures 111-113 show the west span prior to collapse. The large relative deflections shown between Beams 8 and 9 and also Beams 6 and 7 in Figures 111 and 112 imply the loss of the shear key between those beams. The shear key between Beams 3 and 4 has also failed as shown in Figure 113. However, the bridge was still able to maintain and transfer load throughout the system. This was likely due to the transverse tie rods existing between the beams as well as some shear friction between the shear keys and beams.



**Figure 111: Shear Key Failures Between Beams 8-9 and 6-7 Prior to Collapse (West Span)**



**Figure 112: Shear Key Failures Between Beams 8-9 and 6-7 Prior to Collapse (West Span)**



**Figure 113: Shear Key Failure between Beams 3 and 4 Prior to Collapse (West Span)**

Loading was stopped and the string potentiometers were removed to prevent damage. Loading was again applied to the bridge without being able to exceed the previous maximum total loading. Eventually the bridge completely collapsed in a ductile manner (see Figures 114 - 116). Beams 1-8 failed near midspan close to the loading locations and Beam 9 failed near the abutment. Beams 7 and 8 pulled sufficiently away from the pier and fell to the ground near the pier. The transverse tie between Beams 8 and 9 (see Figure 117) and Beams 6 and 7 fractured allowing Beams 7 and 8 to be separated from the remaining beams. Beam 9 had lost its top flange which was a patched section at this location. A combination of separation of the top flange, poor concrete, and shear resulted in the failure of Beam 9.



**Figure 114: Collapsed Bridge (West Span w/ Frame)**



**Figure 115: Collapsed Bridge (West Span w/o Frame)**



**Figure 116: Collapsed Bridge (West Span w/o Frame)**



**Figure 117: Fractured Transverse Bar (West Span)**

### 3.4.4 Span Comparison

In order to compare the destructive test results for the different spans, the plots of the average midspan deflection for the Center and West spans versus the total applied load was created and is provided in Figure 118. These are Figures 85 and 106 superimposed into the same figure. As can be seen in Figure 118, both spans behave in a similar linear manner up to approximately 175 kips (779 kN) even though the West span had significantly more damage. After approximately 175 kips (779 kN), the West span begins to become nonlinear as the Center span continues to be linear to approximately 225 kips (1,001 kN). At larger loading, the West span shows more average deflection. At the peak load for the West span, the average deflection is approximately twice that of the Center span. The Center span obtains the deflection of West span peak load at approximately an additional 70 kips (312 kN), 430 kips (1,914 kN) compared to 360 kips (1,602 kN).

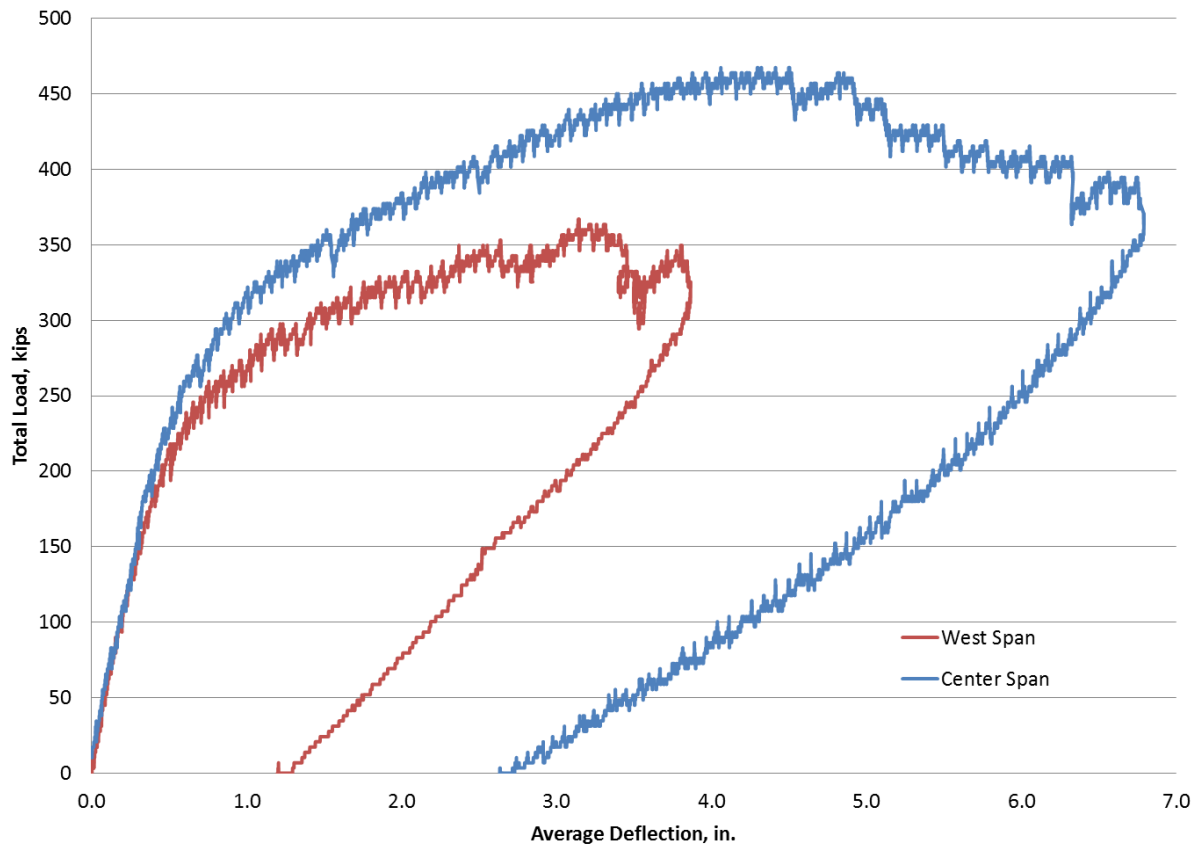


**Figure 118: Average Mid-span Deflections vs. Load (Center & West Spans)**  
(Note: 1 kip = 4.45 kN, 1" = 25.4 mm)

In order to compare the destructive test results for the East and West spans, the plots of the average midspan top strain versus the total applied load was created and is provided in Figure 119. These are Figures 66 and 110 superimposed. As can be seen in Figure 119, both spans show initial linear behavior with the East span being slightly stiffer than the West span. The slope of both curves then change to another approximately linear portion with the East span again being stiffer than the West span. The change in stiffnesses occur at approximately 260 kips (1,157 kN) for the East span and approximately 225 kips (1,001 kN) for the West span. These differences can be attributed to the more severe damage in the West span compared to the East span.

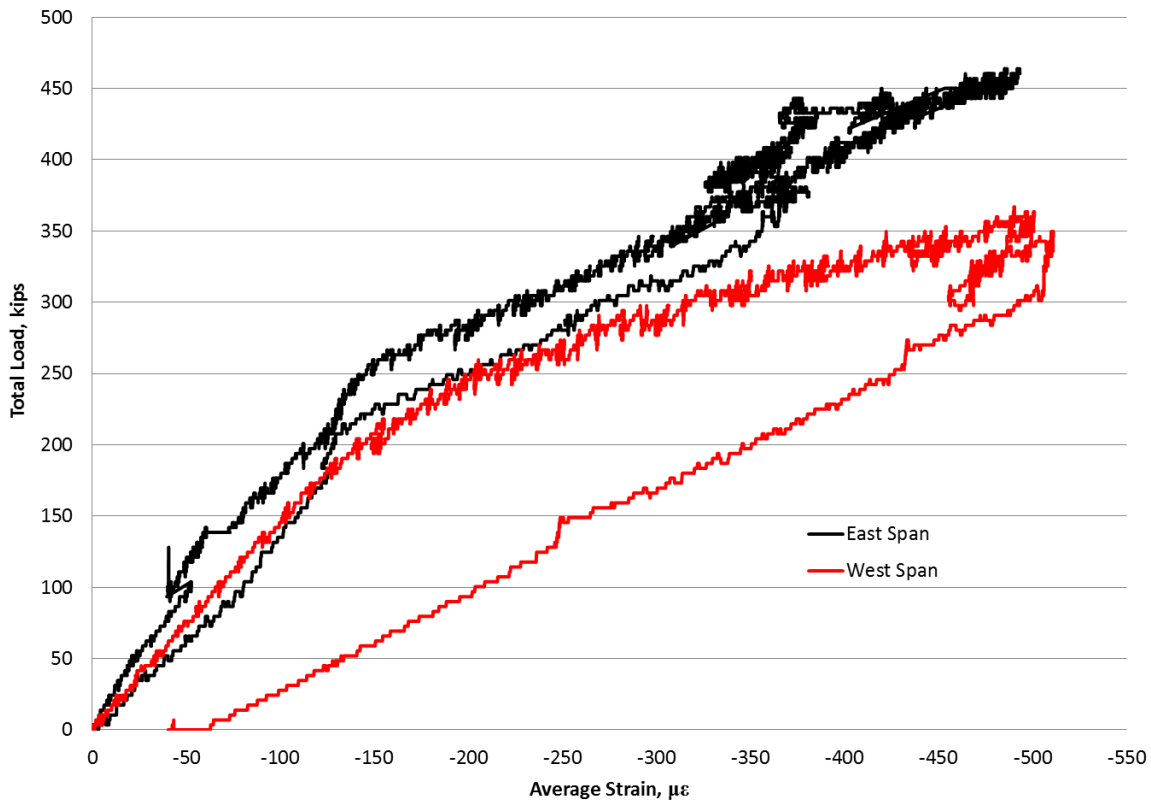


**Figure 119: Average Mid-span Strain vs. Load (East & West Spans)**  
 (Note: 1 kip = 4.45 kN)

## 4. ANALYSIS

### 4.1 AASHTO Standard Capacities

For comparisons and to allow for both rating procedures to be used, the moment capacities of undamaged and damaged beams were determined using the AASHTO Standard Bridge Design Specifications. The AASHTO capacities using the Standard Specifications for each beam are provided in Table 13. The capacities were determined using the average compressive strength of the concrete cores. The live load capacity was determined by taking the total moment capacity and subtracting out the moments due to self-weight and the asphalt wearing surface. Resistance and load factors were not utilized in order to compare the results to experimental findings. The maximum live load is the maximum concentrated load that the beam could support at midspan assuming the bridge to behave as a simply supported span. This was also done in order to compare the calculated results with the experimental results.

The last column of Table 13 shows the maximum live load that could be applied to the bridge if the typical distribution factor method was used. This was determined by taking the live load capacity of the beam and dividing it by the distribution factor.

**Table 13: AASHTO Standard Specifications Beam Capacity**

Strands Cut (27 Total)	Total Moment Capacity (k-ft)	Live Load Moment Capacity (k-ft)	Maximum Live Load (k)	Maximum Live Load (k) (Dist. Factor)
0	744	508	43	168
3	669	433	36	143
6	592	356	30	117
14	378	142	12	47

(Note: 1 kip = 4.45 kN, 1 ft. = 0.305 m)

Another procedure to estimate the total load capacity of the entire bridge was to determine the summation of the individual beam capacities. Each span had a various number of undamaged and damaged beams to different magnitudes. The East Span had 3 beams with 3 strands cut (Beam 9 actually had 3 strands exposed and severely corroded prior to any testing), 2 beams with 6 strands cut, and the remaining 4 beams had no strands cut. The Center Span had no strands cut on any of the beams. The West span had 14 strands cut on 3 beams. Based on these damage levels, the total capacity of the bridge for each span is shown in Table 14. In addition, the Table provides the total capacity of the bridge determined from the experimental results. The last column of Table 14 provides the percentage difference in the analytical and experimental results.

**Table 14: AASHTO Standard and Experimental Bridge Capacity**

Bridge Span	AASHTO Capacity (kips)	Experimental Capacity (kips)	Percent Difference
East	345	464	+34
Center	383	467	+22
West	291	367	+26

(Note: 1 kip = 4.45 kN)

## 4.2 AASHTO LRFD Capacities

Using the AASHTO LRFD Bridge Design Manual, the moment capacities of undamaged and damaged beams were determined. The AASHTO LRFD capacities for each beam are provided in Table 15. The concrete compressive strength determined from the concrete cores was used in the analyses. The damaged beams accounted for the varying number of strands cut in the spans. The live load capacity was determined by taking the total moment capacity and subtracting out the moments due to self-weight and the asphalt wearing surface. Resistance and load factors were not utilized in order to compare the results to experimental findings. The maximum live load is the maximum concentrated load that the beam could support at midspan assuming the bridge to behave as a simply supported span. This was also done in order to compare the calculated results with the experimental results.

The last column of Table 15 shows the maximum live load that could be applied to the bridge if the typical distribution factor method was used. This was determined by taking the live load capacity of the beam and dividing it by the distribution factor for the interior beam. The interior beam was used even though this distribution factor was slightly less than that for the exterior beam. This was done due to the damage and loading occurring on the interior beams.

**Table 15: AASHTO LRFD Beam Capacity**

Strands Cut (27 Total)	Total Moment Capacity (k-ft)	Live Load Moment Capacity (k-ft)	Maximum Live Load (k)	Maximum Live Load (k) (Dist. Factor)
0	742	507	42	167
3	667	432	36	142
6	591	355	30	117
14	377	141	12	47

(Note: 1 kip = 4.45 kN, 1 ft. = 0.305 m)

Another procedure to estimate the total load capacity of the entire bridge was to determine the summation of the individual beam capacities. Each span had a various number of undamaged and damaged beams to different magnitudes. For the East span, Beams 3 and 5 had 6 strands cut and Beams 2 and 6 had 3 strands cut. Beam 9 on East Span also had 3 strands exposed and severely corroded prior to physically causing damage to the span. The remaining 4 beams had no strands cut. The Center Span had no strands cut on any of the beams. The West span had 14 strands cut on Beams 4-6 and the remaining beams did not have any strands cut. Based on these damage levels, the total capacity of the bridge for each span is shown in Table 16. In addition, the table provides the total capacity of the bridge determined from the experimental results. The last column of Table 16 provides the percentage difference in the analytical and experimental results.

**Table 16: AASHTO LRFD and Experimental Bridge Capacity**

Bridge Span	AASHTO Capacity (kips)	Experimental Capacity (kips)	Percent Difference
East	344	464	+35
Center	382	467	+22
West	290	367	+27

(Note: 1 kip = 4.45 kN)

### 4.3 Load Factor Rating (LFR)

In order to rate the bridge using the LFR procedure, the flexural capacities determined in section 4.1 were utilized. The LFR results are provided in Table 17 for each damage level to the beams within the bridge assuming a simply supported span. Live load distribution factors were determined using standard AASHTO procedures. The legal load was controlled by the 4F1 truck in all cases.

In addition to the rating based on a single beam, the rating for the entire bridge capacity was also determined and is shown in the last two rows of Table 17. Only the west span was determined since this was the span with the most severe damage. The total capacity of the bridge was taken from Table 14 for either for the analytically or experimentally determined case.

**Table 17: LFR Rating Factors (Simply Supported)**

Beam	Strands Cut (27 Total)	Design Load Rating (HS20-44)		Legal Load Rating (4F1 Controls)
		Inventory Level	Operating Level	
Exterior and Interior	0	1.05	1.75	2.04
	3	0.87	1.45	1.69
	6	0.68	1.14	1.33
	14	0.17	0.28	0.33
Bridge (West Span)	Analytical	0.86	1.44	1.67
	Experimental	1.33	2.22	2.58

Based on the results shown in Table 17, the rating of the bridge based on the west span after the damage that was induced would be 0.33 which would require posting. However, the rating would increase to 1.67 if the entire capacity of the bridge was considered instead of a single damaged beam. The rating increases to 2.58 if the actual experimental test capacity of the bridge is utilized instead of the analytically determined capacity. Both cases result in no posting.

The analysis for the LFR method made several assumptions. The first assumption was that the bridge behaved as a simply supported span. This was proven from experimental results not to be the case even after cutting continuity steel. To account for this assumption, the LFR method was repeated assuming a continuous span for live load only. The LFR results from assuming the continuous span are shown in Table 18. As expected the ratings for the continuous case increase due to the lower moment associated with the live load. However, these ratings do not take into consideration any negative moment capacity of the bridge over the pier.

**Table 18: LFR Rating Factors (Continuous for Live Load)**

Beam	Strands Cut (27 Total)	Design Load Rating (HS20-44)		Legal Load Rating (4F1 Controls)
		Inventory Level	Operating Level	
Exterior and Interior	0	1.33	2.23	2.55
	3	1.10	1.84	2.11
	6	0.87	1.45	1.66
	14	0.22	0.36	0.41
Bridge (West Span)	Analytical	1.10	1.83	2.10
	Experimental	1.69	2.83	3.24

Another assumption made during the LFR analysis was that the loads distributed between beams based on the live load distribution factor from the Standard Specifications. This assumes the bridge members to be in an original condition and of the same stiffness. This does not affect the rating based on the entire bridge capacity, but it does affect the rating if it is based on an individual beam.

The assumption of rating the entire bridge compared to an individual beams relies on the bridge behaving as a system throughout loading. This is primarily dependent on the shear keys and the transverse tie rods. As seen in the destructive tests that even when the shear keys appeared to no longer be effective based on large relative deflections between beams, the transverse ties were able to keep the bridge acting as a system.

#### 4.4 Load and Resistance Factor Rating (LRFR)

In order to rate the bridge using the LRFR procedure, the flexural capacities determined in section 4.2 were utilized. To perform the rating, the following additional assumptions were necessary. The condition factor,  $\phi_c$ , was taken as 0.95 which corresponds to a “fair” condition. The system factor,  $\phi_s$ , was taken as 1.00 which corresponds to “all other girder bridges and slab bridges”. The LRFR results are provided in Table 19 for each damage level to the beams within the bridge assuming a simply supported span. Live load distribution factors were determined using standard AASHTO procedures. Since there are different distribution factors for the exterior and interior beams, the results from both are provided in the Table. The legal load was controlled by the 4F1 truck in all cases.

In addition to the rating based on a single beam, the rating for the entire bridge capacity was also determined and is shown in the last two rows of Table 19. Only the west span was determined since this was the span with the most severe damage. The total capacity of the bridge was taken from Table 16 for either for the analytically or experimentally determined case.

Based on the results shown in Table 19, the rating of the bridge based on the west span after the damage that was induced would be 0.20 which would require posting of the bridge. However, the rating would increase to 1.25 if the entire capacity of the bridge was considered instead of a single damaged beam. The rating increases to 2.41 if the actual experimental test

capacity of the bridge is utilized instead of the analytically determined capacity. Utilizing the total bridge capacity whether analytical or experimental, does not result in posting be required.

**Table 19: LRFR Results (Simply Supported)**

Beam	Strands Cut (27 Total)	Design Load Rating (HL-93)		Legal Load Rating (4F1 Controls)
		Inventory Level	Operating Level	
Exterior	0	0.94	1.21	1.54
	3	0.77	0.99	1.26
	6	0.60	0.77	0.98
	14	0.12	0.15	0.19
Interior	0	0.98	1.27	1.61
	3	0.80	1.04	1.32
	6	0.62	0.81	1.03
	14	0.12	0.16	0.20
Bridge (West Span)	Analytical	0.76	0.98	1.25
	Experimental	1.31	1.70	2.41

As with the LFR method, the analysis for the LRFR method made the first assumption that the bridge behaved as a simply supported span. To account for this assumption, the LRFR method was repeated assuming a continuous span for live load only. The LRFR results from assuming the continuous span are shown in Table 20. The ratings for the continuous case increase compared to the simply supported case. However, the ratings do not account for the negative moment capacity of the bridge over the pier.

**Table 20: LRFR Rating Factors (Continuous for Live Load)**

Beam	Strands Cut (27 Total)	Design Load Rating (HL-93)		Legal Load Rating (4F1 Controls)
		Inventory Level	Operating Level	
Exterior	0	1.17	1.52	1.93
	3	0.96	1.25	1.58
	6	0.75	0.97	1.23
	14	0.15	0.19	0.24
Interior	0	1.23	1.60	2.02
	3	1.01	1.31	1.66
	6	0.78	1.02	1.29
	14	0.15	0.20	0.25
Bridge (West Span)	Analytical	0.95	1.23	1.56
	Experimental	1.64	2.13	2.70

The LRFR analysis utilized the live load distribution factor from the LRFD Bridge Design Specifications. This assumes the bridge members to be in an original condition and of the same stiffness. This does not affect the rating based on the entire bridge capacity, but it does affect the rating if it is based on an individual beam.

The assumption of rating the entire bridge compared to an individual beams relies on the bridge behaving as a system throughout loading. This is primarily dependent on the shear keys and the transverse tie rods. As seen in the destructive tests that even when the shear keys appeared to no longer be effective based on large relative deflections between beams, the transverse ties were able to keep the bridge acting as a system.

#### 4.5 Distribution Factors

The distribution factors for the tested spans were determined for comparison with those determined by AASHTO methods. The factors were found by dividing the mid-span tensile strain in a beam by the total mid-span tensile strains of all the beams. The tensile strains from the beams were used since strain gages existed on the bottom of all spans across the full width of the bridge. In addition, the tensile strains were more consistent. However, this was only true at lower loading and when only loading from a single cylinder was applied. The distribution factors found from the testing are shown in Table 21. The largest distribution factor is shown in the Table since this is the one that would be used in design and comparable to that determined by AASHTO procedures. The values shown in Table 21 are close to the ones determined from LRFD for use in LRFR (0.242 for interior and 0.254 for exterior). The value determined from the Standard Specification for use in LFR (0.49) is much higher than the distribution factors shown in Table 21. Table 21 also shows the distribution factor is largest for the beam nearest the applied loading with the exception of the West span where Beam 7 had the largest DF when cylinder 2 was loaded. This was due to the significant damage induced into Beams 4-6. It should also be noted that the values in Table 21 were found at relatively low loads compared to ultimate loads where the distribution factor is used in design.

**Table 21: Experimental Distribution Factors**

Span	Loaded Cylinder	Beam	Distribution Factor
East	1	8	0.31
	2	5	0.20
	3	2	0.29
Center	1	8	0.27
	2	5	0.17
	3	2	0.24
West	1	8	0.31
	2	7	0.21
	3	2	0.36

## 4.6 Beam Modeling

To further understand the behavior of the spans, a model was developed to analyze the beam behavior using the computer program Response 2000. This software was utilized in the first phase of the project and predicted the behavior of individual beams well. The difficulty in using this program for this aspect of the project was determining the actual load being applied to individual beams as opposed to the entire bridge. Therefore, the distribution factors developed from the strain data was used to estimate the load carried by individual beams. Figure 120 shows the results of the Response models assuming simple and fixed support conditions for Beam 7 of the Center span when cylinder 3 was loaded to 100 kips (445 kN). The experimental results are for the total load from cylinder 3 multiplied by the distribution factor for the beam based on strains. The majority of the beams analyzed were typical of Figure 120. The experimental results showed a stiffer response than the simple and fixed Response models. However in some instances (see Figure 121), the experimental responses fell in between the simple and fixed support Response models. The differences of the models compared to the experimental results are the result of either the distribution factors and/or the models are conservative.

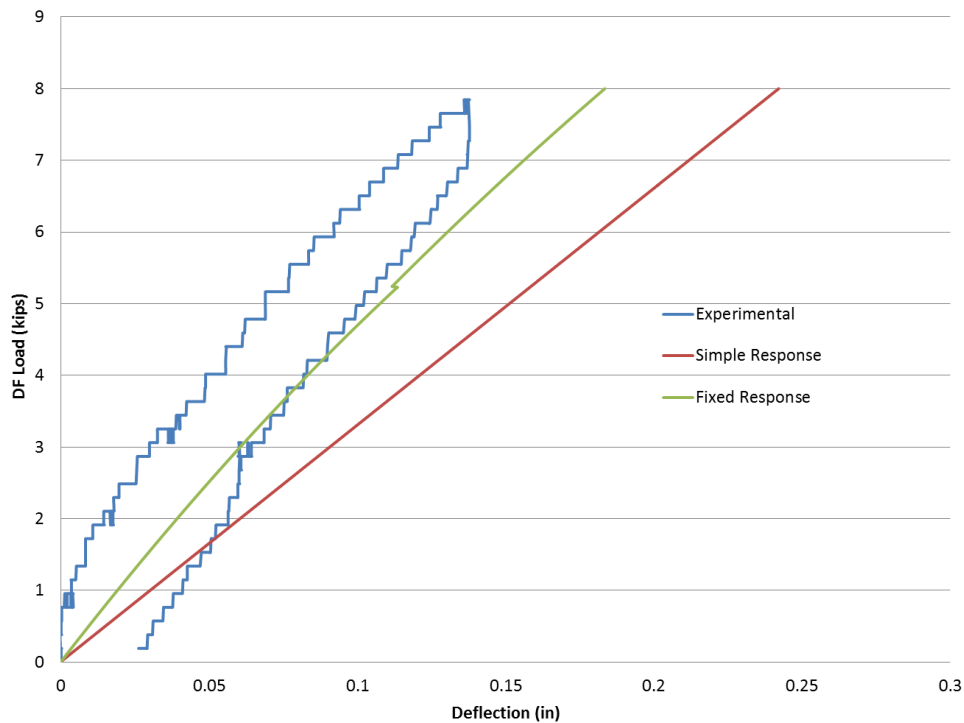


**Figure 120: Center Span Beam 7 (100 kip Cylinder 3)**

(Note: 1 kip = 4.45 kN, 1" = 25.4 mm)

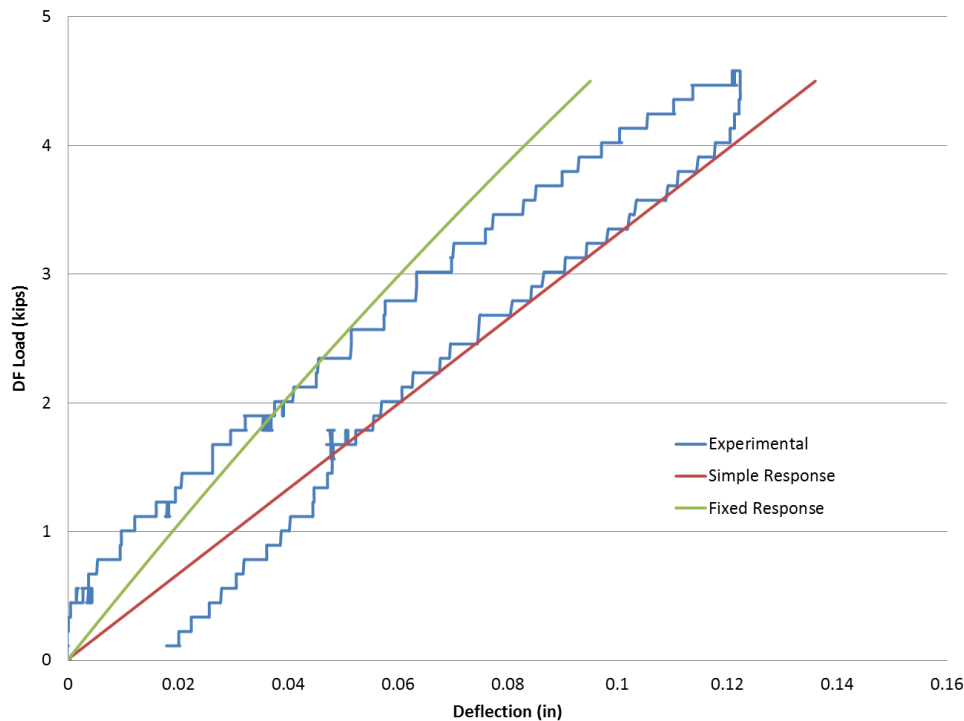


**Figure 121: Center Span Beam 8 (100 kip Cylinder 3)**  
 (Note: 1 kip = 4.45 kN, 1" = 25.4 mm)

## 4.7 Finite Element Modeling

A finite element model was used to model the damaged west span of the bridge. A standard model was constructed in Abaqus/CAE 6.10. The prestressed concrete box beams were modeled using a smeared cracking method with the reinforcement modeled as embedded steel elements. Modeling the concrete using a smeared cracking method is the predominate approach used in three-dimensional modeling of concrete (Barzegar & Maddipudi, 1997). The model of the damaged bridge span consists of nine beams with longitudinal reinforcement, eight shear keys, springs to model the transverse ties and dowel rods, applied loads at the location of cylinders, and boundary conditions that represent the abutment and pier.

The cross-sections of the precast concrete box beams, prestressed reinforcement, conventional reinforcement, and shear keys of the west span of bridge were drawn in the Abaqus/CAE to the specifications provided in the bridge design drawings. Once the cross-sections were drawn, the parts were extruded 47' 10" (14.6 m) in the positive Z direction.

Each part was meshed independently, the cross-section of the beam was seeded to yield an approximate mesh resolution of three inches, and the beam was also seeded along its length every six inches. A three inch seed was required on the beam cross-section to ensure the mesh shape was within the set angle constraints. The beam was then meshed using a sweep mesh control, creating 7,296 elements for each beam. The cross-section of the shear key was seeded with a 0.75 inch (19 mm) seed to meet the angle limits of the element shape. The shear key was similarly seeded with a six inch seed along the length of the part. The shear key was meshed using a sweep mesh control, and 2,304 elements were created for each shear key. The steel reinforcement cross-section was also seeded with a two inch seed to meet the angular limit of the

element shape, to maintain consistency the reinforcement was also seeded with a six inch seed along the length of the part. This allowed the nodes of the reinforcement elements to be accurately embedded into the concrete beam. Embedment is discussed in greater detail in the interaction section. The steel was also meshed using a sweep mesh control and 7,872 elements were created for each set of reinforcement. An illustration of the mesh resolution of one of the box beams can be seen below in Figure 122.

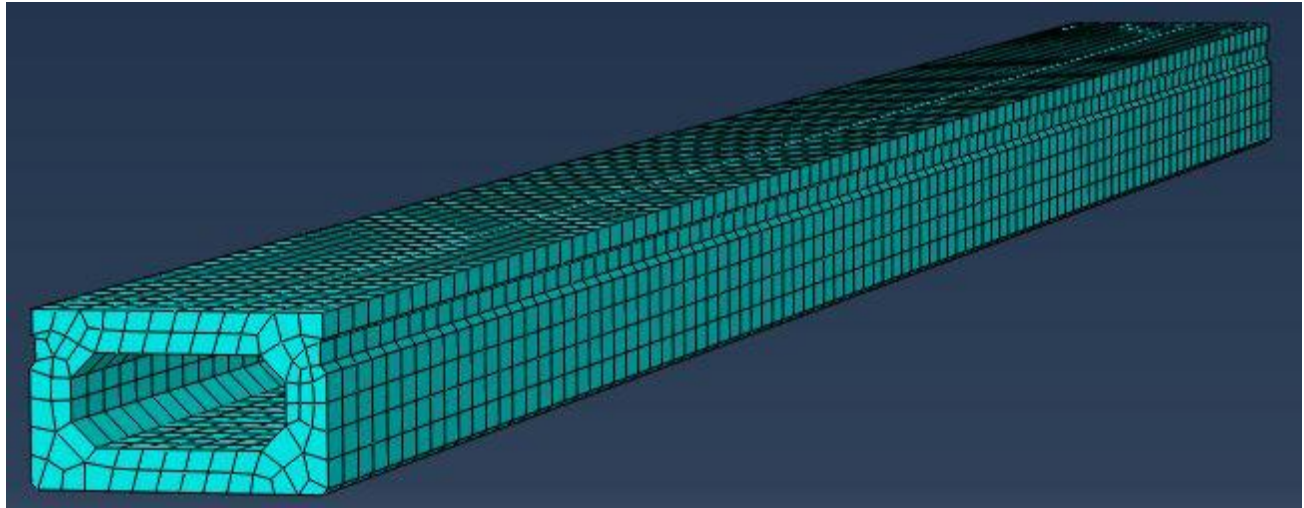


**Figure 122: Meshed Beam**

The elastic concrete material properties were modeled by defining the Young's modulus and Poisson's ratio from the concrete cores. This data included a concrete strength of 10 ksi (68.9 MPa), a Poisson's ratio of 0.2, and a unit weight of 147pcf (2,145 N/m<sup>2</sup>). The plastic concrete material properties were defined using a concrete smeared cracking model. To define the concrete smeared cracking material properties post-yield compressive and tensile stress-strain relations were defined, as were failure ratios for the concrete. The prestressed and conventional reinforcement material properties were defined the using the same material properties, the reinforcement was modeled as an elastic steel material with a Young's modulus of 29,000 ksi (200 GPa), and a Poisson's ratio of 0.3.

The damage was modeled on beams 4, 5, and 6 by taking a three inch (76 mm) long cross-section from the beams at the location of the damage and replacing the concrete smeared cracking material properties with an elastic material that has a relatively low Young's modulus and a high Poisson's ratio. Also the bottom 14 prestressing strands were removed between the locations where the cuts were made on the actual bridge. This removed approximately three feet from the bottom row of reinforcement at the center of beams 4, 5, and 6. Three feet was removed from the reinforcement to model the decreased tensile capacity of the damage sections. The material in the damaged sections models the formation of a plastic hinge when the load is applied to the bridge model. Manipulating these damaged sections allowed the strain discontinuity between the damaged and undamaged beams to be accurately modeled.

The interaction between the concrete beam and the reinforcement was modeled as an embedment constraint. Embedding the elements of the reinforcement in the concrete elements is a computational effective method to accurately model the effect of the reinforcement on the

surrounding concrete elements (Barzegar & Maddipudi, 1997). The embedment constraint embeds a group of user defined non-host elements into a group of user defined host elements. The sets of steel reinforcement were defined as non-host element and the individual beams were defined as the host elements. When a group of non-host elements is embedded in a group of host elements the translational degrees of freedom of the non-host elements are taken away where the nodes of the non-host elements coincide with the nodes of the host elements. The translations at each degree of freedom of nodes of the host elements are then placed on the nodes of non-host elements. This particular embedment type is solid element embedded into solid element. This will result in a more accurate modeling of the concrete-reinforcement interaction as opposed to modeling the reinforcement as shell or membrane elements. However, using shell or membrane elements is more computational economical.

The interaction between the concrete beams and the shear keys was modeled using a surface to surface contact. First the surfaces of the shear keys and beams that come into contact were defined as contact pairs. Both the tangential and normal behavior of the contact properties were defined. The friction formulation was defined in the tangential behavior. The type of friction formulation used was "Penalty". With the "Penalty" friction formulation, the friction coefficient for the interaction was input as 0.6 (MacGregor & Wight, 2005), the shear stress limit was set at 1.0 ksi (6.89 MPa), and the maximum elastic slip was define as 1% of the characteristic surface dimension. The pressure-overclosure in the normal behavior was selected to be linear and the contact stiffness on the interaction was defined as 50 ksi (345 Mpa). The contact stiffness restrains the nodes of the two contacting surfaces from penetration into one another.

In the damaged bridge span model, surface nodes which lied on the top surface of the beams within the location of the cylinder loadings were defined in sets for each of the three cylinder locations. For the cylinder 1 loading condition, 51 nodes were defined as the Cylinder 1 set. Similarly for the cylinder 2 and cylinder 3 loading conditions, 57 nodes were defined in sets for each of the Cylinder 2 and Cylinder 3 node sets. Defining node sets at the locations of the actual cylinder locations allows for accurate modeling of the behavior of the load applied in the destructive testing of the bridge span. Once the sets were defined, the desired magnitude of load to be applied to the model was divided by the number of nodes for that cylinder node set and concentrated point loads were applied at each node of the node set in the negative Y direction. Figure 123 shows the load applied at the node sets for all of the cylinders.

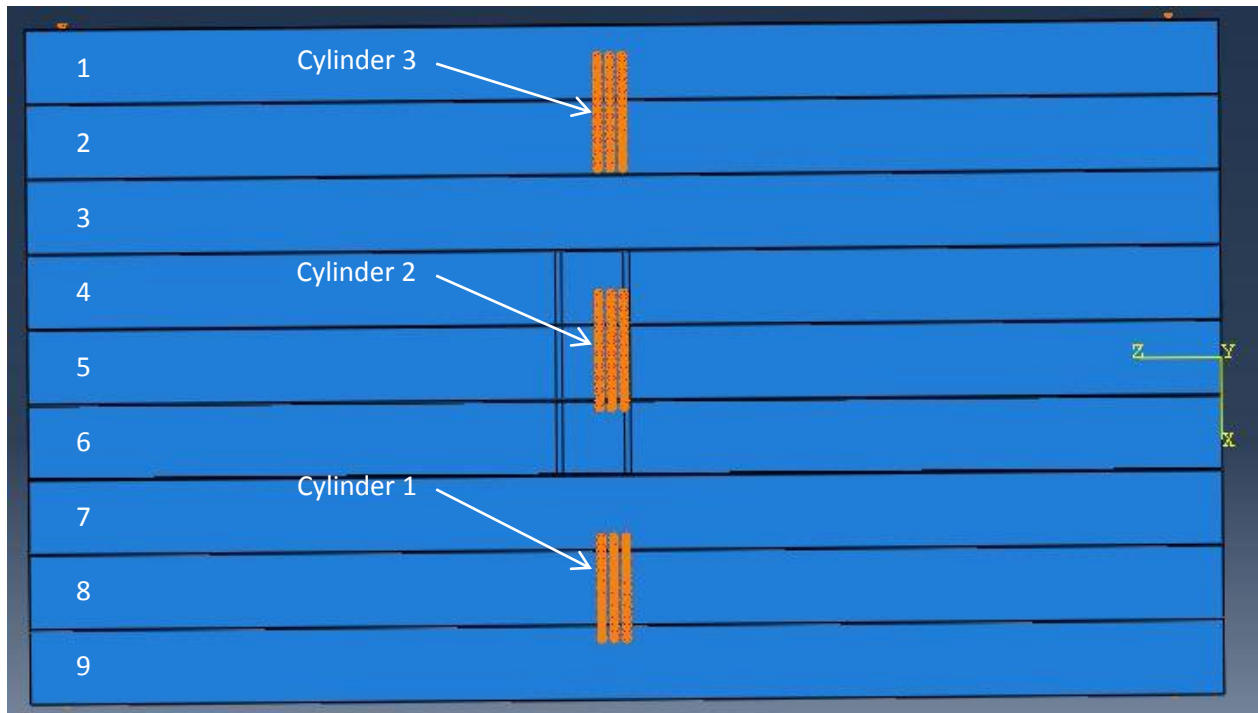


**Figure 123: User Defined Node Sets for Load Locations**

To model the abutment and pier of the damaged bridge span, a combination of support conditions and springs were used. For the abutment, a node set was defined on the bottom surface 24" (610 mm) from the end of the beam and contained seven equally spaced nodes per beam. Translational restraints were defined for these nodes in the X and Y directions. The purpose of these restraints was to model where the beam would pivot on the edge of the abutment. The actual edge of the abutment is 21" (533 mm) from the end of the beam according to the bridge design drawings, however due to the mesh resolution of six inches along the length of the beams 24" (610 mm) was used. Also there were dowel bars that connect the abutment to the beams, node sets were defined at the bottom surface of each beam approximately at the location of the dowel rods. At these node sets, springs were used to connect the nodes in the node sets to a theoretically fixed surface. The springs are defined to resist translation in the Y and Z directions. The stiffness of the springs was assigned individually for each beam to allow for differences in the influence of the dowel bars on each beam. The pier was modeled similar to the abutment. However, the location of the node set for the translational restraints was located 18" (457 mm) from the opposite end of the beam. Again the mesh resolution inhibited the restraints to be placed at the exact location of the edge of the pier specified in the bridge design drawings which was 17" (432 mm). The pier also contained dowel bars that connected the pier to the beams. The dowel bars on the pier side of the span were model using springs in the same way as dowel bars for the abutment.

The transverse ties were modeled in the damaged bridge span by a combination of concentrated loads and springs. The adjacent nodes of adjacent beams at the location of the transverse ties were tied together using springs. This spring caused the translation in the X, Y, and Z directions of one node to be transfer to the adjacent node on the adjacent beam. Also concentrated loads were placed on the nodes in positive and/or negative X direction. This load

allowed for the development of a normal force required for the tangential behavior in the interaction between the shear keys and beams.

The results of the finite element modeling compared to the experimental deflections along instrument line A are shown in Figures 124-126. Figure 124 provides the data when cylinder 1 was loaded to 52 kips (231 kN). Figure 125 compares the experimental results to the modeling data when cylinder 2 is loaded to 73 kips (325 kN). The results when cylinder 3 is loaded to 62 kips (276 kN) is provided in Figure 126. Overall the finite element model agrees well with experimental results. There are differences in the magnitude of the deflections but that is likely due to differences in the model properties and the actual bridge member properties that could vary throughout the actual bridge.

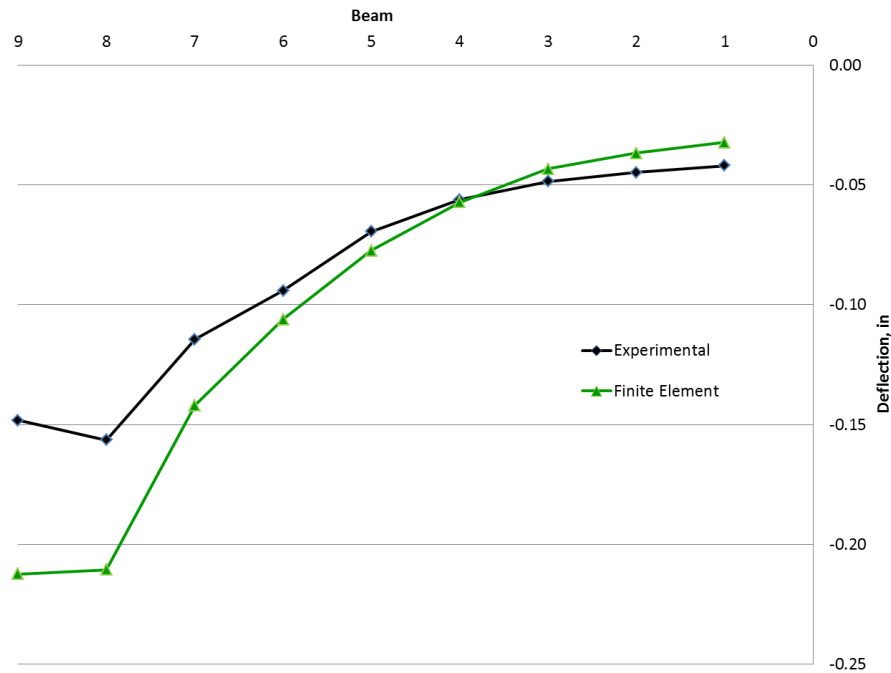


**Figure 124: FEM and Experimental Deflections Cylinder 1 (West Span)**  
 (Note: 1" = 25.4 mm)

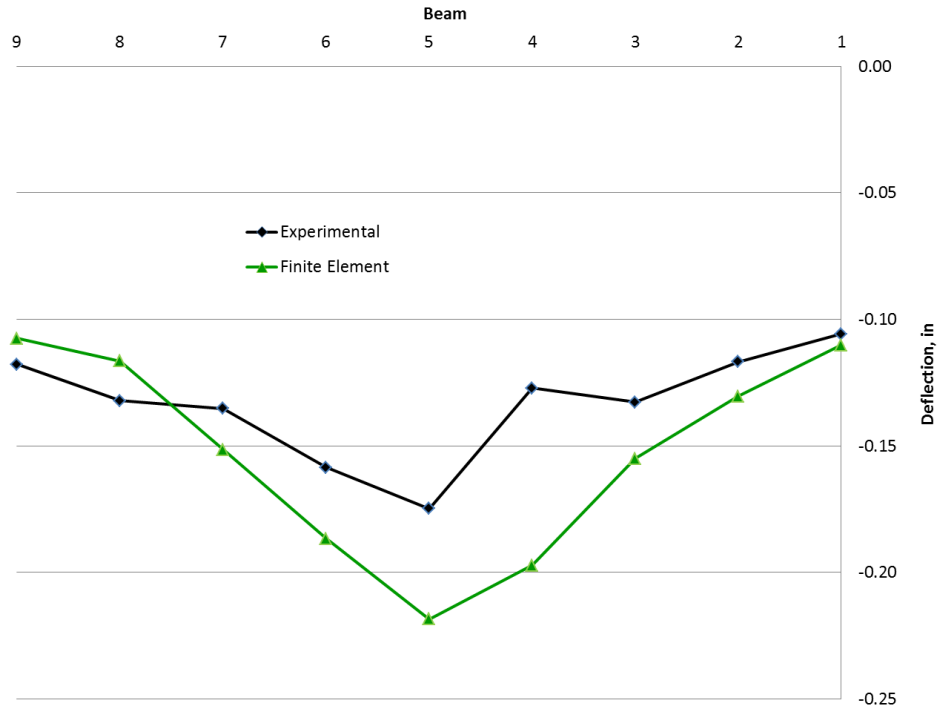


**Figure 125: FEM and Experimental Deflections Cylinder 2 (West Span)**  
 (Note: 1" = 25.4 mm)

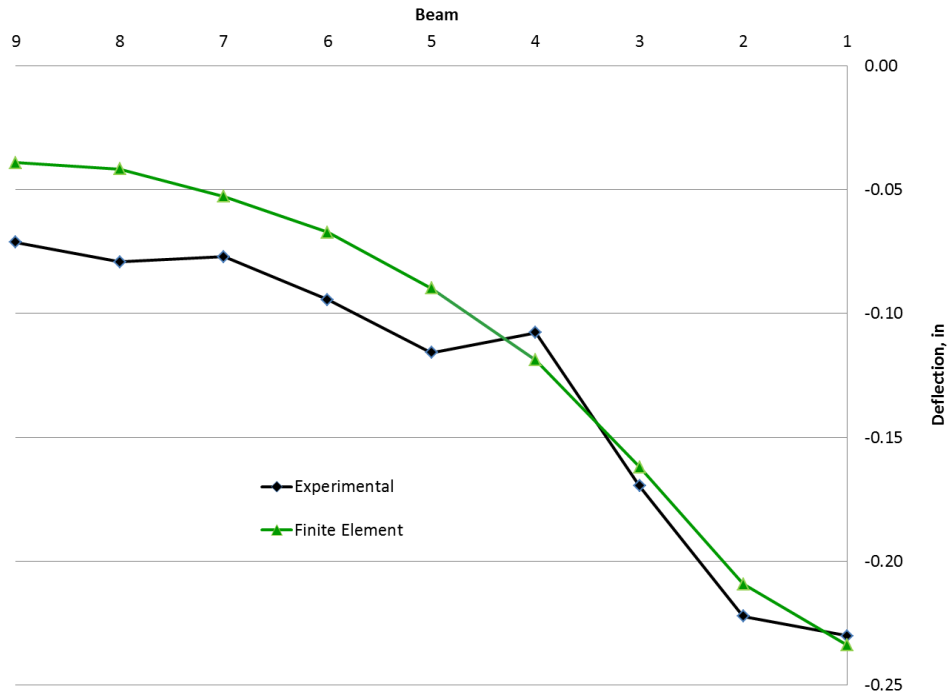


**Figure 126: FEM and Experimental Deflections Cylinder 3 (West Span)**  
 (Note: 1" = 25.4 mm)

Figures 127-130 show the FEM and experimental results for the bottom strains along instrument line A. Figure 127 provides the data when cylinder 1 was loaded to 52 kips (231 kN). Figure 128 provides the data for cylinder 2 loaded to 73 kips (325 kN), and Figure 129 shows the data for cylinder 3 loaded to 62 kips (276 kN). The last figure shows the data for the load on cylinder 2 to 62 kips again but also includes the results of the model when no damage is accounted for. The results of the modeling agree well with the experimental data for all loading cases investigated. The most significant aspect is the ability to account for the strains when the damage has occurred. This is significantly different than when no damage exists (Figure 130).

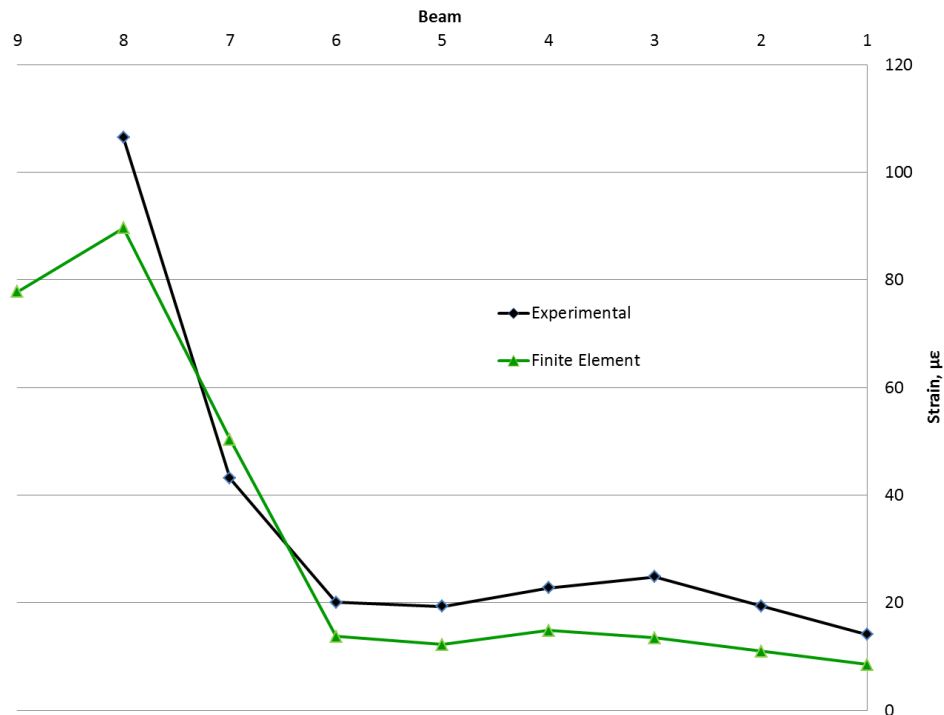


**Figure 127: FEM and Experimental Strains Cylinder 1 (West Span)**

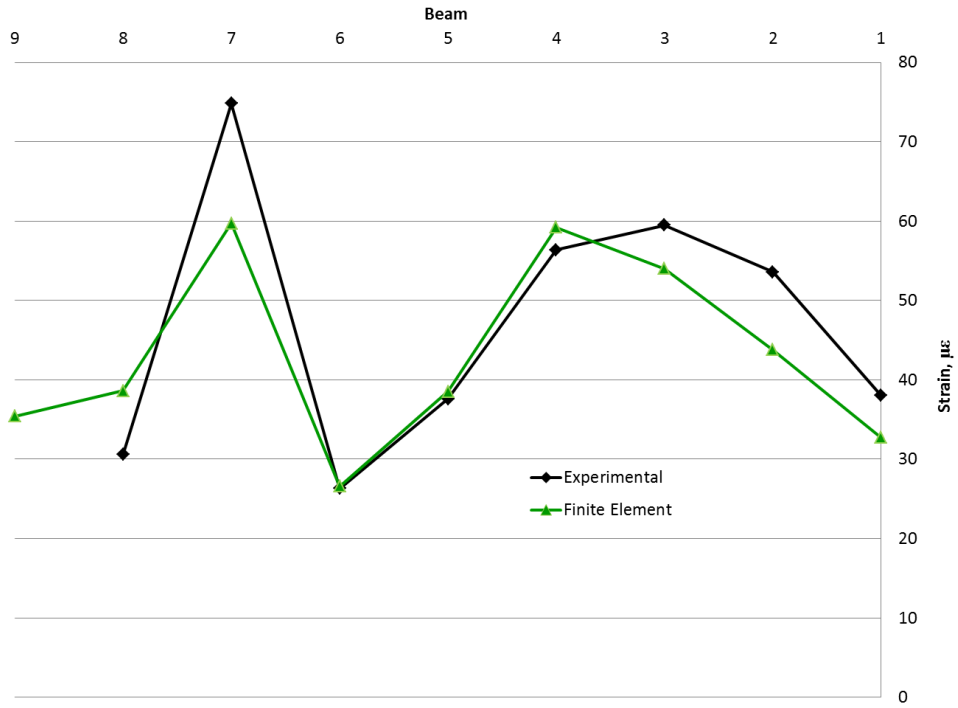


**Figure 128: FEM and Experimental Strains Cylinder 2 (West Span)**

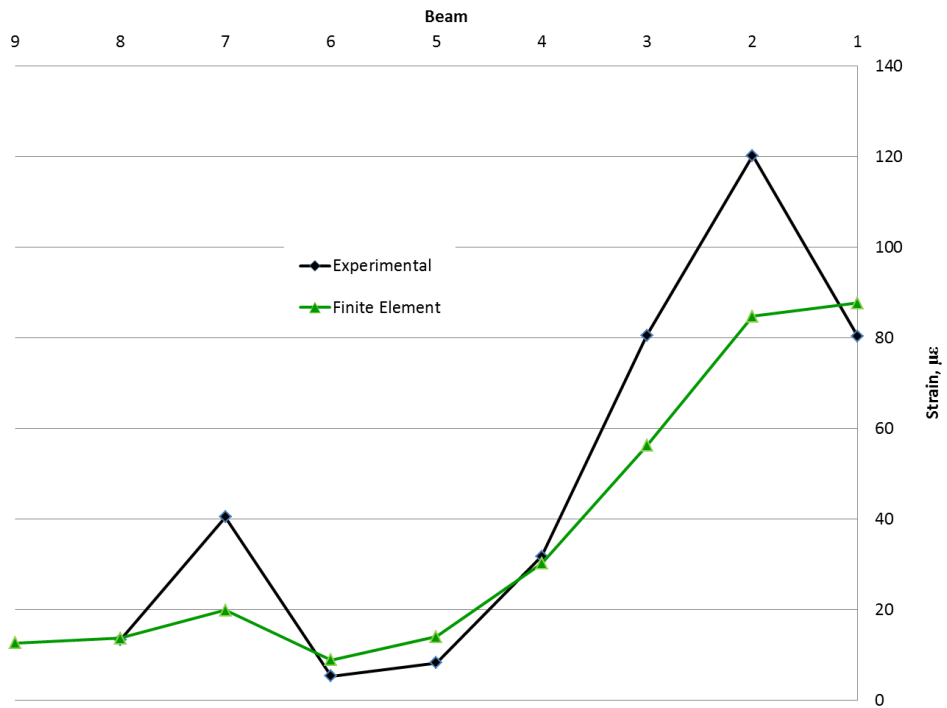


**Figure 129: FEM and Experimental Strains Cylinder 3 (West Span)**

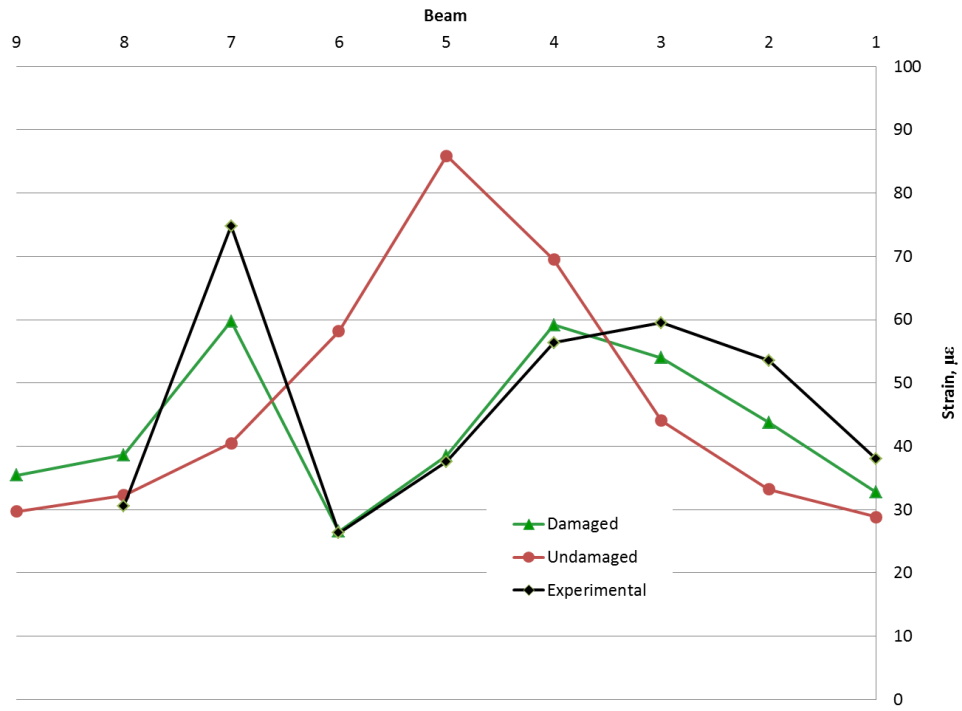


**Figure 130: FEM Damaged, Undamaged and Experimental Strains Cylinder 2 (West Span)**

## 5. CONCLUSIONS

The project involved the evaluation of all 3 spans of a 43 year old adjacent prestressed concrete box beam bridge located in Fayette County, Ohio. The research involved a forensic evaluation of the bridge that included ground penetrating radar, magnetic methods, and truck testing. Full scale destructive testing was performed on all spans after inducing three levels of additional damage to the spans. Finally, the bridge spans were assessed by load rating and advanced analytical techniques to compare to experimental results. The conclusions for the study are provided below.

### 5.1 Forensic

The GPR technique can be difficult to implement on the underside of an adjacent box beam bridge due to challenges related to access. In addition, prestressing strands on the outside of the shear steel requires the bridge to be scanned transversely. This causes delays in analyzing the data due to the unevenness and gaps that exist between the longitudinal joints of the beams. However, the GPR technique can be used to determine areas of beams that have lower quality concrete that may be the result of corroding reinforcement and also lead to reduced member capacity. The GPR technique was used on the top of the bridge to identify areas of lower quality concrete even with an asphalt wearing surface present.

For the two magnetic methods utilized in this research, it was determined that both methods gave results with reasonable accuracy to estimate the health of the prestressing strands. It was clear that MFL was in a more advanced stage of development, but IMF showed great promise. While the MFL method classifies corrosion into categories, such as mild, moderate, or heavy corrosion, the IMF method offers the potential advantage of determining the cross-sectional area of the strand with more precision and accuracy. The data collection for the IMF method took longer than for the MFL method. It was learned that the variation in the gap being maintained between the pole face and the concrete surface needs to be considered as an additional parameter to correctly estimate loss of strand volume. The weight of the IMF equipment is a big detriment, as it weighs roughly five times the MFL equipment. It is clear that a more sophisticated testing arraignment would greatly enhance the capabilities of the IMF system. Both magnetic technologies offer bridge inspectors and DOT's a valuable tool for assessing hidden damage to embedded strands in prestressed box beam bridges.

The truck testing on the West span provided significant data on the bridge behavior prior to destructive testing. The bridge behaved as a system even under very heavy truck loading. The response of the bridge was fairly symmetric showing that the stiffness of the members to be symmetric prior to damaging. The truck testing showed the bridge to act in a continuous manner even after the continuity reinforcement over the pier was cut. The dynamic load factor (impact factor) was determined to be approximately 1.10 for the bridge.

### 5.2 Full Scale Destructive Testing

The loading of the spans during the full scale destructive testing showed that all spans were relatively symmetric in stiffness across the width of the spans as determined by loading one side and then the other side. The spans were able to distribute loads across the width of the bridge even at very loads near capacity. The full scale testing showed that the East span and the

Center span had nearly the same total experimental capacity even though significant damage was induced into the East span (18 out of 243 total strands cut = 7%). The West span had a lower capacity than the East or Center span, but the West span had more damage and the damage was concentrated to 3 beams (42 out of 243 total strands cut = 17%). As all spans reached their total capacity, the upper flange of several beams crushed and the bridge failed to carry any additional load. However, all spans were still able to support and distribute lower loads. In the extreme event where the load was continued to be applied well after the capacity of the bridge was reached, load was distributed across the bridge. The shear keys transferred the load among the beams and likely continued to do so even after failing due to the transverse tie bars producing friction between beams. Complete collapse did not occur until the transverse tie bars yielded and then fractured at several locations. All spans exceeded capacities determined by AASHTO Standard Specifications and AASHTO LRFD Specifications (> 20%) when evaluating the span's total capacity as the sum of the individual capacity of the beams.

### **5.3 Load Rating**

The load rating by both the LFR and LRFR methods showed that the bridge would have required posting considering the damage to the beams in the west span. However, if the bridge was considered to act as a system rather than individual beams, the bridge did not need to be posted. Using a summation of the capacities of the individual beams to arrive at the total capacity of the bridge resulted in a conservative estimate of the total bridge capacity compared to that found by the full scale experimental testing. This also resulted in a conservative rating for the total bridge based on an analytical capacity compared to the rating based on the experimental capacity.

Assuming the bridge to be continuous compared to simply supported bridge resulted in higher ratings but did not consider the rating for negative moment over the pier. This is additional aspect may not justify the small increase in rating even if the continuity is intact.

Rating the bridge based on the total bridge capacity requires the bridge to behave as a system. For the bridge to behave as a system, the shear keys and the transverse ties have to sufficiently transfer load between beams. For the bridge destructively tested in this research, the transverse ties allowed load transfer between beams even though the shear keys had likely failed.

### **5.4 Finite Element Modeling**

The finite element modeling showed that the complete bridge could be modeled to predict the deflections and strains in the West span within reasonable accuracy and more importantly the trend of the behavior of the span. This was especially true in terms of the significant damage that was heavily concentrated within the middle portion of the span.

## 6. RECOMMENDATIONS

Based on the research performed in this project, the following recommendations can be made:

- Load rating can be done assuming the bridge behaves as a system rather than individual beams. The bridge's total capacity can be found using the summation of the individual beam's capacities found by standard AASHTO procedures. LRFD analysis was more conservative than an analysis based on the Standard Specifications. The total span capacities based on LRFD were still conservative in excess of 25% compared to full scale destructive test results.
- The shear keys and the transverse ties must be able to transfer load to the beams if the bridge is to be considered to act as a system. The destructive testing showed that even though the shear keys appeared to fail, the transverse ties were able to perform sufficiently to transfer load for the bridge spans tested. The transverse ties in the bridge tested in this research appeared to be grouted within its duct. The behavior of transverse ties that are grouted, as well as not grouted, or are in various levels of condition need to be investigated further.
- The modeling of the bridge is possible and can predict the performance of the bridge with various levels of damage. This would allow for the further investigation of bridges with different levels of damage and assist engineers in the evaluation of this type of popular bridge.
- Truck loading of these bridges with proper instrumentation can determine behavior and condition of the bridge for a more in-depth assessment.
- Ground penetrating radar (GPR) can be a tool used to evaluate the condition of the concrete on the bottom of the bridge if the data is carefully interpreted.
- The induced magnetic field (IMF) nondestructive evaluation technique must be further developed in order to overcome problems in the collection and measurement of data, but the technique shows to be a promising method for evaluating corrosion of prestressing strand.

## 7. REFERENCES

- AASHTO LRFD Bridge Design Specifications, (2010), American Association of State Highway and Transportation Officials (AASHTO), 5<sup>th</sup> Edition, Washington, DC.
- The Manual for Bridge Evaluation, (2008), American Association of State Highway and Transportation Officials (AASHTO), First Edition, Washington, DC.
- Barzegar, F., & Maddipudi, S. (1997). Three-dimensional modeling of concrete structures. II: Reinforced Concrete. *Journal of Structural Engineering*, 1347-1356.
- Bridge Design Manual, (2004), Ohio Department of Transportation, Office of Structural Engineering, Columbus, OH, .
- Harries, K. (2009), "Structural Testing of Prestressed concrete Girders from the Lake View Drive Bridge," *Journal of Bridge Engineering*, ASCE, Vol. 14, No. 2, March/April, pp. 78-92.
- Harries, K., Gostautas, R., Earls, C., and Stull, C. (2006), "Full-scale Testing Program on Decommissioned Girders from the Lake View Drive Bridge," *Rep. No. CE/ST 33, The Pennsylvania Department of Transportation*, Dept. of Civil and Environmental Engineering, Univ. of Pittsburgh, Pittsburgh.
- Hucklebridge, A., El-Esnawl, H., and Mosses, F., (1993), "An Investigation of Load Transfer in Multi-Beam Prestressed Box Girder Bridges," Final Report submitted to the Ohio Department of Transportation, Department of Civil Engineering, Case Western Reserve University, September, Report No. FHWA/OH-94-002.
- Labia, Y., Saiidi, M., Douglas, B., (1997), "Full-Scale Testing and Analysis of 20 Year-Old Pretensioned Concrete Box Girders," *ACI Structural Journal*, Vol. 94, No. 5, pp. 471-482.
- Lichtenstein Consulting Engineers, Inc., (2001), *Manual for Condition Evaluation and Load Rating of Highway Bridges using Load and Resistance Factor Philosophy*, National Cooperative Highway Research Program (NCHRP), Washington, DC.
- Manual of Bridge Inspection, (2010), Ohio Department of Transportation, Columbus, OH, ORC 5501.47, pp. 397.
- Maierhofer, C., Reinhardt, H., and Dobman, G., (2010), Non-Destructive Evaluation of Reinforced Concrete Structures, Vol. 2 Non-Destructive Testing Methods, Woodhead Publishing Limited, Oxford, CRC Press.
- Marsh, M. L., and McLean, D. I. (1998), "Dynamic Impact Factors for Bridges," *Synthesis of Highway Practice 266*, Transportation Research Board, National Research Council, Washington, D.C.

MacGregor, J. G., and Wight, J. K., (2005), Reinforced Concrete, Upper Saddle River, New Jersey: Pearson Education Inc., 4<sup>th</sup> Edition.

Miller, R., Hlavacs, G., Long, T., and Greuel, A., (1999), Full Scale Testing of Shear Keys for Adjacent Box Girder Bridges, *PCI Journal*, V. 44, No. 6, Nov./Dec., pp. 80-90.

Miller, R., Aktan, A., and Shahrooz, B., (1994), “Destructive Testing of a Decommissioned Concrete Slab Bridge,” *Journal of Structural Engineering*, ASCE, Vol. 120, No. 7, July, pp. 2176-2198.

Miller, R., and Parekh, K. (1994), “Destructive Load Testing of Deteriorated Prestressed Concrete Box Bridge Beam,” *Transportation Research Record*, (1460), pp. 37-44.

Minervion, C., Sivakumar, B., Moses, F., Mertz, D., and Edberg, W., (2004), “New AASHTO Guide Manual for Load and Resistance Factor Rating of Highway Bridges,” *Journal of Bridge Engineering*, ASCE, Jan/Feb., Vol. 9, No. 1, pp. 43-54.

Naito, C., Jones, L., and Hodgson, I. (2010), “Inspection methods & techniques to determine non visible corrosion of prestressing strands in concrete bridge components, Task 3 – Forensic Evaluation and Rating Methodology,” *ATLSS Report No. 09-10*, Lehigh University, Bethlehem, PA and Pennsylvania Department of Transportation, Harrisburg, PA.

Oh, B., Kim, K., and Lew, Y., (2002), “Ultimate Load Behavior of Post-Tensioned Prestressed Concrete Girder Bridge through In-Place Failure Test,” *ACI Structural Journal*, American Concrete Institute, Detroit, March/April, pp. 172-180.

Scanlon, A. and Mikhailovsky, L., (1987), “Full-scale Load test of Three Span Concrete Highway Bridge,” *Canadian Journal of Civil Engineering*, Vol. 14, No. 1, February.

Standard Specifications for Highway Bridges, (2002), American Association of State Highway and Transportation Officials (AASHTO), 17<sup>th</sup> Edition, Washington, DC.

Steinberg, E., and Miller, R., (2011), Structural Evaluation of LIC-310-0396 Box Beams with Advanced Strand Deterioration – Phase I Interim Report, Ohio Department of Transportation and the U.S. Department of Transportation, Federal Highway Administration, Ohio University and the University of Cincinnati, May, pp. 140.

Zhang, J., Peng, H., and Cai, C., (2011), “Field Study of Overload Behavior of an Existing Reinforced Concrete Bridge under Simulated Vehicle Loads,” *Journal of Bridge Engineering*, ASCE, Vol. 16, No. 3, March/April, pp. 226-237.